Attosecond soft X-ray absorption revealing the ultrafast non-adiabatic dynamics of furan

STEFANO SEVERINO

ABSTRACT

One of the fundamental goals of the physical chemistry community has always been to be able to follow the details of the evolution of chemical reactions in real time. Besides the extreme temporal resolution (sub-femtoseconds) required, a blurred picture of the dynamics often arises from the difficulties of spectroscopically disentangling the interplay between the electronic and nuclear degrees of freedom in complex compounds. This depends on the observable used for the experiments, which defines the direct and indirect information that can be retrieved. For example, electron diffraction or X-ray scattering methods directly track the structural changes of a species during a reaction. X-rays Absorption Fine Structure (XAFS) spectroscopy, instead, follows the dynamics from the electron perspective by probing transitions from a core orbital to an empty valence orbital. Especially when applied to the soft X-ray wavelength region, the core-hole transitions minimize the spectral congestion and provide inherent element, charge and state sensitivity. At the same time, the observable is strongly dependent on the geometrical changes and, hence, provides information regarding nuclear dynamics.

With the emergence of attosecond science, the remarkable properties of XAFS spectroscopy were combined with unprecedented temporal resolution matching the natural timescales of electronic motion in matter. This equipped the scientific community with a tool capable of disentangling the details of the intricate dynamics that arise from the interaction between light and matter and initiated a revolution in the field of ultrafast spectroscopy. Among the many chemical dynamics that can be investigated, Attosecond XAFS (AttoXAFS) spectroscopy is very appealing for the study of non-adiabatic processes of polyatomic systems involving degeneracy points of the potential energy surfaces, i.e., conical intersections (CIs), in which electronic and vibrational coherence play a crucial role. In these phenomena, the ability to disentangle the nuclear and electronic degrees of freedom is fundamental for a correct interpretation of the process.

In this thesis, AttoXAFS in the soft X-rays is applied to the study of the complex non-adiabatic dynamics of a prototypical heterocyclic molecule, furan. Analysis of the experimental data, with the support of high-level simulations, provides a clear interpretation of the ultrafast coupled electron and nuclear dynamics. The

temporal resolution and sensitivity to both electronic occupancies and structural changes allow following the dynamics step by step, revealing information about the nuclear and electronic configuration of the molecule with an unprecedented level of detail. The resulting picture shows how the passage through subsequent CIs defines the flow of the electronic population through transient dark states and the complete relaxation to the ground state, as well as the interplay between electronic and vibrational coherence dynamics.

In chapter 1 of this thesis, I will provide the framework for these results. This consists, on the one hand, of the recent development of attosecond science and its achievements in the study of light-matter interaction and, on the other, the coupled nuclear and electronic dynamics that characterize the photoinduced chemical reaction of polyatomic systems. In chapter 2, I will present the experimental setup developed in Prof. Dr. Jens Biegert's lab with which the results of this thesis were obtained. In chapter 3, I will discuss the importance of high photon energy pulses for materials science, focusing on XAFS and its capabilities, and show its exemplary applications on various solid state and gas phase samples achieved during my PhD. The core of this thesis is presented in chapter 4, where I will describe the experimental data on furan and the main results of the combined theoretical and experimental investigation. Finally, I will conclude with a summary and an outlook.

CONTENTS

1

INTRODUCTION

The goal of the first chapter of this thesis is to display the scientific framework in which the present work locates itself. This is crucial to perceive the motivations that drove the experimental investigations that will be described in the following. Firstly, it is important to introduce the reader to the field of attosecond science, born with the experimental implementation of the first attosecond pulses. In the first section, I will describe the spectroscopic revolution initiated by such technological breakthrough that enabled the investigation of phenomena of light-matter interaction never observed before. In the following two sections, I will focus the attention on the ultrafast processes that take place in polyatomic systems, starting from the non-adiabatic crossing of potential energy surfaces, 1.2, and then moving to purely electronic dynamics, 1.3. In treating these topics I will describe the strong connection between these two phenomena that constitute the whole picture of the complex electron-nuclear dynamics, which is at the basis of the field of attochemistry. Over the whole chapter I will discuss the major experimental observations, with particular attention to the potentialities and the achievements of attosecond transient absorption spectroscopy investigations.

1

1.1. ATTOSECOND X-RAY SCIENCE

In the 80s, the technological developments in the field of laser sources enabled the generation of laser pulses with 10/100 femtoseconds (fs) (10^{-15} s) temporal duration. This had a tremendous impact on the scientific community. In those years, the outstanding work of the Nobel laureate Ahmed Hasan Zewail introduced for the first time the concept of "femtochemistry": "studies of physical, chemical or biological changes at the fundamental time scale of molecular vibrations", i.e. femtoseconds (from ref. [1]). The first ingredient needed to perform such investigations is a tool, namely a pump, capable of initiating in a reproducible way a change that will define the beginning of the chemical reaction, the time zero. There are three crucial requirements in order to guarantee the reproducibility of such a reaction: i) the "zero" needs to be accurate in the order of femtoseconds; ii) all the excited molecules have to be synchronized in their evolution; iii) the induced excitation has to be coherent. Moreover, it is necessary a probing technique to follow the evolution of the system with an appropriate temporal resolution. Professor A. H. Zewail and his group demonstrated, experiment after experiment, that ultrashort laser pulses allow performing such investigations [2–6]. On the one hand, an ultrafast laser pulse can initiate a change inducing a coherent electronic excitation, acting as a "pump"; on the other, spectroscopy, diffraction imaging and other techniques can act as "ultrahigh-speed photography" when performed by means of such ultrashort pulses. In this pump-probe scheme, varying the optical path difference between pump and probe translates into a difference in the arrival time of the pulses (1 μm $\rightarrow$ 3.3 fs). The combination of all the subsequent captured snapshots creates the molecular "movie" of the chemical reaction.

From the indetermination principle, a particle in a superposition of states will oscillate with a period that is proportional to the energy difference between these. The larger the energy difference, the faster the particle's motion. For instance, the millielectronvolt energy separation between vibrational levels of molecules implies that molecular vibrations happen in the time scale of hundreds of femtoseconds. The motion of electrons is much faster, ranging from tens of fs to less than an attosecond (as) (10^{-18} s). Motion within nuclei is predicted to be even faster, on a zeptosecond (10^{-21} s) time scale.
In the first years of the 80s, the possibility of temporally resolving vibrational and rotational coherence, bond-breaking dynamics and transition states of chemical reactions was perceived as the "femtosecond dream" and became a reality thanks to Professor Zewail's work in the following 10-20 years. In analogy, the "attosecond dream", instead, consists of the possibility of resolving in real-time the motion of electrons, which are ultimately responsible for the structural changes that

lead to bond breaking and formation in chemical reactions. The electron configuration of the external molecular orbitals defines the properties of the valence states and their quantum dynamics. These govern the response of a system to non-equilibrium conditions and thus its implementation into functional devices. A full understanding of this process requires disentangling the involvement of the various contributions to the non-equilibrium electronic properties and it is the primary goal of attosecond science.

The birth of attosecond science is linked to the extraordinary results obtained in the last decade of the 20^{th} century in the comprehension and control of a highly non-linear optical process known as high-harmonics generation (HHG) [7, 8]. In the interaction of an intense laser pulse with a gas, electrons are tunnel ionized in a short time window (sub-fs) in the proximity of the electric field peak and then can recollide with the parent ion within one optical cycle of the driving laser (≈2.7 fs at 800 nm). On the recollision, the free and bound components of the electron wavefunction interfere, generating an oscillating dipole that emits radiation (more details in chapter 2). The high kinetic energy acquired by the free electrons in their interaction with the intense driving laser is such that the recollision electrons wavelength is typically very short, matching the interatomic distance in the matter. Both the recollision electron pulse and the emitted optical pulse have, intrinsically, attosecond temporal duration and atomic spatial resolution. Their properties can be controlled by acting on the intense driving pulse. This opened to the possibility of two kinds of investigations that I will refer to as in-situ or ex-situ.

In-situ experiments exploit either the electron or the optical attosecond pulse to retrieve information about the emitting medium. Since the recollision happens during one optical cycle, this can be used to retrieve information about the dynamics induced by the intense driving laser. The short recollision electrons wavelength makes these techniques suitable to measure the molecular structure. For example, the recollision electrons can diffract from their parent ion allowing molecular imaging, namely laser-induced electron diffraction (LIED) [9, 10]. High harmonic spectroscopy (HHS), instead, makes use of the emitted radiation spectrum that encodes information about the bound electron wavefunction. HHS demonstrated to be very sensitive to structural rearrangement and electronic structure and dynamics of atoms and molecules [11–14]. These in-situ techniques can be incorporated in a pump-probe scheme, hence enabling time-resolved investigations with attosecond temporal resolution and nanometric spatial sensitivity [15–17].

In the ex-situ case, instead, the generated attosecond optical pulse is used to probe ultrafast dynamics in systems different from the emitting medium. This has

the advantage of disentangling the process of HHG from the one under investigation, at the cost of a more complex experimental implementation. As well as for the recollision electrons, also the emitted photons have nanometric spatial resolution due to their short wavelength (1-10 nm). In other words, the attosecond pulse generated through HHG is, typically, in the X-rays spectral region and therefore can induce core-level electronic transitions in which the excited electron is taken from an inner orbital. When such a pulse is used as a probe, the core-to-valence transition carries site-specific information about the electronic and nuclear structure of the system, getting rid of the spectral congestion that typically affects the valence-to-valence probing techniques (more details in chapter 3). This is especially true in time-resolved investigations of non-equilibrium properties of a system in which the valence orbitals can be strongly altered in time by the photo-induced pump excitation, making the interpretation of the results strongly relying on expensive simulations [18].

The intrinsically combined spectral and temporal properties of these pulses initiated a revolution in the spectroscopic community [19]. Many review articles collect the greatest achievements of attosecond science [20–25]. Here I will present just the most relevant ones for the development of the field.
An actual attosecond experiment would require an attosecond temporal duration for both the pump and the probe pulse, but the low photon fluxes of HHG attosecond sources typically preclude such measurements. Nevertheless, the ability to lock the Carrier-to-Envelope Phase (CEP) of the electric field of few-cycle pulses allowed measurements of dynamics down to sub-cycle time duration of the femtosecond pulse, reaching sub-fs temporal sensitivity.

The first experiments investigated the electronic dynamics of atomic systems. Just one year after the experimental demonstration of the first attosecond pulses [26, 27], the first attosecond resolved experiment investigated the Auger relaxation dynamics in krypton, revealing a $3d$ core-hole lifetime of 7.9 fs [28]. The spectroscopic technique employed for this investigation is known as attosecond streaking, in which the kinetic energy of a photoelectron ionized by the high photon energy attosecond radiation is recorded as function of the delay of a CEP-stable intense pulse. This has been extensively employed also for the temporal characterization of attosecond pulses [29] and will be described in detail in section 2.1.3. The same method allowed to measure photoemission delay down to 20 as in noble gases [30, 31] and solid-state systems [32–34].

In photofragmentation spectroscopy, the system under investigation is first ionized by the x-rays attosecond pulse and then doubly ionized by a delayed few-

cycle near-infrared (NIR) pulse. The resulting charged fragments, ions, are then detected with a time-of-flight spectrometer (ToF). Applying attosecond pulses to this photofragmentation spectroscopy, in 2007 Uilberacker and coworkers studied light-induced electron tunneling in Xenon and Neon observing a yield increase synchronised with the NIR electric field [35]. A big step forward in the study of polyatomic molecules was realized in 2014 when Calegari and coauthors investigated in photofragmentation spectroscopy the prompt ionization process of the amino acid phenylalanine induced by an attosecond x-rays pulse[36]: oscillation of the doubly charged immonium ion yield with 4.3 fs period turned out to be a manifestation of periodic ultrafast electronic charge dynamics initiated by the x-rays pulse.

Outstanding results have been obtained by applying attosecond pulses to transient absorption spectroscopy in both gas-phase and solid-state systems. These will be described in more detail in the following section, being this the spectroscopic technique used for the present PhD project.

1.1.1. ATTOSECOND TRANSIENT ABSORPTION

In transient absorption spectroscopy, the spectral response of the system under investigation is measured as function of the pump-probe delay. This is a well-established technique in the ultraviolet (UV), visible (VIS) and infrared (IR) probing regimes. When the spectral region is moved in the x-rays, synchrotron-based works showed that the method is strongly sensitive to both electronic environment and molecular structure, while carrying site-specific information [37, 38]. In the x-rays community, the method is known as x-rays fine structure spectroscopy (XAFS) and will be described in detail in chapter 3. The experimental demonstration of HHG and attosecond pulses enabled to perform time-resolved XAFS studies with table-top sources and unprecedented temporal resolution [39, 40].

Also in this case, the first investigations focused on the response of atomic systems to the combination of an attosecond and an intense IR-NIR pulses. In 2010 Goulielmakis and coauthors tracked with a sub-150 as pulse the cation dynamics of krypton atoms induced by an intense few-cycles IR pulse, spectrally resolving the $3d^{-1}$ core-hole transitions ($\approx$80 eV) [41]. The authors observed a quantum beating with a period of 6.3 fs, originating from the superposition of coherently excited states produced by the NIR pump pulse, and fully characterized its degree of coherence. Several studies on rare gases employed a less intuitive sequence of pulses in which the intense IR-NIR pulse arrives after the attosecond one. Rather than triggering a photoexcitation, in this case, the IR-NIR acts as a “control pulse”,

dressing the atomic system and thus dynamically changing its absorption [42, 43]. A more detailed description of these experiments and an exemplary measurement in argon performed with the attosecond beamline at ICFO will be presented in section 3.3.2. These works revealed spectral features known as light-induced-states [44, 45], Autler-Townes splitting [46], changes in absorption lines [47] and enabled measurements in the temporal domain of core-hole states' lifetime [48, 49].

These first time-resolved attosecond transient absorption investigations exploited pulses with photon energy in the extreme ultra-violet (XUV) spectral region (10 eV - 120 eV) where it is possible to interrogate the dynamics through the semi-valence transitions. Despite the great results that were obtained in both solid state [50, 51] and gas phase systems [52–54], such probing technique is limited by the challenging interpretation of the absorption spectra. The multiple pathways that follow the absorption of an XUV photon can induce parasite effects, e.g. the multiplet effect, that can alter the resulting absorption spectrum [37, 55, 56]. Moreover, probing a material at these energies can affect the dynamics under investigation and make its interpretation challenging. Accessing the soft x-ray (SXR) spectral region (>120 eV) allows probing the dynamics from the inner core orbitals, like the $1s$ or $2s$, minimizing the ambiguities and enabling a direct connection between the absorption spectrum and the charge carriers. In particular, the water window (280 eV - 532 eV) is a spectroscopically important region for the transparency of water and the presence of core resonances of many elements relevant to organic chemistry such as Carbon (284 eV), Nitrogen (402 eV) and Oxygen (532 eV) $1s$ edges (also known as K-edges). For these reasons, a fundamental step in the development of attosecond transient absorption was the extension of such spectroscopic technique to the water window. The group of Prof. Jens Biegert at ICFO pioneered this by exploiting the ponderomotive scaling law to extend the HHG cutoff to more than 500 eV [39, 57, 58], demonstrating the first spatiotemporal isolation [40] and temporal characterization [59] of an attosecond pulse in the water window. Thanks to these great results, the group performed the first proof-of-principle transient absorption measurement [39] and the first extended edge investigation [60] at the C K-edge from a table-top source. Reaching this spectral domain with table-top sources has been the result of strong efforts in the attosecond community, which will be described in chapter 2, and has opened the way to the investigation of a broad range of organic molecules.

Focusing on the time-resolved investigation, the only two studies on solid-state systems in the water window spectral region have been performed in our lab at ICFO. The first investigated the ultrafast carriers' motion in a thin TiS_2 film [61, 62]. The dynamics probed at the Ti $L_{2,3}$-edges (460 eV) revealed carriers os-

cillations at twice the pump optical cycle that were interpreted with the help of simulations as intra-band carriers motion. In the second one, we investigated the relaxation dynamics of the photon-carrier-phonon system in a highly oriented pyrolytic graphite (HOPG) thin sample at the C K-edge, demonstrating that the spectroscopic technique is capable of following simultaneously carrier and phonon evolution upon photo-excitation [63].

Moving to the gas phase systems, the first time-resolved transient absorption measurement in the water window was published in 2017 by the group of Professor Hans J. Worner [64]. In this experiment, Y. Pertot and coworkers followed the evolution of CF_4 after strong-field ionization leading to the $C-F$ dissociation and showed how the reshaping of the x-ray absorption spectrum could be explained by the structural rearrangement of the molecule. In 2019 the technique was extended to the N K-edge by N. Saito and coworkers who investigated the electronic, vibrational and rotational dynamics of NO with attosecond temporal resolution [65].
In more recent years, the number of attosecond transient absorption experiments in polyatomic systems increased considerably. Thanks to its sensitivity to both the electronic and nuclear structure, the technique proved to be a great tool for tracing potential energy curves crossing dynamics [54, 66–68]. The non-adiabatic dynamics around these crossing points, known as conical intersections (CIs), are complex, happen on ultrafast timescales (10-100 fs) and involve both the electronic and nuclear degrees of freedom of the system. The comprehension of the energy flow through CIs is crucial for the understanding of several chemical and biological relevant processes and it will the focus of the next section. In parallel, experimental and theoretical investigation demonstrated attosecond transient absorption to be valid also for the study of electronic coherence [53, 69–71]. The possibility to steer chemical reactions acting on coherently excited electronic states is one of the most exciting applications of attosecond chemistry and will be described in the following sections.
It is worth noting that, despite of the great improvements in the field, the number of HHG-based studies in polyatomic molecules in the water window is still small [64, 65, 68, 71–78] and just four of them have attosecond temporal resolution [65, 68, 71, 78].

1.2. DYNAMICS AT CONICAL INTERSECTION

Absorption of a photon in a molecule can activate a variety of phenomena that occur on different time scales. Assuming an instantaneous absorption, the electronic transition is described by the Franck-Condon (FC) principle, according to which an electronic transition is more likely to occur without changes in the po-

sitions of the nuclei, i.e. pure vertical transitions with respect to nuclear coordinates. When the lower potential energy surface's (PES) minimum, known as the FC region, is shifted with respect to the upper's one, the excitation results in a simultaneous change in the electronic and vibrational energy levels, referred to as a vibronic transition. A vibrational mode is excited provided that it is FC active, i.e. the vibrations of the mode coincide, somehow, with the motions of the nuclei required to reach the equilibrium geometry of the excited state. The larger the nuclear change, the larger the number of vibrational modes activated and the broader the absorption bandwidth.
The change in the electronic distribution causes a variation in the permanent dipole moment and in the strengths (lengths) of bonds. Suddenly the molecule is out of equilibrium. After the vibrational relaxation towards the PES minimum, an electronic transition is needed in order to take the molecule back to its ground state (GS). One possible mechanism is fluorescence, which involves the emission of a photon with energy lower than the absorbed one, where the photon energy difference can correspond to the fraction dissipated vibrationally. This radiative process tends to be slow (nanoseconds) because of the typically large energy gap between the GS and the first excited state.

The fluorescence of a system is typically quantified in terms of quantum yield, which is the ratio of the number of photons emitted to the number of photons absorbed. A compound showing a low quantum yield indicates the presence of alternative very-fast non-radiative relaxation processes that quench fluorescence. If the spin does not change from the initial to the final state, a radiation-less transition from a higher electronic state to a lower one is known as internal conversion (IC). Ultrafast ICs are a manifestation of the Born-Oppenheimer (BO) approximation's breakdown and proceed through conical intersections (CIs), which are degenerate points of PESs [79, 80]. The existence of a CI along a vibrational relaxation direction offers the system a mechanism for a highly efficient and fast electronic relaxation, where the absorbed energy is dissipated in the form of nuclear motion, and eventually heat, instead of photon emission.

Relaxation dynamics that involve the passage through CI play a primary role in most of the polyatomic molecules and enable many biological and chemical functions. An example is the UV absorption of aromatic amino acids and nucleic acid bases [81, 82], the most important building blocks of life. Sunlight contains a significant amount of harmful radiation (<400 nm) that, once absorbed, constitutes one of the most potent environmental carcinogens. Quoting A.L. Sobolewski and coworkers, *it is conceivable that the evolution of life has selected molecular building blocks with particularly short excited-state lifetimes to minimize dangerous pho-*

toreactions in living cells.[83], as a photoprotection mechanism. As a result, nucleic acid bases show a high photostability, which is due to ultrafast IC processes that ensure the release of harmful electronic energy, which otherwise would cause permanent damages [84, 85].
In the before mentioned example the IC to the GS allows the system to return to its initial condition. A different class of ultrafast relaxations is the one that induces a chemical reaction. This is the case of the photoisomerizations of the retinal chromophore in rhodopsin, where the relaxation of the system through CI offers the route for an ultrafast cis-to-trans isomerization [86, 87]. This constitutes the first of a series of chemical reactions that are initiated by photon absorption and culminate in the stimulation of the optic nerve [88].

These and many other examples testify to the importance of CIs in photochemistry and photobiology[80, 89–91]. These processes typically take place on a timescale of 10-100 fs and involve multiple excited states. The non-adiabatic nature of the phenomena poses great challenges to the investigation of such dynamics, both theoretically and experimentally. In the next sections I will first provide the theoretical framework for ultrafast IC relaxation dynamics and then describe the most recent relevant experimental observations of ICs with a special focus on attosecond transient absorption spectroscopy.

1.2.1. BORN-OPPENHEIMER APPROXIMATION AND BEYOND

The BO approximation is a milestone in the theory of molecules and is basic to all molecular quantum mechanics. The concept at the basis of this approximation is that the large mass of a nucleus with respect to an electron allows separating the electronic and nuclear motions. This permits a great simplification in the theoretical treatment of molecular dynamics and allows the introduction of the concept of molecular electronic states, which is of great help in the visualization of their dynamics, even when the approximation fails.
The Hamiltonian (H) of a molecular system is

$$H = T_n + T_e + U(\mathbf{r}, \mathbf{R}) \tag{1.1}$$

where U is the total potential energy operator as function of the electronic, $\mathbf{r}$, and nuclear, $\mathbf{R}$, coordinates and T_n and T_e are, respectively, the nuclear and electronic kinetic energy operators. We can define the electronic Hamiltonian $H_e = T_e + U(\mathbf{r}, \mathbf{R})$, which is parametrically dependent on the nuclear coordinates and whose eigenvalues V_i and eigenfunctions ϕ_i fulfill the following relation:

$$H_e \phi_i(\mathbf{r}, \mathbf{R}) = V_i(\mathbf{R}) \phi_i(\mathbf{r}, \mathbf{R}). \tag{1.2}$$

The set of eigenfunctions $\phi_i(\mathbf{r},\mathbf{R})$ form a complete basis and can be used to expand the total wavefunction ψ of the total Hamiltonian 1.1 as:

$$\psi(\mathbf{r},\mathbf{R}) = \sum_i \phi_i(\mathbf{r},\mathbf{R})\chi_i(\mathbf{R}). \tag{1.3}$$

This is known as BO expansion [92] and it does not include any approximations. $\psi(\mathbf{r},\mathbf{R})$ must fulfill the full Schrödinger eqn. $H\psi(\mathbf{r},\mathbf{R}) = E\psi(\mathbf{r},\mathbf{R})$. Using the BO expansion 1.3, multiplying the full Schrödinger equation from the left by $\phi_j^*(\mathbf{r},\mathbf{R})$ and integrating over $\mathbf{r}$ we obtain the following relation:

$$[T_n + V_j(\mathbf{R})]\chi_i(\mathbf{R}) - \sum_i \Lambda_{ij}\chi_i(\mathbf{R}) = E\chi_j(\mathbf{R}). \tag{1.4}$$

Λ_{ij} is the non-diabatic coupling term and describes the interplay between the electronic and nuclear motion:

$$\Lambda_{ij} = \delta_{ij}T_n - \int \phi_j^*(\mathbf{r},\mathbf{R})\,T_n\phi_i(\mathbf{r},\mathbf{R})\,d\mathbf{r}. \tag{1.5}$$

The off-diagonal elements of this term represent the possibility of coupling between different electronic states as a consequence of the nuclear motion and are larger the closer these are energetically.

The BO approximation lies on the adiabatic ansatz that, given the different velocities between electrons and nuclei, the former can adapt to the slow nuclear motion. This does not imply a complete separation between the two degrees of freedom, $\mathbf{r}$ and $\mathbf{R}$, but a parametric dependence of the electron wavefunctions ϕ on the nuclear coordinates, such that

$$\psi(\mathbf{r},\mathbf{R}) = \phi(\mathbf{r},\mathbf{R})\chi(\mathbf{R}). \tag{1.6}$$

This ansatz implies that each electronic state can be treated separately. In other terms, eqn. 1.6 states that the nuclear motion can not couple different electronic states as in the non-adiabatic term 1.5. Repeating the same steps as before, eqn. 1.4 becomes

$$[T_n - \Lambda + V(\mathbf{R})]\chi(\mathbf{R}) = E\chi(\mathbf{R}) \tag{1.7}$$

for a specific electronic state. This relation can also be retrieved from 1.4 putting at zero all the off-diagonal terms of Λ_{ij}. The adiabatic ansatz 1.6 is accurate for electronic states that are well separated energetically from others and the approximation improves with increasing nuclear mass. These conditions imply a weaker dependence of the electronic wavefunction on the nuclear coordinates and a smaller non-adiabatic term $\Lambda = T_n + \int \phi^*(\mathbf{r},\mathbf{R})\,T_n\phi(\mathbf{r},\mathbf{R})\,d\mathbf{r}$. Neglecting its contribution, we

obtain the Born-Oppenheimer approximation, also known as adiabatic approximation:

$$[T_n + V(\mathbf{R})]\chi(\mathbf{R}) = E\chi(\mathbf{R}). \tag{1.8}$$

When Λ cannot be neglected, it implies a relevant coupling contribution and other electronic states need to be taken into account. In this case, the process is defined as non-adiabatic and more than one Born-Oppenheimer PES ($V(\mathbf{R})$) needs to be taken into account. Despite the importance of BO approximation in our understanding of molecular physics, the study of non-adiabatic processes goes back to 1932 [93]. These can be divided into two classes. Non-Born-Oppenheimer processes are those where the breakdown of the BO approximation is so strong that the notion of PES is not useful and nuclear and electronic degrees of freedom must be treated equally. When the nuclear kinetic energy is not excessive, instead, it is still possible to use the concept of PES, but it is necessary to consider the coupling between different surfaces. The latter is the case of radiationless ICs. Such transitions are very likely to happen in the vicinity of a point in the nuclear coordinate space where two Born-Oppenheimer PESs intersect, namely a conical intersection. The investigation of dynamics at CIs requires the evaluation of the non-adiabatic term 1.5, which represents the coupling effect of the nuclear motion among different electronic states.

Conditions for the existence of such degeneracy points were investigated for the first time in 1929 by von Neumann and Wigner [94], just two years after the formulation of the BO approximation. They realized that the non-crossing rule for PESs of the same symmetry only holds for systems with one vibrational degree of freedom. In 1937 E. Teller showed that CI may generate an efficient and fast radiationless transition [95] using an extension of Zener's one-dimensional approach [93] and coined for the first time the term conical intersection. Since these early works, a lot of effort has been put in order to describe the nature of dynamics at CIs and identify the molecular geometries at which they occurred (details can be found in several reviews and books [79, 96–98]). By this moment, it was known that CIs can have a crucial role in the dynamics if there are two or more vibrational modes. Still, the common opinion in the 70s was that CIs are very rare and special cases, as expressed by Michl in a review on organic photochemistry in 1974 [99]. This opinion was prevalent until 1990 when the development in the field of numerical computation started playing an important role. In 1990 two groups independently demonstrated the existence of CI in triatomic molecules [100, 101]. In the same year Robb, Bernardi and Olivucci proved the existence of CI in photochemical pericyclic reactions of bigger systems [102]. In the following years, a number of works demonstrated that CIs are ubiquitous in polyatomic molecules

and have a crucial role in many biological and chemical functions.

Fig. 1.1 displays a schematic representation of a photochemical reaction involving CIs. Fig. 1.1(a) shows the coupling between two PESs (GS and excited state) as function of the nuclear coordinates. Starting from the geometry at GS_1, an excited state (EX_1) is created at the same geometry, according to the FC principle. Subsequently, the system can evolve towards either CI_1 or CI_2, where it decays to the electronic GS, then progresses towards the geometrical structures GS_1 or GS_2. X_1 and X_2 are the nuclear coordinates that define the degeneracy points (see inset), while X_3 represents the remaining ones orthogonal to X_1 and X_2. This example shows a common situation where, depending on the initial conditions, the system can decay towards the GS with two competitive relaxation pathways, with X_1 and X_2 defining the branching space. The inset shows the typical conical shape of the crossing point from which is named. In more complex systems the decay dynamics can involve two or more subsequent CIs, with one or more electronic excited states assuming the transient role (neither populated at the beginning or at the end of the dynamics) of assisting the flow of energy from the primarily excited state to the GS [83] (see Fig. 1.1(b)).

Despite the great advancements in the localization and prediction of CIs, an effort is still needed in order to be able to correctly predict the quantitative aspects of ICs and to provide a theoretical comparison to the experimental investigations [18, 103, 104]. In this sense, the recent developments of experimental techniques, like attosecond transient absorption, capable of providing a clearer picture of ultrafast IC dynamics, establish strong references against which the computational results can be benchmarked.

1.2.2. EXPERIMENTAL OBSERVATION OF CIS

Besides the high temporal resolution needed to investigate CIs dynamics, another challenge is represented by the strong interplay of the nuclear and electronic degrees of freedom, which determines the behavior of the system in the vicinity of a CI. Spectroscopic techniques are typically able to directly probe either one or the other, hence missing details of the whole dynamics.

When tracing the vibrational character of a system, measurements rely on the PESs' distortion in the vicinity of a CI. The resulting temporal variation of the frequencies of the modes can be interpreted as a signature of the CI passage. Among other techniques, this can be probed with IR transient absorption (IR-TA) [105–107] or Raman spectroscopy[108, 109]. In these measurements, information re-

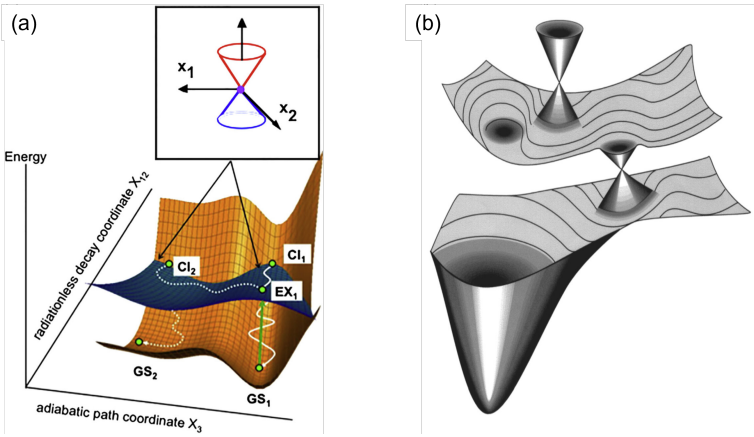

Figure 1.1: Schematic representation of photoinduced chemical reaction involving CIs. (a): IC dynamics involving two competitive relaxation pathways (CI_1 and CI_2). X_1 and X_2 define the degeneracy point, while X_3 represents the remaining orthogonal nuclear coordinates. The inset shows the degeneracy point along X_1 and X_2 with the typical conical shape. From reference [98] (b): cartoon of PESs of a non-adiabatic decay involving multiple CIs and a transient state. From reference [83].

garding the electronic configuration of the system can only be inferred following the comparison with the simulations and, hence, direct visualization of the electronic population's flow through a CI is difficult to achieve.

The second class of spectroscopic techniques aims at probing electronic transitions of the system while it evolves. The passage through a CI determines the flow of the electronic population between the electronic states involved, causing an abrupt change in the character of the electronic wavepacket and, consequently, of the transition dipole moment that determines the observable. In addition, the energy change of the PES due to the nuclear rearrangement also can be traced as a chemical shift of the electronic resonances, providing an indirect probing of the nuclear degree of freedom. The electronic properties of the system can be probed with transient absorption techniques using visible/UV light (UV/Vis-TA) to interrogate valence transitions or photoelectron spectroscopy (PS). These techniques in the last 20 years provided major insights into the dynamics in the proximity of CIs.

A landmark experiment in TA performed by the group of A. H. Zewail investi-

gated the non-adiabatic population dynamics of NaI being able to distinguish the different photoproducts of the reaction [110]. An outstanding result was the one obtained by D. Polli and coworkers in 2010 studying the CI dynamics leading to photoisomerization of rhodopsin [87]. Thanks to a sub-20 fs temporal resolution and a broadband probing pulse covering from the visible to the NIR, the authors showed that the CI region is reached in ≈80 fs and a complete photoproducts generation is obtained in ≈250 fs, providing what probably is the clearest observation of the primary event in vision to date. The same research group in 2018 realized an experimental investigation of thiobases (4- and 2-thiouracil) [111]. The excellent results reveal the complex dynamics involving multiple CIs and show how UV/Vis-TA can be sensitive also to the active vibrational modes. At the same time, the measurement shows how some details of the process, like the participation of a dark state, can be only inferred indirectly with this technique. In general, the spectral congestion that typically affects the lower valence to higher valence states resonances probed by UV/Vis-TA limits the possibility of assigning spectral features to specific electronic transitions.

In a pump-probe PS experiment, the observable is the kinetic energy of the ionized electrons. The typical shape of a PS trace shows how the wavepacket evolution along a PES gradient in the vicinity of CI translates into a rapid decrease in the kinetic energy of the photoelectrons, almost following the movement along the PES. PS is sensitive to the active vibrational modes [112] and provides a signature of electronic population [112–115]. One drawback is that high probing temporal resolution results in a loss of energy resolution preventing the identification of the states involved. Moreover, the theoretical analysis showed how the passage through CI can be hidden in the experimental data [116].

In this context, the generation of x-rays attosecond pulses through HHG marked a crucial moment in the experimental investigation of non-adiabatic dynamics. Besides the extreme temporal resolution that permits to access purely electronic dynamics and, hence, to provide further details of the dynamics, the spectral coverage of these sources allows interrogating core-level transitions. Differently from the valence orbitals, the core ones are much less influenced by the pump-induced valence transitions and, therefore, represent a better reference for probing the electronic population. Additionally, the orbitals are strongly localized on the atoms allowing to interrogate the electronic structure of the system from the perspective of nuclei. All in all, this results in an observable that directly interrogates the electronic configuration of the systems, while being much less affected by the spectral congestion and more sensitive to the structural changes with respect to other techniques. The implementation of these sources in transient absorption schemes is

particularly useful for the investigation of non-equilibrium dynamics induced by a valence excitation. Here, the broadband nature of the spectrum is exploited for XAFS and allows for multi-edges measurements.
An exemplary theoretical work showing the potentiality of such a technique was published by S. Neville and coworkers in 2018 [117]. They investigated the dynamics at the twisted-pyramidalized CI of ethylene (C_2H_4) showing how the time-resolved x-rays absorption at the carbon K-edge can provide a clear signature of the wavepacket dynamics. Significative is the result obtained by Attar and coauthors in 2017 in resolving the prototypical ultrafast ring-opening dynamics of 1,3-cyclohexadiene [72]. Even though the temporal resolution of the experiment was not enough to reveal the details of the process, the experiment traced the competitive relaxation pathways distinguishing the different photoproducts thanks to XAFS sensitivity to the nuclear structure. Following this measurement, over the past years XAFS demonstrated to be strongly sensitive to the structural deformations [64] and vibrational modes [54, 65, 66], to discriminate between diabatic and adiabatic curve-crossing in a diatomic molecule [53], to access quantitative information regarding the branching ratios of competitive channels [67], to be able to probe transiently populated dark states [77] and many other details of non-adiabatic processes. Recently, an attosecond XAFS (AttoXAFS) investigation at the C K-edge resolved the fastest non-adiabatic dynamics in organic molecules [68].

These works show how site-specificity, electronic and structural sensitivity and temporal resolution of AttoXAFS provide crucial benefits for the investigation of ultrafast non-adiabatic processes, setting the basis for the application of this technique to more complex and biologically relevant systems. Here, site-specificity and multi-edges measurements can play a crucial role in the interpretation of the data providing different nuclear points of view on the dynamics.

It is worth mentioning that also other approaches have been used to follow these dynamics obtaining excellent results. For example, H. J. Worner and coworkers investigated the CI dynamics of NO_2 probing its electronic degree of freedom using pump-probe HHS (see section 1.1) [16]. A completely different approach was instead used by J. Yang and coworkers in 2018, who exploited ultrafast electron diffraction to retrieve the non-adiabatic and photodissociation dynamics of CF_3I from the structural imaging of the molecule [75]. Among many available reviews on the topic, reference [103] presents a very detailed overview of the different spectroscopic techniques employed for revealing non-adiabatic processes, describing the theoretical aspects and the major results achieved. In addition, the review also shows novel spectroscopic techniques, such as 2D spectroscopy and X-rays Raman, and their promising applications.

1

1.3. ELECTRONIC COHERENCE

With the birth of attosecond science, the possibility to observe in real-time, and eventually manipulate, purely electronic dynamics with attosecond pulses raised the interest of the scientific community. A topic of particular interest was the role of electron correlation in ultrafast photoinduced chemical reactions. The attention of the scientific community around this topic was motivated by the experiments performed by Weinkauf et al. on the dissociation of peptides following site-selective ionization [118]. Even though the ionization was localized on the chromophore end, the experimental observation showed that ionic fragmentation induced by UV absorption was dominated by ionic species related to the amino acid end of the peptide chain. This process was interpreted in terms of charge relocation across the molecular backbone [119]. The effect remained unchanged when the size of the molecule was increased, indicating that the process was not driven by nuclear motion (a phenomenon known as charge transfer [120]), but by purely electron dynamics. Cederbaum and Zobeley proposed the existence of a coherent superposition of electronic states at the origin of the charge relocation dynamics, also known as charge migration [121].

Weinkauf's experiments can be interpreted as a pump-probe measurement in which the pump prepares a coherent superposition of electronic states (the site-selective ionization step) and the probe projects it on one (or more) final states. The "probing" step is essential for the electronic correlation to have a role. However, the probe does not need to necessarily be a second light pulse. For example, in polyatomic molecules, a non-adiabatic coupling of the nuclear and electronic degrees of freedom, such as the passage through a CI, can serve as a probe [122]. Following Cederbaum and coworkers' theory on charge migration [123, 124], the electronic superposition induces a charge oscillation across the molecule with a period given by the energy separation between the states. A non-adiabatic process in which two PESs approach each other can be seen as slowing down of the purely electronic dynamics (increasing charge migration periodicity with decreasing energy gap) that leads to the final localization of the charge at the crossing point of the surfaces (the probing step).

This interpretation of Weinkauf's experiment stimulated a discussion around the topic of attochemistry [122, 125]: is it possible to engineer charge-directed reactivity starting from electronic coherence? The idea behind is to control the electrons' behavior at the very early time of photoinduced dynamics as a way of doing

chemistry. The interference of the coherently excited electronic states defines a new electronic distribution and a new chemical reactivity. The first question is how to initiate such dynamics and how to control them. Attosecond pulses with their broadband spectrum offer an ideal tool to initiate such dynamics on the natural electronic time scale. Another possibility is to excite the system in a non-selective way with highly intense pulse inducing multi-photons processes.

The first experimental observations of electronic coherence relayed on strong-field ionization processes to generate a coherent superposition of electronic wave packets. In 2005 F. Lindner and coworkers studied the interference of electron wave packets created by the ionization of Argon [126]. Thanks to precise control of the phase of the ionizing femtosecond pulse, they achieved unprecedented control over the electronic interference detected by two opposing electron detectors placed symmetrically to the laser focus. In 2006 M. F. Kling and coworkers investigated D_2 dissociation with HHS [127]. The ionization of the molecule at the electric field peak initiated a dynamics in which a superposition of electronic states was induced. The recollision event after half the optical cycle probed the electronic coherence. The experiment directly offered a way to control the reactivity of the system: a shift of the CEP changes the direction of emission of the fragments generated in the dissociation. CEP control has been strongly proposed as a way to modulate the relative phase between the electronic wavepackets [128] and, hence, to steer chemical reactions at CI [129–131].
Landmark experiment revealing charge migration dynamics initiated by an attosecond pulse was published in 2014 by F. Calegari and coworkers [36]. The aromatic amino acid phenylalanine was photo-ionized with an attosecond pulse and the induced cationic dynamics were probed with a few-femtosecond intense NIR pulse. The resulting yield of immonium dication showed an oscillation with a period of 4.5 fs that was assigned to the charge density fluctuation caused by the superposition of electronic states coherently excited by the attosecond pulse. This is to date the clearest observation of charge migration in a complex biologically relevant system.

Computationally speaking, simulations of such dynamics require additional effort with respect to the already non-trivial non-adiabatic processes discussed in the previous section. The well-established independent electron approximation that allows simplifying the theoretical treatment of non-equilibrium dynamics of molecules [132] is not valid and the many-electrons interactions and coupling terms describing electron-correlation need to be taken into account. Computational predictions on such systems show that nuclear motion can affect the nature and the time scale of electronic coherence. Non-adiabatic coupling be-

tween electronic states can induce fast electronic decoherence on the order of a few femtoseconds [129, 133–135]. In order to have a role in the chemical reactivity, electronic coherence must be preserved at the "probing step" and this initiated the search for systems in which electronic coherence lives long enough [136]. Changing perspective, non-adiabatic passages through a CI itself can generate a coherent superposition of electronic states and be a source of electronic correlation-driven processes [137–139].

Theory predictions show a picture of strong coupled electronic and nuclear dynamics in which both degrees of freedom affect each other and the outcome of chemical reactions. Besides the already discussed state and structural sensitivity, AttoXAFS demonstrated to be sensitive also to electronic coherence in atomic [41, 140], diatomic [141, 142] and in small polyatomic system [71], and it has been proposed as a valid tool for even more complex systems [69]. Theoretical predictions show that the site-specificity of the observable can provide direct information on the localization of the charge density and allow for real-time tracking of the charge migration along the molecular backbone [70].

The state of the art in our comprehension of charge migration requires to experimentally investigate the effects of electronic coherence on non-adiabatic dynamics (and vice versa) of complex systems, such to have a complete and trustful description of the processes, which nowadays is still missing. This is a fundamental step in order to move to the engineering of electron wavepackets by means of light pulses to enable otherwise impossible chemical reactions.

1.4. CONCLUSIONS

Attosecond pulses made it possible to observe electronic dynamics on the sub-fs time scale, but the fundamental goal of spectroscopic investigation stays to reveal the whole picture. Electronic and vibrational coherence, non-adiabatic coupling, CIs, structural deformations and photoproducts' generation on different time scales characterize ultrafast photoinduced chemical reactions of polyatomic molecules. These processes are dependent on each other such that dynamics on the sub-femtoseconds time scales happen to determine the final outcome of the whole reaction. Attosecond transient absorption spectroscopy, especially when applied in the soft x-rays (SXR) spectral domain of the water window, is a promising tool to follow this whole picture with the required temporal, electronic and structural sensitivity. Despite the great advancements in the comprehension of its potentiality over the last decade, further steps are needed to make this a reliable technique for the investigation of such dynamics, the first of which is the extension of the

method to more complex systems with a stronger interplay between the electronic and nuclear degrees of freedom. This requirement drove the motivations for the work presented in this thesis.

2

EXPERIMENTAL FUNDAMENTS

The generation of attosecond pulses in the water window and their implementation in pump-probe schemes for spectroscopic applications are the key experimental components for the realization of the work presented in this thesis. In this chapter, I will discuss the details of such experimental implementation. It is divided into two sections: in the first, 2.1, I will present the evolution of the field of high-harmonic and attosecond pulses generation over the last 20 years and outline the primary elements necessary for the generation of such radiation, focusing on the generation of isolated attosecond pulses in the water window; in the second section, I will present the experimental setup used for time-resolved AttoXAFS in the soft X-rays (SXR). The latter is divided into three subsections, the first describing the IR laser source 2.2.1, the second dealing with the generation, detection, and characterization of the SXR attosecond pulses 2.2.2, and the third dealing with their implementation in pump-probe schemes for spectroscopic applications 2.2.3.

2.1. HHG AND ATTOSECOND PULSES

In this section, I will introduce the basic concepts of attosecond pulse generation. In doing so, I will focus on the difficulties encountered in implementing this technology in the SXR spectral region. First, I will present the generation of high-energy photons through the process of High Harmonics Generation (HHG) and introduce the three-step model and the cutoff law for the highest photon energy generated. I will then show the ingredients needed for the generation of Isolated Attosecond Pulses (IAP) and the methods for their temporal characterization.

2.1.1. THREE-STEP MODEL AND PONDEREMOTIVE SCALING

Already in the late 70s it was known that an atom exposed to an intense laser field radiates at odd multiple harmonics of the incident laser frequency [143, 144]. The development of high-intensity laser sources in the 80s increased the interest in the topics and a lot of effort was put to describe the physics behind the HHG process [145–148]. In 1993, the well-established "three-step model" was introduced for the first time independently by P. B. Corkum [7] and Kulander et al. [149]. The interaction of an intense laser field (10^{14}-10^{15} Wcm^{-2}) with an atom was described in a semi-classical picture in three-step (see Fig. 2.1): around the peak of the electric field oscillation, the atomic potential can be perturbed enough to induce tunnel ionization of the electron wave-packet in the continuum (step 1); in this condition, the electron emitted with zero velocity is first accelerated away by the electric field and then, once the electric field changes direction, back to parent ion (step 2); finally, the accelerated electron has a certain probability of recombining with the ion (step 3). In the recombination there is a release of excess energy in the form of

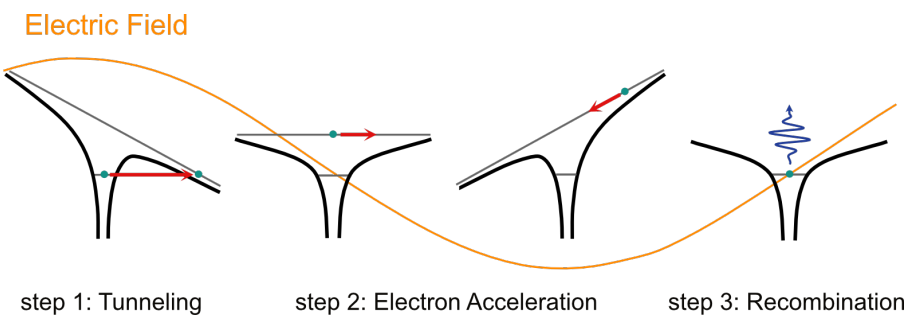

Figure 2.1: Schematic representation of the three-step model displaying the perturbed atomic potential during one optical cycle of the driving laser. In orange shown one optical cycle of the electric field.

high-energy photons. This is given by the gas Ionization Potential (I_P) plus the kinetic energy acquired by the electron when accelerated by the electric field. From energy conservation principles it is possible to retrieve the highest photon-energy generated as:

$$E_{cutoff} \approx I_P + 3.17U_P. \tag{2.1}$$

Equation 2.1 is known as cutoff law and was for the first time derived numerically by J. L. Krause and coworkers [148] and then interpreted semi-classically by P.B. Corkum [7]. U_P is the ponderomotive energy, which is the average kinetic energy of a free electron immersed in an oscillating electric field, and it is given by

$$U_P = \frac{e^2 E^2 \lambda^2}{16\pi^2 c^2}. \tag{2.2}$$

e is the charge of the electron, E is the electric field peak amplitude, c is the speed of light and λ is the wavelength of the driving pulse. The term $3.17U_P$ in eqn. 2.1 corresponds to the maximal kinetic energy of an electron born with zero velocity at the origin and returning to it. In the quantum-mechanical treatment of the HHG process, the cutoff law is slightly more complicated but numerically very close to the semi-classical one [8]. The efficiency of HHG is strongly dependent on the polarization of the driving pulse, such that the stronger the ellipticity, the less probable the recombination. This can be easily understood considering that, in the case of elliptically polarized light, the tunnel-ionized electron driven by the electric field will be displaced in the direction of the minor axis of the ellipse when it should recollide with the parent ion, therefore decreasing the recombination probability.
In the time domain, the three-step model indicates that the process allows the emission of high-energy photons at each half-optical cycle. At the same time, the high nonlinearity of the process is such to confine the event in a small temporal window close to the electric field maximum. This results in the emission of a train of pulses, each every half optical cycle (1.5 fs at 800 nm), intrinsically much shorter than an optical half-cycle and with a bandwidth that supports a pulse duration much lower than a femtosecond.

Moving to the spectral domain, the very first experimental investigations of HHG used short wavelengths in order to reach higher photon energy [144, 146], but the cutoff law 2.1 clearly shows an opposite trend, i.e. the highest photon energy generated increases linearly with the intensity (E^2) and, very importantly, quadratically with the wavelength. Both the intensity and the wavelength scaling law allow reaching a higher cutoff, each with its disadvantages. Great limitations in increasing the cutoff using higher intensities are due to unfavorable phase-matching conditions and depletion by ionization [150–153]. Typically, the highest cutoff for

a driving laser at 800 nm is around 70 eV in Argon or around 100 eV in Helium. Higher photon energies have been obtained [154–157], but typically with insufficient flux for spectroscopic application.

In order to exploit the wavelength scaling for reaching a higher cutoff, HHG drivers extending deeper into the short wavelength infrared (SWIR) spectral range (0.7 – 2.5 μm) are needed. As opposed to around 800 nm, where Ti:Sapphire sources operate, one must employ a series of non-linear frequency conversion steps to manufacture these extended SWIR pulses. This adds significant complications to producing the stable, high-energy, few-cycle pulses required for generating high-photon energy pulses. Additionally, a longer wavelength implies that in the HHG the electron wavepacket experiences more spatial spreading between the tunnel ionization and the recombination (step 2), significantly reducing the recombination probability and, therefore, the HHG conversion efficiency ($\approx \lambda^{-6}$) [153, 158]. To overcome these challenges much research has occurred in both the construction of ultrafast lasers sources in the SWIR, as well as in the implementation of high-gas-pressure HHG phase-matching configurations. The "Dramatic extension of the high-order harmonic cutoff by using a long-wavelength driving field" was experimentally demonstrated for the first time by B. Shan and Z. Chang in the 2002 [159]. In 2012 T. Popmintchev and coworkers obtained the impressive result of generating radiation up to 1.5 keV focusing a 3.9 μm beam into a Hollow-Core Fiber (HCF), but with a flux still insufficient for spectroscopic applications.

Pioneering work for the development of long wavelength sources and the overcome of the unfavorable wavelength scaling law was performed in my group at ICFO [39]. Engineering a high-pressure gas target for favorable phase-matching conditions for HHG, S. Cousin and coworkers demonstrated, using sub-2-cycles 1.85 μm pulses, the generation of radiation in the SXR region up to 500 eV with total photon flux that enabled transient absorption studies [39, 40, 60, 160]. Following this example, nowadays many groups reported similar results [161–165].

2.1.2. ISOLATED ATTOSECOND PULSES

As theoretically proposed for the first time by Gy. Farkas and Cs. Tóth in 1992 [166] and experimentally demonstrated by P. Paul and coauthors in 2001 [27], the HHG process allows for the generation of ultrashort pulses every half optical cycle, also referred to as Attosecond Pulses Train (APT). Given the interference between the multiple pulses produced, a typical APT spectrum is characterized by discrete peaks positioned at odd multiples of the driving laser frequency (see Fig. 2.2). Since the high-energy photons are generated just by the most intense half-

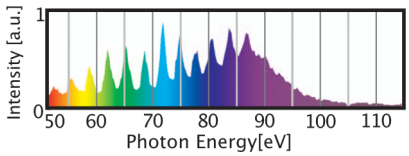

Figure 2.2: HHG spectrum obtained with a few-cycle NIR pulse [167] showing the typical discrete harmonics of an APT. The cutoff region (above 85 eV) is characterized by a continuum, symptom of a single attosecond pulse generated in that energy region. Adapted from [20].

cycle, in the case of few-cycles driving pulses the cutoff region can lose the shape of the discrete harmonic and appear as a continuum (above 85 eV in Fig. 2.2). Even though a number of experimental studies have been, and still are, performed using APT [72, 77, 127, 168], their application is limited to the cases where sub-fs resolution is not strictly needed. In order to generate IAP different gating techniques have been introduced, all based on the idea of exploiting the emission of just a half optical cycle of the driving pulse. For this purpose the stability of the Carrier-to-Envelope Phase (CEP) of the fundamental laser, i.e. the phase between the electric field and the intensity envelope, becomes crucial. Having a stable and adjustable CEP allows control of the electric field amplitude in the ultrashort temporal window in which the HHG takes place, enabling a handle over the temporal and spectral shape of the emitted radiation [58, 167, 169].

One way to isolate an attosecond pulse is to spectrally filter the cutoff region of the HHG emission where only the most intense half-cycle contributes (spectral gating). This technique enabled the first measurement with sub-fs resolution [26] but resulted efficient just for driving pulse duration close to one cycle. Additionally, this technique limited the minimum pulse duration because of the reduced bandwidth of the selected harmonics. The temporal gating, instead, points at temporally restricting the emission to a half-cycle. One possibility is to modulate the ellipticity of the driving pulse such as to have linearly polarized light in a limited temporal window [170, 171]. This can be implemented in the polarization gating [172–174] or double-optical gating [175, 176] schemes.
Another technique to obtain an IAP is the ionization gating [177, 178]. Here, a peak intensity high enough to saturate ionization of the emitting medium is used to restrict the phase-matching for high-harmonic generation to the leading edge of the driving pulse, with possible confinement to a single half-cycle [169]. The implementation of ionization gating in the SXR spectral region was theoretically and

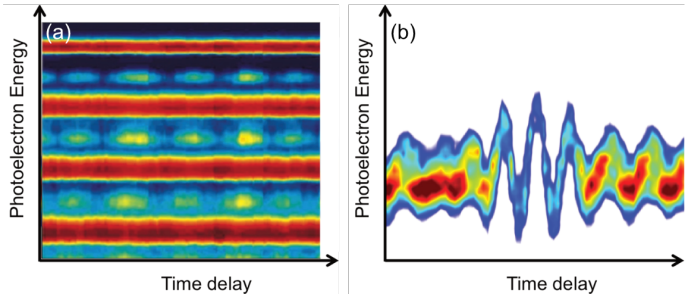

Figure 2.3: Examples of RABBITT (a) and Attosecond Streaking (b) traces. (a): RABBIT photoelectron spectrum as function of the delay between the APT and the fundamental pulse; note the amplitude of the oscillating sidebands between two next harmonics order as function of the delay (b): photoelectron signal following the shape of the vector potential of the fundamental pulse in an attosecond streaking measurement. Adapted from [24]

experimentally investigated for the first time by my group at ICFO [160]. In this work, Teichmann and coauthors showed that, using a sub-2-cycles 1.85 μm pulse, the temporal region for good phase-matching becomes narrower when increasing the pressure of the rare gas used for HHG, obtaining isolated attosecond pulses emission at 500 eV at helium pressures above 4bar.

2.1.3. TEMPORAL CHARACTERIZATION

The advancement of APT and IAP sources required the development of attosecond metrology to temporally characterize such pulses. The well-established techniques to retrieve phase and amplitude of the electric field, such as Frequency Resolved Optical Gating (FROG) [179], cannot be directly applied to XUV-SXR radiations because of the low flux and the unavailability of non-linear crystals transparent in this spectral region. In 2001, two experimental techniques were introduced, both based on the interaction of a replica of the HHG driver with the photoelectrons produced by the ionization of a target gas by the attosecond pulses.

The first temporal characterization of an APT was performed in 2001 [27]. The method used is known as Reconstruction of Attosecond Beating By Interference of Two photons Transitions (RABBITT) [180, 181] and it is based on two-photon two-color ionization of a target gas by one APT photon and one fundamental. The photoelectron spectrum produced by the APT is a replica of the harmonics spectrum with its discrete peaks separated by twice the photon energy of the fundamental pulse ($2\hbar\omega$) (see Fig. 2.3(a)). Upon the arrival of a weak fundamental pulse, the

photoelectron spectrum will show sidebands at $\pm\hbar\omega$, corresponding to the emission (-) or the absorption (+) of a photon. The signal originating from the absorption of a q-th harmonic photon and a fundamental one and the signal generated by the absorption of a $(q+1)$-th harmonic photon and the emission of a fundamental one contribute to the same sideband. These spectrally overlapping paths interfere producing a trace oscillating with periodicity twice the optical cycle (oscillating features in Fig. 2.3(a)). From this interference signal is possible to extract the phase difference between the different harmonics, thus allowing for a complete characterization of the APT.

In 2001, was also reported for the first time the method known as Attosecond Streaking [26] for the temporal characterization of IAP. The setup is similar to the previous case, except for the intensity of the fundamental pulse that in this case needs to be strong enough to impart a substantial momentum to the photoelectrons, but still weak enough to not ionize the target gas by itself. In these conditions, the vector potential of the fundamental pulse modulates in time the phase of the electron wavepacket and this corresponds to a shift in the energy of the photoelectron spectrum (see Fig. 2.3(b)) from which is possible to measure the duration of the IAP [29]. The action of the fundamental pulse in the attosecond streaking can be interpreted as a phase gate in FROG-like measurements [182] and as such took the name of FROG for Complete Reconstruction of Attosecond Bursts (FROG-CRAB). This analogy allowed to apply the same iterative inversion algorithms used for FROG to the FROG-CRAB traces, enabling complete temporal characterization of IAP [173, 183, 184].
While this technique is well-established in the XUV range, only a few measurements have been performed in the SXR [59, 161, 185]. The higher photon energy and the broader spectrum make the measurement much more challenging for different reasons[59, 186]: on one hand, the measurement is experimentally more difficult because of the lower flux and the smaller ionization cross-section; on the other hand, the central momentum approximation, commonly used for narrowband pulses in XUV, is not valid because of the broadband nature of the spectrum. Additionally, the much broader spectral component makes it harder to identify a target gas able to produce a photoelectron spectrum that is an exact replica of the one of IAP, i.e. whose dipole transition matrix element does not vary significantly over the energy range of interest, and that is not affected by higher-order ionization process, such as Auger processes [59].

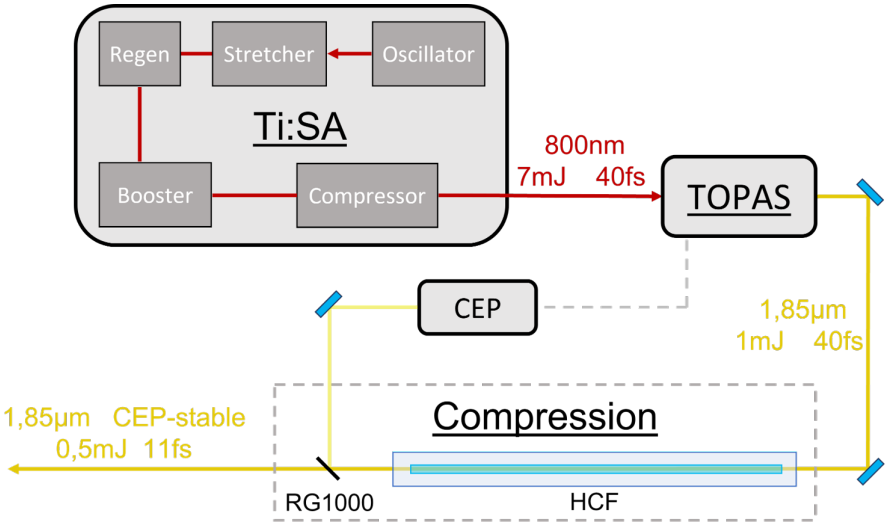

Figure 2.4: Schematic of the laser constituted of CPA-based Ti:Sa source, a TOPAS and a compression stage. The main pulse parameters are indicated after each of these stages. HCF: hollow-core fiber for spectral broadening; RG1000: IR filter for dispersion compensation.

2.2. CORE-LEVEL ATTOXAFS SETUP

In this section, I will present the experimental setup used for the generation and detection of the SXR IAP in our lab. To do so, first I will start describing the laser source used as a driver of the HHG and then I will show the SXR AttoXAFS Beamline, providing a characterization of the high-energy radiation obtained.

2.2.1. LASER SOURCE

From the discussion in section 2.1 it is possible to recognize the principal ingredients needed for the generation of an IAP in the water window spectral region through HHG, i.e. a few-cycle, high-intensity, CEP-stable source with a central wavelength longer than a commercial Titanium:Sapphire (Ti:Sa) system. The source exploited for the present work is based on a multi-mJ Ti:Sa system used to feed three Optical Parametric Amplification (OPA) stages (TOPAS in the figure) for wavelength conversion, plus a final compression stage to reduce the pulse duration to sub-2-cycles (Fig. 2.4). The Ti:Sa is a home-built system based on the well-established Chirped Pulse Amplification (CPA) scheme, in which the output of an

oscillator is stretched in time in order to reach high pulse energy in the amplification stages. The oscillator is a commercial system (Gecco Ultra - Laser Quantum) delivering an 11 fs nJ-level pulse at the repetition rate of 80 MHz and a central wavelength of 800 nm. This pulse is first spectrally reshaped by an acousto-optic programmable dispersive filter (Dazzler, Fastlite) and then temporally stretched to roughly 200 ps in the stretcher. This pulse is then used to seed the two amplification stages, namely a regenerative amplifier cavity (Regen) and then a multi-pass booster amplifier. Both amplification stages are in high vacuum (10^{-8} mbar) and are cooled by a high-power cryogenic system (Cryomech). This allows handling the high power delivered by the pump lasers without incurring in heating effects that could compromise the spatial and temporal properties of the beam. The Regen is 12 passes cavity characterized by a high amplification factor (nj → 2.1 mJ) and highly stable (<1% pulse-to-pulse instability) and spatially clean output mode. The Booster is a 2 passes cavity that further amplifies the 800 nm pulse to 11 mJ. The last stage of the Ti:Sa system is a reflective grating compressor that delivers a final pulse with 40 fs temporal duration, 7 mJ pulse energy, 0.7% pulse-to-pulse instability and 1 kHz repetition rate.

The good stability and high-quality spatial profile of the Ti:Sa output are crucial for the following wavelength conversion stage. This is a commercial set of three OPA stages (HE-TOPAS - Light Conversion) for downconversion of the 800 nm pulse to longer wavelengths. The system is designed in order to generate a signal beam ranging from 1.2 μm to 1.6 μm and an idler beam ranging from 1.6 μm to 2.6 μm. In the present design, these are set, respectively, to 1.3 μm and 1.85 μm. The 800 nm pump beam is split into three portions that are then used in the different stages. The lowest energy part (≈1%) goes to the first OPA where it is mixed in a beta barium borate (BBO) crystal with a temporally dispersed white-light continuum seed generated in a yttrium-aluminum-garnet (YAG). The temporal dispersion of the latter allows to fine adjust the wavelength of the amplified beam by means of the delay between the two pulses, here set for 1.3 μm. The resulting amplified beam, from now on referred to as signal, is then further amplified in a second BBO crystal where it is mixed in a collinear geometry with another portion of the 800 nm pump (≈9%). In this stage, the idler beam at 1.85 μm is generated through a Difference Frequency Generation (DFG) process that inherently ensures its CEP-stability. The third OPA is pumped by the remaining 90% of the 800 nm beam in order to boost the energy of the idler, resulting in a 1.85 μm, 1 mJ and CEP-stable pulse. This stage is set in a non-collinear geometry with a small angle that allows to spatially separate the pump, signal and idler in the far field.

The pulse energy and the wavelength of the idler beam already meet the re-

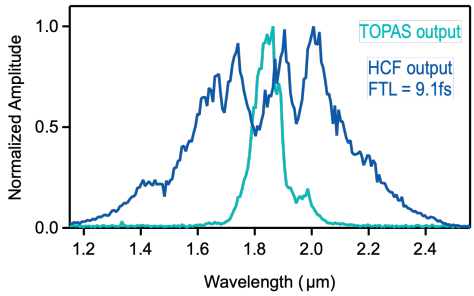

Figure 2.5: The broadening effects of the SPM in HCF filled with 1bar of argon. Measured spectra at the TOPAS output (cyan) and HCF output (blue) with an Indium Gallium Arsenide (InGaAs) spectrometer.

quirements for the generation of SXR-IAP, but the last step is needed in order to reduce its temporal duration. The compression is implemented through a well-established scheme of spectral broadening in Hollow-Core Fiber (HCF) filled with rare gas and dispersion compensation [187, 188]. When this is filled with 1bar of argon, the small core of the fiber (inner diameter 300 μm) ensures a peak intensity high enough to induce Self Phase Modulation (SPM) effects and generate a multi-octave-spanning spectrum (see Fig. 2.5. The propagation through the fiber temporally disperses the broad pulse with a positive chirp. While at 800 nm this is usually compensated using dichroic mirrors, at 1.85 μm the transmission through glass can provide the negative group velocity dispersion needed. Here, propagation through a 2 mm IR filter (RG1000, Schott) at Brewster angle allows the compression of the pulse to sub-2-cycles. The temporal characterization of the pulse is performed in a home-built Second-Harmonic FROG (SH-FROG) [179] where a pulse duration of 11.2 fs is retrieved (optical cycle at 1.85 μm is 6.2 fs) [39].

While the generation of the idler 1.85 μm beam through DFG in the TOPAS compensates for the random shot-to-shot phase fluctuations, its propagation can still cause CEP instability. In these conditions, the measured CEP roof-mean-square (rms) is roughly 300 mrads over an hour of measurement. For the generation of a stable SFX IAP essential for spectroscopic measurement, it is necessary to reduce it. This is obtained by implementing an f-2f interferometer that allows to measure a relative value of the CEP and whose fluctuations are used to generate a feedback loop acting on a delay stage of the TOPAS. The f-2f is fed with the residual reflection of the RG1000 filter used for dispersion compensation. The blue tail of the spectrum of this pulse around 900 nm interferes with the SH of its central wave-

length generated in a BBO crystal. The fluctuations of the resulting interference pattern are measured with a spectrometer and used as a feedback signal. Activating the feedback loop the rms is reduced to 88 mrads over an hour, so reaching the stability requirements for pump-probe measurements[39].

2.2.2. SXR ATTOXAFS BEAMLINE

The 1.85 μm, CEP-stable and sub-2-cycles pulse described in the previous section is exploited for the generation of SXR IAP by means of HHG (see section 2.1). In this section, I will present the SXR AttoXAFS beamline that allows the generation and propagation of the high photon energy pulse, together with a characterization of the source.

GENERATION AND DETECTION

A crucial point when dealing with photons in the XUV/SXR spectral domain is that these are strongly absorbed when propagating through any medium. For this reason, the whole experimental setup for the generation, propagation and detection of the radiation is kept in vacuum and no transmissive optics are used on the SXR optical path. The sub-2-cycles 1.85 μm pulse enters the beamline through a thin fused-silica window (FSW, 400 μm thick, glued on a metallic tube) at Brewster angle (55 degrees) that separates the optical table where the laser setup is placed from the vacuum chambers. The dispersion added by the transmission through this window is taken into account in order to have the shortest pulse where the HHG takes place.

The *Generation Chamber* (see Fig. 2.6) is the first of the five chambers that constitute the AttoXAFS beamline and, as the name suggests, it is where the SXR IAP is generated. This is obtained by tightly focusing the beam in a gas cell (GC) filled with Helium. A single attosecond pulse is obtained through ionization gating (see section 2.1.2) using high pressure of the emitting gas [160]. The design of the GC constitutes a key point of the vacuum system of the whole beamline. The main requirement is to have high pressure, on the order of 10 bar, in the region where the HHG takes place while keeping at the minimum the gas flow towards the chamber in order to avoid re-absorption of the SXR. The final design consists of a 0.5 mm long interaction region and two aligned laser drilled apertures of 200 μm diameter and 0.5 mm long (more details in [189, 190]). The gas is directly injected into the interaction region through a gas line where a mass flow controller (Bronkhost) is used for fine adjustment and stabilization of the pressure level. The vacuum is preserved using a mechanical booster pump (Leybold, 650 m^3/h), which allows to reach a pressure level 10^{-4} mbar in static conditions and mbar level when high-

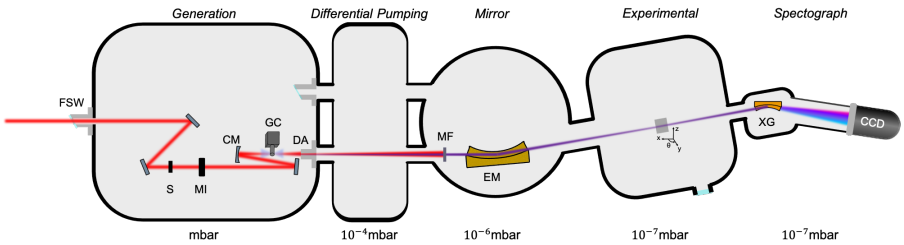

Figure 2.6: Sketch of the beamline for the generation and detection of SXR IAP. The beamline is entirely in vacuum and it is composed of 5 chambers (Generation, Differential Pumping, Mirror, Experimental and Spectrograph). The IR beam enters the first chamber through a fused-silica window (FSW) and then propagates through a motorized shutter (S) and iris (MI). It is focused in the gas cell (GC) filled with high-pressure Helium by a concave mirror (CM). Through a differential aperture (DA), the IR and the SXR co-propagates first in the differential pumping and then in the mirror chamber. Here a metallic filter (MF) is used either for calibration of the spectrograph or for removing the residual IR component. The SXR pulse is focused by an ellipsoidal mirror (EM) in the center of the experimental chamber. Finally, the X-rays grating (XG) diffracts the SXR pulse on a cooled charged-coupled device (CCD). More details in the text.

pressure Helium is injected into the chamber.

The laser beam is tightly focused in the interaction region by a concave mirror (CM) with 200 mm radius of curvature. A beam radius ($1/e^2$) of 25 μm allows for peak intensity higher than 5×10^{14} Wcm^{-2} at the focal plane, necessary for the generation of IAP in the SXR spectral region. Given the sensitivity of the HHG, a careful alignment of the beam through apertures is needed. This is achieved using a reference Helium-Neon laser (He-Ne) spatially overlapped with the 1.85 μm beam and an imaging system placed in the *Generation Chamber*. First, the He-Ne is picked after the GC by a movable mirror and aligned on the reference positions by means of two motorized mirrors, and then the GC, mounted on motorized stages for x-y-z control, is aligned on the beam allowing its transmission without clips. This procedure ensures good harmonics output, but still fine adjustment is needed directly optimizing the counts and/or the spectrum. Besides alignment, GC position with respect to the beam focus and gas pressure, another degree of freedom for harmonics optimization is given by a motorized iris (MI). Changes in the iris apertures act on the beam size and pulse energy at the focal plane, both affecting the peak intensity. This results in a very useful knob to fine-adjust the HHG to the everyday laser source conditions.

Given the size of the beam at the GC apertures (≈150 μm), it is likely to incur in ablation during the HHG optimization process. This causes an enlargement of the apertures and, hence, the optimal pressure conditions are lost. For this reason, the GC in this setup is a consumable that needs to be replaced every 2-3 months.

After its generation, the SXR is transmitted through an aperture (namely differential Aperture, DA) to the *Differential Pumping Chamber*. The DA has a diameter of 1 mm and a length of 1 cm, allowing the pressure to drop from the mbar level to the 10^{-5} mbar. This is placed as close as possible to the gas cell in order to reduce at the minimum the re-absorption of the high energy radiation. The 1.85 μm and the SXR pulses co-propagate through the aperture, but, given the extremely different divergence of the two, the former results heavily clipped while the latter does not. In the *Mirror Chamber* a metallic filter (MF) mounted on a motorized wheel is placed on the optical path. MFs are used for two purposes: spectral calibration of the spectrograph and filtering of the residual IR component. In the first case, metals with absorption edges in the generated bandwidth are needed, like Carbon (K-edge 284.5 eV) and Titanium (L_3-edge 454 eV). In the latter, a common choice is tin (Sn) or aluminium (Al) with 100 μm thickness that allows 50-70% transmission over the bandwidth of the high-energy radiation, while completely blocking the IR component. The motorized wheel allows to change or remove the filter in vacuum.

The SXR pulse is refocused by an ellipsoidal mirror (EM) (Carl Zeiss Laser Optics) coated with platinum and with a surface roughness lower than 0.5 nm. This is aligned at grazing incidence (2 degrees) to reduce losses and it is mounted on a motorized 6-axis hexapod positioner for full control of the translational and rotational degrees of freedom. This mirror has a 0.5 magnification factor and is placed at 1.4 m from the GC, such that the image plane, 0.7 m apart, corresponds to the center of the *Experimental Chamber*. Here, a 4-axis stage (Smaract) with sub-μm precision is exploited to align the sample onto the beam in transient absorption measurements. Detection of the SXR radiation is performed in a home-built *Spectrograph*. An X-rays Grating (XG) is mounted on a 2-axis manual stage that allows adjusting its position and angle in vacuum. The flat-field, aberration-corrected, gold-coated, reflecting concave grating (2400 lines/mm, Hitachi High Technologies America, Inc.) disperses the different wavelengths in the horizontal axis while re-imaging the center of the *Experimental Chamber* on the vertical axis. While the zero diffraction order is dumped, the first order is detected by a cooled charged-coupled device (CCD) camera (PIXIS-XO, Princeton Instruments, -75°C), connected to the grating chamber with a metallic bellow. The camera is positioned at the focal plane of the grating. The nominal resolving power of the spectrograph is E/dE = 1000, which translates into a spectral resolution of about 0.3 eV at 300 eV.

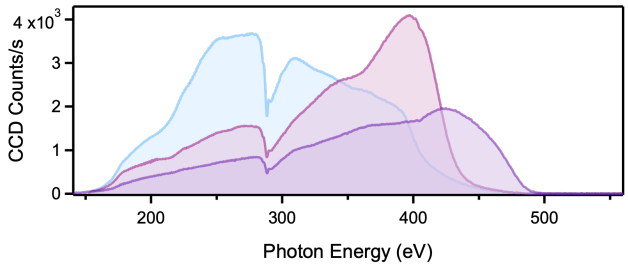

Figure 2.7: SXR spectra obtained with the setup described in section 2.2.2 optimized at the Carbon *K*-edge (light blue), Nitrogen *K*-edge (pink) and Titanium *L*-edge (violet). The spectra are measured as an average of 60 frames, each acquired with an exposure time of 40 seconds, and with a 100 nm Al filter placed before the XG.

CHARACTERIZATION

The setup described in the previous section allows to generate, on a daily basis, a SXR pulse covering the water window. The degrees of freedom at our disposal for HHG optimization, like GC position along the propagation axis of the driving pulse, CEP value or Helium pressure, allow to vary the phase-matching conditions and, hence, the shape of the generated spectrum, as shown in Fig. 2.7. The highest number of counts is usually obtained by optimizing the HHG in the low-energy region, while a broader spectrum reaching higher photon energy comes at the cost of lower efficiency.

In order to have an estimation of the flux of SXR source, the number of detected counts on the CCD (see Fig. 2.7) needs to be converted to the number of photons. The working conditions are such to generate 1 count/electron and each electron corresponds to 3.7 eV. This provides the number of photons/eV/s detected by the CCD, corresponding to a total of 3.9×10^4 photons/s detected by the camera for the light blue spectrum in Fig. 2.7. Taking into account the detection efficiency of the camera (40-60%), the grating efficiency (≈1.5%) and the Al filter transmission, we obtain $N_{ph} = 1.6\times10^7$ photons/s delivered to the experimental chamber. Knife edge measurements of the SXR pulse performed in the center of the experimental chamber show a $1/e^2$ beam size of 18 μm.

The conditions of peak intensity, pulse duration and gas pressure allow for the high-harmonics emission in a short temporal window, which ensures the generation of IAP in the SXR spectral region [160]. Experimental proofs of IAP come from attosecond lighthouse [40] and attosecond streaking experiments [59]. The lat-

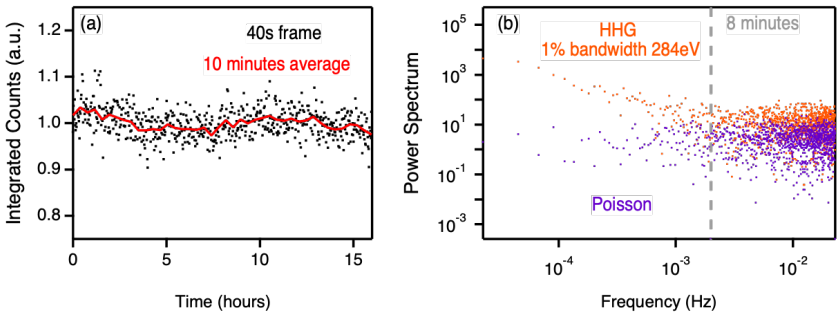

Figure 2.8: Stability characterization of the HHG source. (a): The long-term stability of the source characterized by evaluating the fluctuations of the integrated number of counts per 40 s frame over more than 15 hours; (b): Power spectrum of the integrated counts within the 1% bandwidth around the C K-edge (284 eV) (orange) compared to the one of shot-noise limited source (violet).

ter was performed in 2015/2016, constituting the first of this kind with such high photon energy and broad bandwidth. Given the difficulties encountered by the standard retrieving algorithms, in recent years a new approach to the problem was proposed by the group of prof. C.D. Lin that, analysing the overmentioned streaking trace, was able to assign a pulse duration of 165as [186]. On a daily basis, the absence of discrete harmonics peaks and the continuum shape of the spectrum are strong indications of the generation of IAP (see section 2.1.2).

Given the high non-linearity of the HHG process, small deviations of the laser source from the optimal conditions can translate in much stronger effects on the SXR pulse. In order to perform spectroscopic measurements, it is then crucial to evaluate the stability of the SXR source. First, we can consider the long-term stability, i.e. the capability of the source to maintain a stable flux over the long timescales needed for spectroscopic measurement. This is characterized by monitoring the total number of counts per frame acquired with an exposure time of 40 seconds and during a period of 15 hours. Fig. 2.7(a) shows a small decrease of the total counts over time with an overall standard deviation of only 3%.

Multiple sources contribute to noise, including detector readout noise, detector dark noise and the statistical fluctuations of the source; when the number of detected photons per frame has a Poissonian distribution then the detection is said shot-noise limited. This is a limit that cannot be overcome and is characterized by

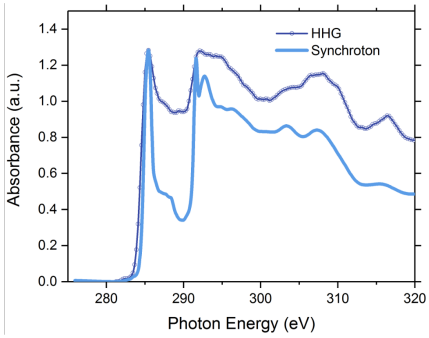

Figure 2.9: Comparison between the absorption spectrum collected in the lab with SXR AttoXAFS beamline and the data measured at a synchrotron SXR beamline for a 95 nm thick Highly Oriented Pyrolytic Graphite (HOPG) sample with the basal plane at 40 degrees respect to the linearly polarized SXR pulse.

fluctuations given by the square root of the number of detected photons. Starting from the average number of photons per frame, we can simulate the fluctuations of a shot-noise limited detection and compare it to the present case. This is typically done by evaluating the power spectrum, which is the Fourier transform (FT) of the detected number of photons per frame, over 1% bandwidth [191]. Fig. 2.7(b) shows the power spectrum of the data in Fig. 2.7(a) over the 1% bandwidth around the Carbon K-edge (284.5 eV). Clearly, by increasing the frequency of the measurement, i.e. reducing the exposure time, the fluctuations decrease till reaching the shot-noise limit for exposure time below several minutes. Transient absorption measurements require acquiring transmission spectra with (T_s) and without the sample (T_{ns}) (or with and without pump excitation, in case of time-resolved measurements) in order to retrieve the absorption spectrum as $-ln(T_s/T_{ns})$. Performing a series of measurements with integration time below the minute would then ensure to be working in shot-noise limited detection conditions.

Finally, in order to test the spectroscopic capabilities of the SXR AttoXAFS beamline, Fig. 2.9 shows a benchmark comparison between the static X-ray absorption spectrum of graphite measured in our beamline, alongside one measured using a synchrotron x-ray light source. In particular, we compare the absorption of a 95 nm thick flake of highly oriented pyrolytic graphite (HOPG) measured in our beamline to that of a total electron yield (TEY) measurement performed at the NAno Magnetism Unit (NAMU) beamline at the ALBA synchrotron. The basal plane is oriented at 40 degrees with respect to the linearly p-polarized X-ray pulse to allow

for the selective probing of bands with different orbital characters. The excellent agreement between the spectra proves the spectroscopic capabilities of the SXR AttoXAFS beamline in resolving the orbital character of samples.

2.2.3. SETUP FOR TIME-RESOLVED MEASUREMENTS

The SXR IAP described in the previous chapter is exploited as a probe in pump-probe time-resolved measurements. The setup to perform such experiments is described in the present section, together with a characterization of the pump pulse used for the measurements that will be presented in the following chapters. Afterward, the procedures for the optimization of the spatio-temporal overlap, data acquisition and analysis will be presented, providing the whole set of tools necessary for pump-probe experiments.

PUMP-PROBE SETUP

Time-resolved measurements performed with the AttoXAFS beamline are realized using a pump-probe scheme in which two optical pulses (pump and probe) combine on the sample with a controllable delay between each other. The probe is what provides a spectroscopic fingerprint; in the present case it is constituted by the SXR IAP pulse and the fingerprint is the transient absorption spectrum. The pump, instead, is the one that optically induces a change whose evolution will be tracked by the measurement. The properties of the pump beam are set according to the experiment to perform. Among the different kinds of setups implemented during my PhD, I will here present the one used for the measurement that is the core of this thesis and that will be presented in chapter 4.

A sketch of the pump-probe experimental setup is shown in Fig. 2.10. On the probe arm, i.e. the one described in detail in section 2.2.2, the only substantial difference with respect to the previous setup is the presence of a thin beam splitter (BS), which is the first optics on the path of the sub-2-cycles 1.85 μm beam in the beamline. It constitutes the beginning of a Mach-Zender interferometer splitting the beam into two portions: the probe (in transmission) and the pump (in reflection). The energy ratio between the two pulses depends on the BS used and is chosen according to the requirements of the experiment, with the most energetic part always used to drive the HHG. The IR pump beam is sent to a delay stage (DS) composed of two flat mirrors at 90 degrees and a linear positioner with nm resolution (Smaract). The DS allows controlling the temporal offset between pump and probe with attosecond accuracy. Afterward, the beam propagates towards the *Mirror Chamber* going through a FSW separating the *Generation* and *Differential Pumping Chambers*. The beam is focused through the combination of a diverging

(CaFl, f = -300 mm) and a converging (CaFl, f = 300 mm) lenses at a relative distance of 400 mm (respectively labeled as DL and CL in Fig. 2.10), corresponding to an effective focal length of 500 mm. This focusing scheme is used to achieve a smaller beam size at the focal plane and to reduce the losses on the holey mirror (HM) used for the recombination of the pump and probe beam. The HM is a 2 inches diameter mirror with a 3 mm hole in the center that transmits the SXR beam without clips and reflects IR one. After the HM, the two beams propagate in a collinear geometry and focus at the center of the *Experimental Chamber*. The collinear setup ensures the absence of any temporal smearing effects coming from the angle between the two beams, typically limiting the temporal resolution in non-collinear setups. Finally, a metallic filter (MF) placed before the X-rays grating (XG) reflects the pump while transmitting the probe.
In order to perform diagnostics measurements, e.g. for the optimization of the spatio-temporal overlap described in the following section, a movable pick-off mirror is placed after the center of the *Experimental Chamber* that sends the co-propagating beams to an imaging system mounted outside the vacuum chamber.

The presence of optics in transmission on the optical path of the pump beam (FSW, DL and CL) adds temporal dispersion. An in-situ SH-FROG measurement retrieved a temporal duration of 17 fs (see Fig. 2.11) in the experimental chamber,

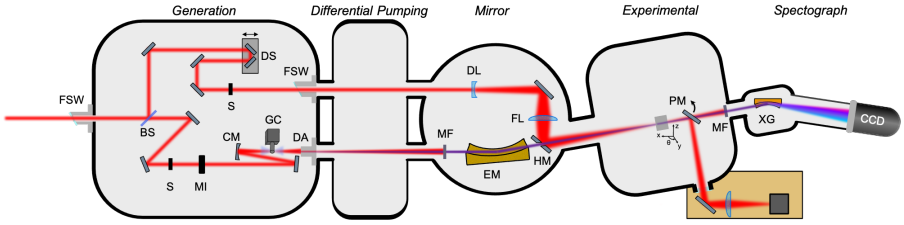

Figure 2.10: Sketch of the pump-probe setup for time-resolved AttoXAFS measurements. The beam is split into two portions, pump in reflection and probe in transmission, with a thin beam splitter (BS). The probe arm is described in section 2.2.2. The pump beam is sent to a delay stage (DS) and then propagates towards the Mirror Chamber going through a motorized shutter (S) and a fused-silica window (FSW). The beam is focused through a combination of a diverging (CaFl, f = -300 mm) and a converging (CaFl, f = 300 mm) lenses at a relative distance of 400 mm (DL and CL). The pump and probe beam are then recombined on a holey mirror (HM) and focused in the center of the Experimental chamber. Before the X-rays grating (XG), a metallic filter is placed to reflect the pump beam and transmit the probe one. A movable pick-off mirror (PM) can be used for diagnostics purposes. More details in the text.

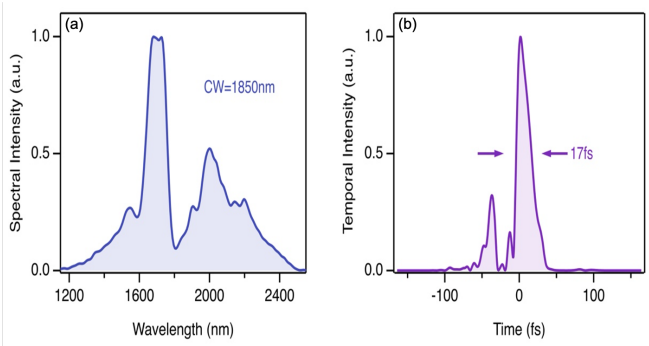

Figure 2.11: Spectral and temporal characterization of the pump beam in the *Experimental Chamber*. Measured spectrum with an InGaAs spectrometer (a) and retrieved temporal duration (b) from a SH-FROG measurement. Retrieved temporal Full-with half-maximum of 17 fs.

i.e. 5 fs longer than the pulse driving the HHG.
The collinear geometry comes at the cost of compromising the spatial and energetic properties of the pump beam because of the hole in the center of the HM that causes a doughnut-shaped beam profile in the far field. The focusing scheme used ensures a larger beam reflected by the HM, therefore attenuating these effects. A beam profile measurement revealed good spatial properties (75% ellipticity) and a beam radius ($1/e^2$) of 41 μm at the focal plane, which ensures a homogeneously excited area probed by the SXR pulse. With this scheme, 69% of the pump pulse energy after the BS is delivered to the *Experimental Chamber*.

The beamline is suitable for both solid-state and gas phase transient absorption studies. In the former case, thin flakes of samples (≈100 nm) are deposited on a metallic TEM grid and then placed in the sample holder (see Fig. 2.12(a)) mounted on the 4-axis stage in the center of the *Experimental Chamber*. The same stage is used also for gas-phase measurements. A gas-line with fine control of the backing pressure is used to deliver the sample to a gas cell mounted to the stage. As in the case of the generation of the SXR IAP (see section 2.2.2), also the design of this gas-cell required some engineering. The requirement is to reach a high enough density in the interaction region, i.e. inside the GC, while keeping the *Spectograph* at a pressure lower than 10^{-4} mbar. Decreasing the diameter of the input and output apertures reduces the gas flow to the chambers, but there is a drawback: the smaller the apertures, the more probable is to incur in gas cell clogging, especially when performing a strong-field measurement in organic samples, like the one de-

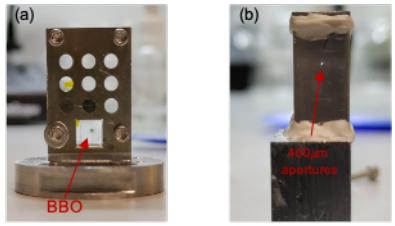

Figure 2.12: Sample holder for solid-state measurements (a) and gas cell for gas-phase samples delivery (b). The sample holder can contain up to 9 samples; on the bottom a 20 μm thin BBO crystal for temporal overlap in vacuum. The gas cell is 4 mm long, has 400 μm apertures and 1 mm thick walls.

scribed in chapter 4. The final design that allowed to perform pump-probe measurements in optimal conditions corresponds to a 4 mm long gas-cell with 1 mm thick walls and 400 μm apertures diameter (see Fig. 2.12(b)). With this setup, 30 mbar of backing pressure of Argon (Ar) allowed us to measure a 75% transmission drop at the Ar $L_{2,3}$-edges (245 eV), while keeping the *Spectograph* pressure at 10^{-5} mbar. The corresponding estimated pressure in the interaction region is ≈10 mbar.

SPATIO-TEMPORAL OVERLAP

Time-resolved measurements require the pump and probe beams to be spatially and temporally overlapped on the sample. The overlap accuracy can strongly influence the pump-induced signals and a well-established procedure to optimize it is required to have reproducible excitation conditions. The first step is always to fix the spatial overlap, being the temporal delay-sensitive to the alignment. Since the probe arm's optical path is fixed by the optimization of the HHG, the pump arm's degrees of freedom (DS position and alignment) are used for this purpose. The whole procedure takes advantage of the movable pick-off mirror (PM in Fig. 2.10) and the diagnostics setup outside the vacuum chamber (see Fig. 2.10), where either a beam-profiler, a spectrometer, or a power meter, is used. Depending on the parameters of the experiment, such as pump wavelength and intensity, the procedure can differ. In the following, I will present the one used for the gas-phase investigations that will be presented in section 3.3.2 and chapter 4.

In these experiments, we exploited a pump beam of 1.85 μm wavelength (see Fig. 2.11) with high intensity at the focal plane ($10^3/10^4$ Wcm^{-2}). The intensity is such that no physical reference can be placed on the beam path, hence making harder the alignment. The first step is to individuate the focal plane of the pump

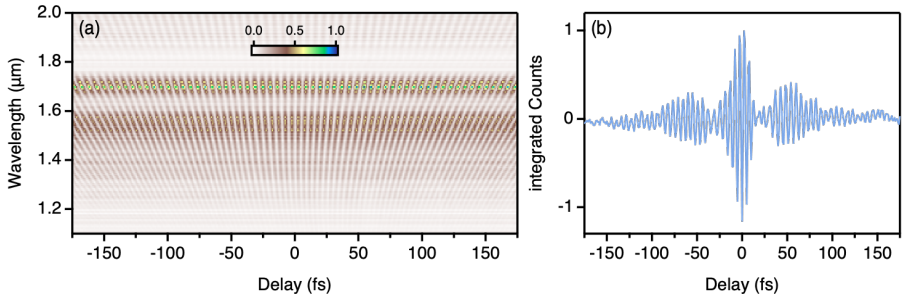

Figure 2.13: Interferometric measurement of the IR pump and the IR probe temporal overlap measured with an InGaAs spectrometer and performed with 1 fs temporal resolution. The plot in (b) shows the wavelength integrated version of the trace in (a). The stronger modulations in (b) define the optimal temporal overlap between the pulses. The data are normalized and scaled for visualization purposes.

beam and match it with the one of the SXR IAP. While the probe focal plane is found through a knife-edge measurement, the pump one is identified optimizing third harmonics generation in Ar in the gas cell. Moving the DL and the CL in the *Mirror Chamber* allows to match the pump's focal plane with the probe's one. The spatial alignment is then optimized using two motorized mirrors far away from each other, one being in the *Generation Chamber* and the other being the HM. Once the HM and the gas-cell's apertures are centered on the SXR beam, the iterative alignment procedure requires to use the first mirror to center the pump on the HM, looking at its doughnut shape with an IR beam-profiler (WincamD, Dataray), and the second to optimize the transmission through the gas-cell measured with a power meter. 3 mm away from the focal plane the pump beam is expected to be 4/5 times larger and, therefore, the optimal transmission through the apertures represents a strong constraint on the alignment.

Once the spatial alignment is optimized, the next step is to individuate the zero delay position of the DS. This is done by means of spectral interferometry between the pump and the residual IR beam on the probe arm. The two IR pulses are coupled into a fiber and the spectral modulations as function of the delay are detected with an InGaAs spectrometer. Stronger modulations of the integrated interference pattern (see Fig. 2.13) corresponds to the zero delay position of the DS used as a reference for time-resolved AttoXAFS measurements.

ACQUISITION AND ANALYSIS PROCEDURE

The first necessary step to perform a time-resolved measurement is to define the integration time needed. Starting from the assumption of a shot-noise limited detection and knowing the photon flux per pixel (see section 2.2.2), it is necessary to have an estimation of the amplitude of the signal. This is strongly sample and excitation dependent, but previous works show that this usually ranges between 1% and 10% [65, 72, 77]. Considering a 5% signal and an average photon flux detected by the X-rays CCD camera of 10^2 photons/pixel/s at the C K-edge (284 eV), a signal-to-noise ratio (S/N) of 10 corresponds to roughly 10 minutes of integration. Typically, a first "rough" measurement allows for a better estimation of the amplitude of the signal and of the exposure time needed.

A time-resolved measurement requires acquiring transmission spectra with and without pump excitation, respectively T_{pp} and T_p, with an estimated integration time of 10 minutes each. This needs to be repeated for each delay step. In order to work in shot-noise limited conditions, it is necessary to reduce the exposure time of the single acquisition (see section 2.2.2) and, given the integration time needed to reach a good level of S/N, this translates into the acquisition of multiple frames (N_f) for each delay, alternating with and without the pump excitation. In addition, a proper background subtraction requires recording spectra with the probe beam blocked, for the residual pump background (T_{pump}), and with both pulses blocked (T_{bkg}), for ambient noise reference. Finally, each delay requires the acquisition of 20-30 minutes, resulting in measurements lasting on the order of 1-3 days. The whole data acquisition procedure is managed through a home-built Labview software that remotely controls the DS, the shutters on the pump and probe paths and the CCD camera and that provides tools for the live monitoring of the signal and HHG performances.

Background subtracted pump-probe and probe-only spectra are obtained as $T_{pp}^{bkg} = T_{pp} - T_{pump}$ and $T_p^{bkg} = T_p - T_{bkg}$, respectively. Finally, the delta absorption can be constructed from the average of T_{pp}^{bkg} and T_p^{bkg} on the N_f frames as $\Delta A = -\ln \bar{T}_{pp}^{bkg} / \bar{T}_p^{bkg}$. Considering all the delays, the resulting trace is a 2D matrix with photon energy (E) and time (τ) dependencies, $\Delta A(E, \tau)$.

Because of the highly non-linear nature of the HHG process, also in optimal conditions the typical noise of attosecond transient absorption studies is in the order of 10^{-2}-10^{-3}, while transient absorption investigation in the visible and IR domain demonstrated a detection limit down to 10^{-5}-10^{-6} [192, 193]. Different noise suppression procedures can be applied to increase the S/N. Over the years,

my group developed a method based on the idea of using the probe-only spectra as references to reduce the frame-to-frame fluctuations between T_p^{bkg} and T_{pp}^{bkg}. To do so, each background subtracted pump-probe frame is normalized to the probe one acquired immediately before. The normalization area is composed of two regions, one above the absorption edge and one below, chosen to be away from the spectral range where pump-induced signals show up. The advantage of this procedure is that does not require sacrificing part of the photon flux for reference acquisition and can also be applied to pre-existing datasets.

In Fig. 2.14 I show the results of this procedure on a particularly noisy dataset corresponding to a time-resolved transient absorption measurement on a 95 nm thick HOPG sample. For this experiment the acquisition time of each frame is set to 40s with $N_f = 15$ and 110 delay steps (total acquisition time of 42 hours). The raw trace presents strong fluctuations (Fig. 2.14(a)) that are almost entirely suppressed in the normalized one (Fig. 2.14(b)). The noise level is estimated from the standard deviation over a region where no pump-induced signal appears (287.5 eV - 289.5 eV, shadowed orange area in the plot) and shows a reduction of a factor of 2.15 in the normalized case. Better noise suppression can be achieved by increasing the repetition frequency of the frames' acquisition.

A very interesting alternative approach has been recently proposed by R. Ge-

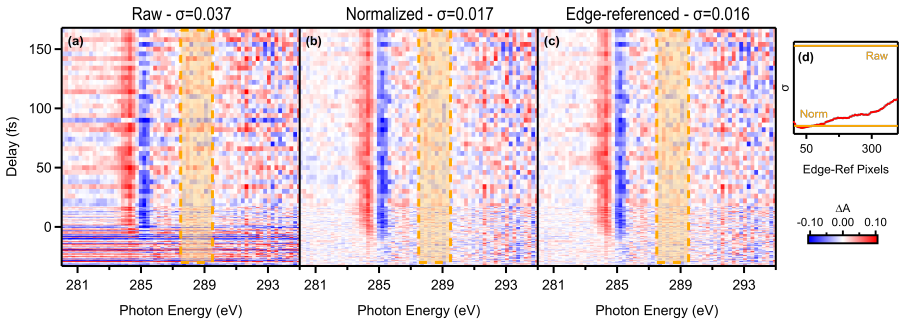

Figure 2.14: Noise suppression procedures. Time-resolved transient absorption measurement on a 95 nm thick HOPG sample pumped with 1.85 μm pulse with a fluence of 23 mJ/cm^2 and probe at the C K-edge. The standard deviation, σ, is calculated over the shadowed orange area in the plot (287.5 eV - 289.5 eV). (a): raw; (b): normalized; (c): edge-referenced with 34 referencing pixels (d): σ as function of the number of pixels used for edge-referencing.

neaux and coauthors [194]. This is based on edge-referencing techniques [195], where the probe-only spectra are used as a calibration dataset. Here, edge- referencing pixels in a spectral region where no pump-induced effects are present are used to build a correlation matrix that minimizes the residual noise. The noise suppression results of such procedure depend on the number of calibration frames, i.e. number of probe-only spectra over the whole dataset, and the number of pixels used for reference, with the constraint that the first has to be always larger than the second. In Fig. 2.14(c) the results on the same dataset presented above demonstrate that with the two procedures the same S/N level can be achieved. The standard deviation presents a minimum with a number of edge-referencing pixels equal to 34, as shown in Fig. 2.14(d).

Normalization or edge-referencing procedures are applied depending on which of the two shows better noise suppression on a specific dataset. Finally, 2D gaussian smoothing function with a width equal to 0.7 pixels is used in order to further reduce the noise level without losing spectral or temporal information.

2.3. CONCLUSIONS

The huge technological developments over the last 20 years enabled for the first time attosecond investigations in the water window. The generation of attosecond pulses in the water window and their application for spectroscopic purposes still requires non-trivial experimental efforts in which multiple consecutive steps of non-linear optics play a fundamental role. Just optimal working conditions at each of these stages allow to perform long time-resolved measurements with stable and reproducible conditions. More than ten years of experience leading the field of generation of attosecond pulses in the water window is a crucial and fundamental ingredient that grants our lab to have on a daily basis a source whose characteristics enable investigations like the ones presented in the following sections.

3

X-RAY SCIENCE

Besides allowing time-resolved investigations with an extreme temporal resolution, the technological breakthrough of the generation of attosecond pulses enabled to perform x-ray spectroscopy with table-top sources. The well-established x-rays capabilities of probing materials properties can now be exploited to investigate ultrafast non-equilibrium dynamics with attosecond resolution. The advantages of using high-energy radiation will be discussed in this chapter. In the first section, I will introduce x-rays science, briefly presenting the available sources of high-energy radiation (section 3.1.1) and their main spectroscopic applications (section 3.1.2). Afterward, in section 3.2, I will discuss in more detail the spectroscopic tool used for the present work, i.e. x-rays absorption fine structure spectroscopy. Finally, in 3.3 I will show static (3.3.1) and time-resolved (3.3.2) exemplary applications of such experimental method performed during my PhD.

3.1. INTRODUCTION

X-rays were discovered for the first time in 1895 and immediately became a fundamental tool for the investigation of matter. They are electromagnetic waves with wavelengths in the order of 10^{-9}-10^{-10}m. Their interaction with matter can be studied in terms of electron-photon interaction and two kinds of events can be considered: scattering or absorption. A scattering event, which can be either elastic or inelastic, occurs when a photon impinges on a sample, interacts with the electrons and then a photon with a different direction is emitted. In a crystal, this effect is known as diffraction. In the 1920s, the laws of x-ray diffraction from crystals and the capabilities to retrieve structural information with atomic resolution were already established [196–198]. In more recent times, the structure of proteins, and even functional units of living organisms, can be solved on a regular basis.
An absorption event, instead, occurs when, as the name suggests, the x-rays radiation is absorbed by the electron. Given the high photon energy of the radiation, this process generates a vacancy in a core electronic level that will be then filled in short times by transitions of electrons from higher ones. This series of processes produce a set of observables that contain electronic and structural information and on which are based the spectroscopic techniques described in section 3.1.2.

Even if x-rays absorption edges were discovered long before [199, 200], several decades of theoretical developments were needed till Sayers, Stern, and Lytle provided a consistent interpretation [201]. The development of the theoretical and experimental infrastructure for the comprehension of x-rays interaction with the matter was slowed down by the source limitations. Since the implementation of the first tube for x-rays emission in 1912, x-rays sources remained basically unchanged till the 1970s, when the first synchrotron radiations emitted from accelerated charged particles were obtained. This defined a huge improvement in the photon flux and sparked a series of technological innovations that still shows no sign of slowing down.

While UV, visible or IR spectroscopy probe transitions between valence or vibrational levels, x-rays radiation tracks the dynamics from a core orbital. This comes with many advantages. The core-to-valence transitions directly interrogate the electronic structure, while being strongly dependent on the reporting atom and, hence, providing site-specific information. Typically, the dependence of the core-level transitions on the dynamical processes following a valence excitation is small compared to the case of the valence-level ones. This translates into a tool able to directly probe the changes affecting the external orbitals. Moreover, due to the dependence on the reporting atom, these transitions are also sensitive

to internuclear distances and, therefore, provide information regarding dynamical structural changes and vibrational coherence of the system. Altogether, x-rays spectroscopy is a tool that allows extracting simultaneously the electronic and nuclear changes from the perspective of the reporting atoms. Among many others, site-specificity is extremely useful for tracking charge transfer [202] or charge migration dynamics [70] (see also section 4.3.3).

Crucial for time-resolved methods is the availability of an ultrashort x-rays pulse. For this purpose, in the following section, I will present the available sources delivering such pulses. Afterward, in section 3.1.2 I will focus on the different spectroscopic techniques that make use of x-rays radiation showing the set of information that each of them allows extracting.

3.1.1. X-RAYS SOURCES FOR TIME-RESOLVED STUDIES

Most of the x-rays investigations of matter have been historically performed at large-scale installations, like Synchrotron. In the last 20 years, the scientific community put a lot of effort into the development of table-top sources, like HHG and laser-plasma sources, that enabled these experiments also in a lab-based environment. In this section, I will briefly present the working principles and main properties, starting from the large-scale infrastructures that dominated the early years of x-rays science. More details can be found in reference [38, 203].

Synchroton is a specific type of particle accelerator and synchrotron radiation is a term that describes the radiation emitted by the charged particles traveling in applied magnetic fields, which force them to travel along curved paths. The emitted radiation is spectrally broad and a narrow-band region can be selected by means of monochromators. The emission is not continuous in time, but rather in the shape of "bunches", typically with a repetition rate in the order of MHz and a pulse duration of 50-150 ps. A better temporal resolution can be achieved through the "slicing" technique, which consists in exploiting an intense fs laser pulse co-propagating with the electron bunch. The interaction between the two generates bunches with the same temporal characteristics of the fs laser [204]. The drawback of this technique is that reduces the photon flux by almost three orders of magnitude.

These issues have been overcome with the advent of the Free Electron Lasers **FELs**. These are linear accelerators with "undulators" at their end, which can be hundreds of meters long. In this very large area, the electrons interact constructively with the generated x-rays radiation, resulting in "microbunching" with a

temporal duration of less than 100 fs, enhanced coherence and photon flux. The new generation of FELs is able to produce bunches as short as a few fs with pulse energy beyond the mJ level [205, 206]. Recently attosecond waveforms were measured in both the extreme ultraviolet [207] and in the soft X-ray spectral [208] regions, enabling the first x-rays experiments with attosecond resolutions in large-scale facilities [209].

However, for large-scale facilities practical difficulties for time-resolved measurements still remain, such as the tens of femtosecond jitter in synchronization or the large stochastic fluctuations of pulse duration and spectrum. These limitations, in addition to the cost and scarcity of beam time, have further motivated the development of laboratory-scale X-ray sources. An example is the **Laser-Produced Plasma** (LPP) source where an intense (>10^6 Wcm^{-2}) femtosecond pulse is focused on a metal target, resulting in the generation of plasma. The emitted electrons are accelerated by the electric field and interact with the target atoms, resulting in the emission of SXR of Hard x-rays (HXR) radiation. Typically, the radiation results in 100-50 fs long pulses with up to 10^7 photons/s [210], but is characterized by strong pulse-to-pulse intensity fluctuations. In an additional approach, spectacular progress has occurred on the spectral extension of **HHG** attosecond sources from the extreme ultraviolet to the soft X-ray photon energy, as deeply discussed in chapter 2.

These sources all differ in pulse duration, photon energy range, tunability, flux and other parameters, making one or the other more suitable according to the applications. Despite the reduced photon flux, the broad emission spectrum covering the water window spectral region, extreme temporal resolution and pulse-to-pulse stability are crucial benefits of HHG sources that in recent years enabled a number of experimental investigations [25]. Additionally, the great flexibility of implementation, easy control over the parameters and reduced costs are strong advantages with respect to large-scale facilities. At the same time, the accessible photon energy for time-resolved spectroscopic studies has been so far limited to less than 500 eV, while FEL and Synchroton easily access the 10 KeV range allowing to probe the K and L edges of heavy elements. Moreover, the high photon flux of the large-scale facilities can enable the implementation of non-linear x-rays spectroscopic techniques, but can also constitute a limit because of x-rays induced perturbation of the ground state.

3.1.2. X-RAY SPECTROSCOPY

Absorption of an x-ray photon by an electron enables different possibilities for spectroscopic investigations. The core-hole vacancy generated by this event can be filled by an electron from a higher energy level, resulting in a release of energy. Most of this is released as an emitted photon, but a portion can be transferred to an electron resulting in a further ionization of the medium. This second process is known as Auger decay, from which the name of the emitted electron, Auger-electron. Transmitted and emitted photons, as well as photoelectrons and photofragments, contain structural and electronic information of the sample and, in a pump-probe scheme, of its photo-induced dynamics. The spectroscopic methods are therefore defined by the detection scheme (see Fig. 3.1). In the following I will describe the most common ones.

Detecting the x-rays photons transmitted through the sample, it is possible to directly look at the absorption features, historically known as x-rays Absorption Fine Structures (**XAFS**). Depending on the spectral region where the analysis is focused, XAFS can be divided into Near-Edge XAFS (NEXAFS), also known as x-rays Absorption Near Edge Structure (**XANES**), and Extended-Edge XAFS (**EXAFS**). In the former case the core electron probes the valence orbital, while in the latter the information retrieved come from the photoelectron scattering. These two provide different and complementary sets of information that will be described more in detail in section 3.2, being this tool used for the spectroscopic investigations presented in this thesis.

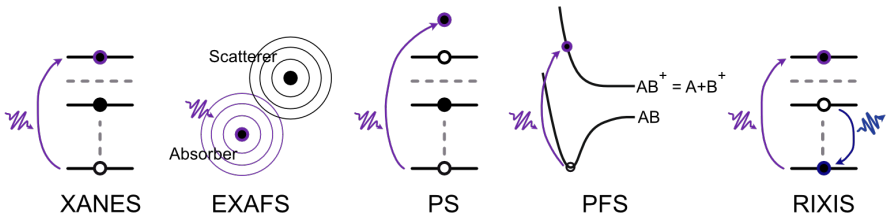

Figure 3.1: x-ray spectroscopic techniques used for time-resolved investigations involving charged particles or photon detection. In violet the transitions induced by an x-ray. Details of the different techniques in the text.

Replacing the photon detection scheme with a charged particle one, we can either detect electrons or ions. The former case is known as Photoelectron Spectroscopy (**PS**). It is possible to either detect the direct photoelectrons or the ones produced by Auger decay. Auger-electron intensity emitted by an atom in response to a core-level excitation is a direct measurement of the x-rays absorption coefficients and is exploited for time-resolved investigation of photoinduced dynamics [209, 211–213]. In the case of the direct photoelectrons, the effects of a photoinduced excitation are tracked by looking at the changes of the inner-shell binding energy that are particularly sensitive to charge-state or interfacial charge transfer. When dealing with solid-state sample, differently from the XAFS signal that is obtained through transmission in the bulk sample, PS surface sensitivity provides a good tool for investigation of surface and interfacial chemistry [214–216]. Besides the core-level study, the x-rays radiation can be used to trace the valence-state photoelectron emission [114, 115, 217–219]. In this case, the site-specific information of the core-level transitions is lost, but the high-photon energy allows to probe a large portion of the valence orbitals.

Photofragmentation spectroscopy (**PFS**), instead, traces the fragment ion produced by the absorption of an x-ray photon. This technique allowed to track the ultrafast charge migration dynamics of phenylalanine cation following a transition photoinduced by an XUV photon, probed projecting the system to a dication state by mean of a NIR pulse [36].

Once a core-hole is produced by an x-rays absorption, valence electrons can fill the vacancy and the consequent emitted photon can be detected as function of the absorbed photon energy. The difference between the incident and the emitted photon energy provides direct information on the valence transitions, minimizing the core-hole shifts that in complex systems can affect the XAFS. At the same time, the emitted photons' direction yields spatial information like in x-rays diffraction experiment. This spectroscopic technique is known as resonant inelastic x-rays scattering (**RIXS**) and its first application allowed the investigation of ligand-exchange dynamics in $Fe(CO)_5$ [220].

While XAFS and valence-level PS have been exploited for time-resolved studies with HHG sources, spectroscopic techniques that rely on secondary events, like RIXS and Auger-PES, have been so far limited to large-scale facilities due to the need for higher photon flux.

3.2. XAFS

The primary event to consider in an x-rays absorption process is the transition of a core-electron into a higher energy level. This transition is characterized by a final state with a core vacancy and an electron either in the continuum, i.e. a photoelectron, or in a previously unoccupied orbital. The latter case consists of excitation in the outer bound orbitals that, in the equilibrium condition, are excited states and, as such, energetically close to the transition to the continuum. If E is the x-rays photon energy, the transmission of an x-rays radiation through a sample is described by the Beer-Lambert equation:

$$I(E) = I_0(E)e^{\mu(E)x}. \tag{3.1}$$

I_0 and I are, respectively, the incident and transmitted radiation, μ is the absorption coefficient and x is the length of the interaction region. μ contains the information regarding the available transitions between the initial state i and the final one f:

$$\mu(E) = |\langle i|H|f\rangle|^2 \rho(E_f - E_i - E), \tag{3.2}$$

where H is the interaction term and ρ is the density of available states such that $E_f = E_i + E$. Equation 3.2 is known as Fermi's Golden rule and tells us that the absorption (as $ln(I_0/I)$ from eqn. 3.1) is characterized by a sharp rise in amplitude in the proximity of the binding energy of the core-electron, E_0, because of the sudden increase in the available transitions, as sketched in Fig. 3.2(a). The transitions are categorized by the core-level from which they occur. Absorption from the $1s$ orbital is labeled as K-edge, while the L_1-edge relates to the $2s$ level and $L_{2,3}$-edges to the $2p$ level. M_1, $M_{2,3}$ and $M_{4,5}$ correspond to the $3s$, $3p$ and $3d$, respectively. Higher edges can also exist and continue in the same fashion (see Fig. 3.2(b)). The edge multiplicity is given by $2j+1$, where j is the total angular momentum quantum number. Being the binding energy E_0 strongly element dependent ($\propto Z^2$, where Z is the atomic number), the absorption feature provides element-specific information.

A secondary event to take into account is photoelectron scattering. For E larger than the E_0, the photoelectron travels with a wave-vector k proportional to $\sqrt{E-E_0}$ and undergoes scattering processes on the neighbor atoms. This generates modulations of the absorption coefficient in a broad spectral region above the edge (in blue in Fig. 3.2(a)). While the spectral region close to E_0 can contain information regarding the electronic occupancy of bound states, the modulations in the higher energy region deliver information about coordination numbers and bond distances of the nearest neighbors of the absorbing atom, both in an element-specific fashion. As already mentioned in the previous section, the former region is

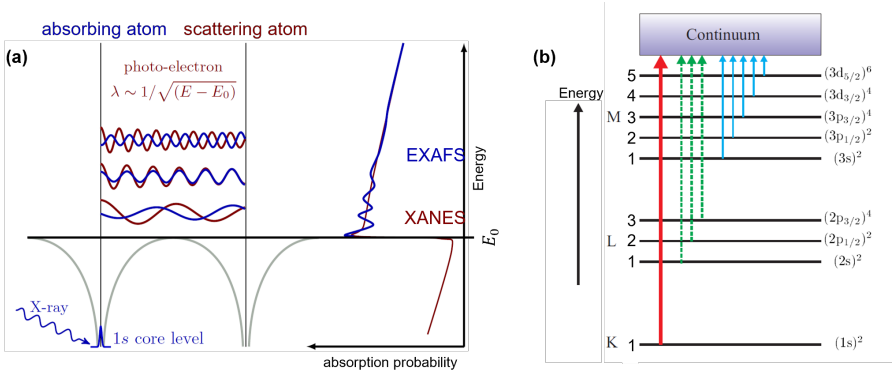

Figure 3.2: (a): schematic representation of XAFS spectroscopy. XAFS absorption can be divided into the "bare" atom part (in red) and a contribution coming from the photo-electrons that scatter from a neighboring atom (in blue). The scattered photo-electron can return to the absorbing atom, modulating the amplitude of the photo-electron wave-function at the absorbing atom. This in turn modulates the absorption coefficient causing the EXAFS. Adapted from [221]. (b): nomenclature used to label the absorption edges of elements. The electronic shells are labeled as $(nl_j)^{2j+1}$, where n, l and j are the principal, orbital angular momentum and total angular momentum quantum numbers, respectively. Adapted from [203].

known as XANES while the latter as EXAFS. A substantial experimental difference between the two is that, while near-edge investigations require to spectrally cover a region of 10-20 eV around the edge of interest, EXAFS necessarily relies on a much larger spectral coverage above the edge, so limiting its application to broadband sources.

In the two following two subsections, I will separately focus on these in order to describe their properties.

3.2.1. XANES

Transitions that define the XANES region of an absorption spectrum are described by the Golden rule 3.2. The interaction hamiltonian H, in the dipole approximation, can be written as $H = -e\vec{E} \cdot \vec{d}_{i\to f}$, where e is the electron charge, $\vec{E}$ is the x-rays electric field and $\vec{d}_{i\to f}$ is the dipole moment between the initial and the final state. This scalar product defines the selection rules, which depend on the radiation polarization and the symmetry of the final and initial states. The dipole

approximation is typically good for light elements and K absorption edges, while higher-order terms become not negligible when dealing with heavy elements, like in transition metal complexes [222], and more external edges [223]

In order to be the dipole term different from zero, the difference in the orbital quantum number l between the initial and final state must be $\Delta l = \pm 1$. Consequently, valence states with p-like symmetry can be probed by K- or L_1-edge transitions, while s- or d-type valence states can be accessed from the $L_{2,3}$ edge. When the dipole approximation breaks down, the quadrupole selection rules require $\Delta l = \pm 2$, therefore making available new transitions. On the other end, the scalar product is non-zero only if $\vec{E}$ has a non-zero component along $\vec{d}_{i \to f}$, therefore, introducing a relative orientation dependence, which is particularly relevant for samples with crystalline structure [60].

The energy width of a transition is given by the lifetime of the created excited states, like the core-vacancy states induced by an x-rays radiation absorption (typically in the order of femtoseconds). Following the uncertainty principle, this generates a Lorentzian broadening of the X-ray absorption spectrum, which, on the one end, constitutes the ultimate spectral resolution of XANES (1 fs $\rightarrow$ 0.6 eV) and, on the other, can be affected by changes to the atomic environment. Chemical changes, for example induced by a pump pulse in a time-resolved measurement, can also alter the electron screening and, hence, cause a core-hole energy shift. Additionally, the presence of a core-hole can strongly affect the electronic occupancy of the various orbitals, especially the one spatially localized on the core atomic-like one. This alteration is known as multiplet effect and can make interpretation of the X-ray absorption spectrum, and identification of valence electronic dynamics, extremely difficult without the theoretical means to disentangle these effects [55, 224]. As a general principle, these effects scale very poorly for higher order core-shells and increase very quickly the difficulty of accurate interpretation of the underlying dynamics [37, 56, 225]. K- and L-edges minimize such ambiguities and are thus the established transitions used in x-ray spectroscopy.

In order to have a proper S/N, the sample concentration has to be set such as to have efficient interaction with the x-rays radiation, but without excessively reducing the number of photons transmitted. The rule generally accepted in the XAFS community is to set a concentration such that the interaction region corresponds to one absorption length, i.e. a drop after the edge of a factor 1/e in the number of photons.

3.2.2. EXAFS

To take into account the photoelectron scattering effect on the absorption spectrum, the final state in eqn. 3.2 can be expanded as $|f\rangle = |f_0\rangle + |\Delta f\rangle$, where the first term is the "bare-atom" part and the second corresponds to the effect of the neighboring atom:

$$\mu(E) \propto |\langle i|H|f_0\rangle|^2 \left[1 + \langle i|H|\Delta f\rangle \frac{\langle f_0|H|i\rangle^*}{|\langle i|H|f_0\rangle|^2} + C.C.\right], \tag{3.3}$$

where $C.C.$ stands for complex conjugate. This can be rewritten in the following form:

$$\mu(E) = \mu_0(E)\left[1 + \chi(E)\right], \tag{3.4}$$

where μ_0 is the absorption in absence of neighboring atoms and χ takes into account the modulation effects. In its simplified form [221], the interference term as function of the wave-vector k is given by:

$$\chi(k) = \sum_j \frac{N_j f_j(k) e^{-2k^2\sigma_j^2}}{kR_j^2} sin\left[2kR_j + \delta_j(k)\right]. \tag{3.5}$$

The sum is done over the different shells labeled with j. f is the scattering amplitude of the emitted photoelectron, N_j is the number of neighboring atoms in the $j-th$ shell and R_j is their distance from the absorbing one. σ_j^2 is the disorder in the neighboring distance, which has a damping effect on the modulation amplitude. Finally, $\delta_j(k)$ is the scattering phase factor for the shell j. Though its complicated shape, the EXAFS eqn. 3.5 clearly shows the sinusoidal term $sin\left[2kR_j + \delta_j(k)\right]$, responsible for the modulations in the absorption spectrum (in blue in Fig. 3.2(a)). The most significant approximation made to obtain eqn. 3.5 is to not consider inelastic scattering of photoelectrons and the finite lifetime of the core-hole state. Taking into account these effects, a damping term is added to the equation depending on the mean free path of the photoelectron, i.e. how far it can in average travel before it scatters inelastically or the hole is filled. This is typically in the order of 5 to 30 Å and depends on the wave-vector k [221].

Starting from an XAFS absorption spectrum, it is possible to retrieve the distance of the first nearest neighbor and its coordination number. The interference signal is obtained from the measured spectrum removing the "bare" atom absorption contribution by means of a polynomial fit, normalizing the edge jump and converting photon energy into wave-vector values. Once known scattering amplitudes $f(k)$ and the phase-shift $\delta(k)$ [226], a Fourier Analysis allows to determine the absorber-backscatterer distance.

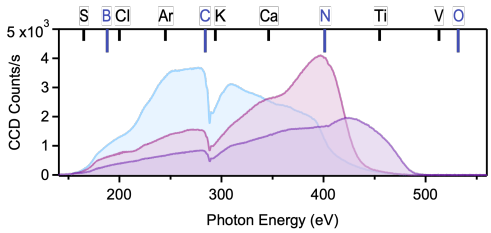

Figure 3.3: SXR spectra obtained with the setup described in section 2.2.2 optimized at the Carbon *K*-edge (light blue), Nitrogen *K*-edge (pink) and Titanium *L*-edge (violet). The spectra are measured as an average of 60 frames, each acquired with an exposure time of 40 seconds, and with a 100 nm Al filter placed before the x-rays Grating (see pump-probe setup in Fig. 2.10). On the top the *K*-edges (in dark blue) and the *L*-edges (in black) covered by the SXR spectrum. Clear carbon contamination is detected in correspondence of the C *K*-edge.

3.3. ATTOXAFS AT ICFO

In chapter 2 I described the experimental setup implemented in our lab that allows performing time-resolved measurements, exploiting a broadband SXR IAP to probe the ultrafast dynamics. In Fig. 3.3 I show the spectrum of this pulse that ranges from 150 eV to 500 eV, superimposing the *K*- and *L*-edges present in this region. This spectral region is of particular spectroscopic interest for the investigation of organic systems, because of the presence of C *K*-edge (284 eV) and water transparency up to Oxygen *K*-edge (532 eV) (for this known as *water window* region). The spectrum covers multiple absorption edges of spectroscopic interest, like *K*-edges of Boron, Carbon, Nitrogen and Oxygen (in dark blue on the top of Fig 3.3), considered as the building blocks of most of the biological compounds, and several *L*-edges (like Titanium, Vanadium, Chlorine, Argon, etc...) (in black).

The broadband nature of the attosecond SXR pulse allows performing XANES investigations on multiple edges, as well as EXAFS study. The spectroscopic capabilities of the source have been recently demonstrated in static [60] and time-resolved studies [63] on highly-oriented pyrolitic graphite (HOPG). The former proved the possibility to apply EXAFS spectroscopy with an HHG table-top source, while the latter constituted the first *K*-edge time-resolved investigation of solid state samples with attosecond resolution. It demonstrated the ability to track energy flow upon light absorption between electrons, holes and phonons in real-time and the capability to disentangle coherent and incoherent excitation and dissipation pathways from the attosecond to the picosecond time scales.

In the next two subsections, I will present static and time-resolved measurements performed during my PhD with the aim of showing with practical examples the element-specific electronic and nuclear information that a XANES measurement can provide.

3.3.1. STATIC MEASUREMENTS

Utilizing attosecond pulses to perform time-resolved XAFS measurements provides the ability to probe ultrafast non-equilibrium electronic dynamics. Additionally, the ultrabroad bandwidth gives the possibility to cover multiple absorption edges at the same time. In order to show the kind of physics that can be retrieved with such a spectroscopic tool, in Fig. 3.4 I present the x-ray absorption spectra from three solid-state samples, HOPG, hexagonal boron nitride (hBN) and titanium disulfide (TiS_2), measured with the SXR AttoXAFS beamline at ICFO. Each sample represents a uniquely different class of solid-state materials with different properties.

Figure 3.4(a) shows the X-ray absorption profile of HOPG. This consists of equally oriented graphene layers bound through Van der Waals forces. In each of these, the

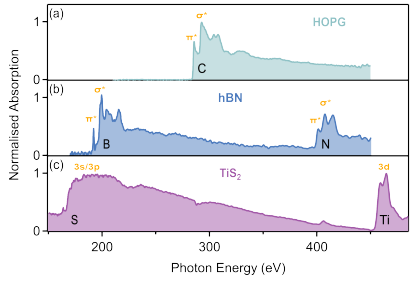

Figure 3.4: X-ray absorption spectra with broadband SXR attosecond pulse at ICFO. The static X-ray absorption spectra from (a) highly-oriented pyrolitic graphite (HOPG), (b) hexagonal Boron Nitride (hBN), and (c) Titanium Disulfide (TiS_2). The samples are around 100 nm thick and placed at 40 degrees with respect to the polarization axis of the SXR probe. Labeled within each panel are the valence-level (in orange) and the core-level (in black) orbital natures of the absorption peaks.

carbon atoms form a hexagonal lattice through strong covalent bondings. The four carbon valence shell electrons undergo hybridization to form the band structure. Three of these electrons form covalent bonds through an sp^2 hybridization while the fourth has p_z symmetry with an orientation perpendicular to the graphene plane. The sp^2 orbitals form in-plane σ states while the p_z leads to the formation of a π state. The graphite conduction band consists of antibonding π^* and σ^* states and the XANES structure at the carbon K-edge arises from the transitions of the $1s$ core-shell electron to the unoccupied π^* and σ^* states. Given the orientation of the π^* and σ^* states with respect to the graphene planes, the sample is placed at 40 degrees with respect to the polarization axis of the SXR probe in order to simultaneously probe the in-plane and out-of-plane orbitals. These two conduction band states are clearly distinguishable in the X-ray absorption profile.

The absorption spectra of hBN and TiS_2 clearly show the importance of probing multiple edges. Starting from the former, the lattice structure of hBN also consists of individual hexagonal layers bound through Van der Waals interactions. As in graphite, the conduction band of hBN contains π^* and σ^* states. Figure 3.4(b) shows that these states are visible in the x-rays absorption profile in both the boron K-edge, near 193 eV, and the nitrogen K-edge, near 400 eV. Interestingly, the top of the valence band (π) is primarily composed of nitrogen $2p$ orbitals, while the bottom of the conduction band (π^*) of boron $2p$ orbitals[227]. Therefore, the extreme bandwidth of the SXR pulse provides the possibility to track the optical excitation from valence bands to conduction bands in real time, recording the ultrafast correlations and electronic dynamics within the bands, all in one shot. Difficulties, such as repeating measurements while scanning probe photon energy and maintaining experimental conditions typical of large-scale facilities, are inherently avoided.

Finally, 3.4(c) shows the x-rays absorption profile of TMDC TiS_2. Transition metal dichalcogenides (TMDCs) are an exciting class of 2D materials in which correlated carrier properties could be exploited for novel optoelectronic functions or for high-density energy storage[228, 229]. In TMDCs, the properties of the material nearly exclusively arise from the partially-filled d-orbitals, which also exhibit strong spin-orbit coupling. In particular, TiS_2 has a trilayered structure where hexagonal sheets of $Ti^{4+}(3d^0)$ atoms are sandwiched between sheets of S atoms. While the atoms within the trilayer are covalently bonded, the different trilayers bond to each other via Van der Waals forces. Since the conduction band has nearly exclusively Ti $3d$ character, it can be conveniently probed at the Ti $L_{2,3}$-edge at around 460 eV. The valence band, instead, is mainly composed by mixed sulfur $3s$ and $3p$ states and can be accessed at the S $L_{2,3}$-edge at 160 eV. It is worth noting that the presence of two possible dipole-allowed core transitions, L_2 and L_3,

clearly manifests itself in two separate peaks at the Ti edge. Recently, my group resolved with sub-femtosecond precision the effect of an IR excitation on TiS_2 at the Ti $L_{2,3}$-edge [62].

3.3.2. DRESSING EFFECTS ON X-RAYS INDUCED POLARIZATION

In conventional attosecond transient absorption spectroscopy (ATAS), x-rays pulses are used for their capability of tracing through the core-level absorption the effects induced by a NIR/IR pump. In this framework, the interesting dynamics, revealing the relaxation pathways following the excitation, are restricted to the condition in which the pump pulse precedes the probe one. This standard way of thinking at ATAS experiments is not the only possible and a number of works have been performed inverting the roles of the NIR/IR and x-rays pulses, in atomic [44, 45, 48, 168, 230, 231] and, more recently, in molecular systems [232].
Following these examples, during my PhD we performed a benchmark time-resolved measurement in Argon. Before showing the results of this measurement, in the following I will briefly introduce the physics that can be retrieved from these experiments.

Let us consider the situation of the x-rays pulse impinging the sample before the NIR/IR one. The absorption of the broad attosecond pulse (pump) induces a polarization of the medium that can then be altered by the interaction with the NIR/IR one (probe). In this case, the NIR/IR pulse acts as a "control pulse", dressing the system and thus dynamically changing its absorption around the absorption edge. The final absorption signal resolved in the spectrometer is the result of the interference between the sample emission, originating from the oscillating dipole induced by the x-rays pulse and perturbed by the NIR/IR one, and the transmitted broadband pulse. This is possible because the x-rays induced polarization persists on a timescale that depends on the lifetime of the core-level excited states, which can vary from a few fs to ns, depending on the nature of the state.

Figure 3.5(a) shows a typical ATAS spectrogram calculated in Helium (He) using an IAP as pump and IR pulse with a photon energy of 1.5 eV and peak intensity of 3×10^{12} W/cm^2 [43]. Negative delays correspond to x-rays pulse first, opposite to the usual convention. Here, the attosecond pulse excites the $1s$ electron into a manifold of states, namely the $2p$, $3p$, $4p$ and $5p$, below the ionization threshold (I_p). At large positive delays there are no time-dependent features because the IR pulse arrives before the x-rays-induced polarization is created.

At negative delays, before the overlap region, there are sidebands whose spec-

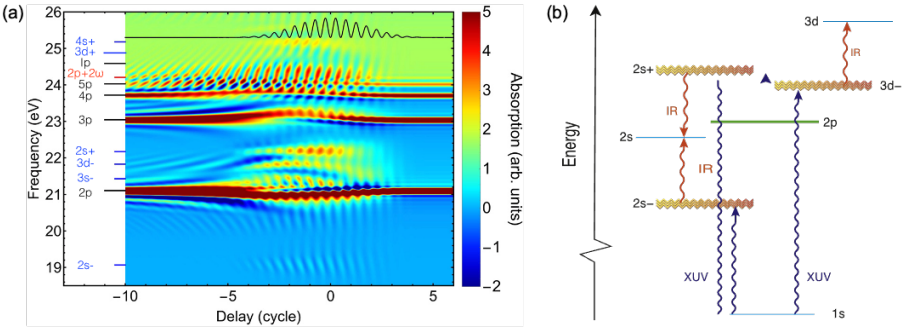

Figure 3.5: (a): typical ATAS spectrogram calculated in Helium using a broadband attosecond pulse with photon energy centered at 25 eV as pump and IR pulse with a photon energy of 1.5 eV and peak intensity of 3×10^{12} W/cm^2. Negative delay means x-rays pulse first. On the left, in black the bright states probed by the attosecond pulse in absence of NIR dressing (np) and in blue the light-induced states (LISs). (b): schematic diagram for LISs. In green the bright states, in light blue the dark states and in yellow the LISs. Adapted from [43]

tral position results time-dependent. These structures originate by the coupling of the np states with nearby ns or nd states, due to the presence of the NIR. The hyperbolic time-dependent behavior comes from the initial phase of the excited states wavepacket that changes according to the delay between the two pulses as $\omega\tau$, where ω is the characteristic frequency of the nd or ns state and τ is the delay.

In the overlap region, there are two characteristic phenomena, coupling between states induced by the NIR pulse and sub-cycles oscillations. The first ones are new features that rise just when the two pulses are overlapped and can be interpreted as IR-induced coupling to a dark state (ns/nd) that involves either the emission or the absorption of an IR photon, as schematically shown in Fig3.5(b). The phenomenon can be interpreted as a two-photon resonant process (1 x-rays + 1 NIR) with a net population transfer from the core-level state to the dark state. LISs can be recognized by their energy separation from the dark states ($2s$) that corresponds to exactly one NIR photon ($2s+$ and $2s-$ in the figure). The condition for this process to happen is that the distance between the dark state and the bright one (np) is different from one NIR photon energy. In resonant conditions, instead, an effect that can take place is Autler-Townes splitting[233]. This consists of the splitting of the bright state feature in a doublet as a result of the strong-field coupling between the states. Moreover, LISs can appear also for resonant two-photon coupling from the populated bright state.

Additionally, periodic modulations are clearly visible on multiple absorption lines. These are interpreted as interference between states that are two NIR photons apart, but that lead to the same final state, like in the case of LIS $2s-$ and $2s+$ that leads to the same dark state ($2s$). Oscillations can then appear on both the final state ($2s$) or the intermediate ones ($2s-$ and $2s+$) and are characterized by a periodicity of half IR optical cycle. Another example of this phenomenon in Fig. 3.5(a) is the modulation of the $5p$ absorption line that is two photons apart from the $2p$ one.

Finally, when the x-rays pulse precedes or overlaps with the NIR, the latter can modify the shape of the absorption line (note the shape difference for the np states between large positive delays and large negative ones). This is interpreted in terms of a Stark shift of a bright state due to the IR-induced phase shift of the dipole moment state. This translates into a shift of the central frequency of the absorption line [234, 235] that depends on the IR intensity and duration, and is therefore delay-dependent. In the condition of weak coupling with the nearby states, this is equivalent to the ponderomotive energy of the pulse [47]. Additionally, in the region in which the NIR pulse follows the IAP, the reshaping of the absorption lines provides a way to retrieve the lifetime of core-level excited states [42, 49].

STRONG-FIELD INDUCED EFFECTS IN ARGON AT THE $L_{2,3}$-EDGE

In 2019 we performed the first ATAS measurement on a gas-phase sample done in our lab aimed at investigating the sub-cycles dynamics of the autoionizing states of argon at the $L_{2,3}$-edge. A similar measurement had been previously published by the group of Professor Zenghu Chang [45]. In this work, the comparison between the experimental data and simulations allowed the coauthors to recognize the appearance of LISs, Stark shift effects and sub-cycles oscillations. The nature of these processes is such to strongly constrain their effects to the temporal overlap between the pump and the probe pulse and, hence, provides a tool to directly evaluate the temporal overlap between the two pulses at the interaction region with sub-fs precision. Therefore, argon constituted a perfect system to exactly define the time "0" for a time-resolved measurement and to benchmark our capability to resolve sub-cycle dynamics and strong-field effects in gas-phase samples against a well-studied case.

For this measurement, the pump-probe setup used is the one presented in section 2.2.3, with a pump pulse intensity of 10^{13} W/cm^2, central wavelength of 1.85 μm and duration of 17 fs, corresponding to ponderomotive energy of roughly 3 eV (see eqn. 2.2). With a backing pressure of 30 mbar, the ΔA signal resulted to be as high as 0.3, much higher than the typical values in non-atomic systems. This

allowed reaching a good level of S/N acquiring 8 frames of 60 s integration for the pumped and unpumped cases, for each delay step. The ΔA trace was obtained by applying the normalization noise suppression procedure described in section 2.2.3. The measurement was performed on a temporal window of 30 fs around the pump-probe overlap, with a step size of 500as, for a total of roughly 20 hours of acquisition.

In the vicinity of $2p$ ionization potential, argon presents a series of autoionizing states, as shown on the left in Fig. 3.6. The series starts with the lowest state being the $4s$, followed by $5s/3d$, $6s/4d$ and $7s/5d$. Because of the strong spin-orbit splitting (≈2 eV), the transitions from the $2p_{1/2}$ and $2p_{3/2}$ core-levels are shifted, with the result that the resonance into the 4s state is the only one from the $2p_{1/2}$ core-electron before the L_3 ionization threshold. The lifetime of these core-level excited states due to Auger electron emission is in the order of 1-10 fs (5.44 fs for $2p^{3/2}4s$) and, hence, in the resolution of the experiment. Worth to note also the presence of the $4p$, $5p$ and $6p$ states whose transitions from the $L_{2,3}$-edge are forbidden for the selection rules (see section 3.2.1), i.e. dark states. In Fig. 3.6(a) I show the transmission spectrum of argon, with (blue) and without (red) the pump excitation. In the red curve clearly distinguishable the three strongest resonances that correspond to $2p_{1/2}\rightarrow 4s$ (244.2 eV), $2p_{1/2}\rightarrow 5s/3d$ (247 eV) and $2p_{3/2}\rightarrow 5s/3d$ (249.2 eV). The blue curve clearly shows the effects of the dressing field appearing

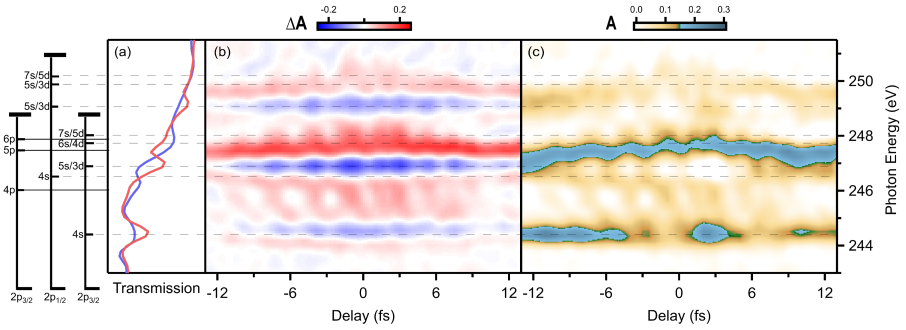

Figure 3.6: Strong-field effects in Argon at the $L_{2,3}$-edge induced by a 1.85 μm pump pulse with a peak intensity of 10^{13} W/cm^2 and resolved with a 500as delay step size. On the left argon absorption lines at the $L_{2,3}$-edge (dotted line: bright state; continuous line: dark state). (a): x-rays transmission with (blue) and without (red) the pump excitation. The pump-excited one is the time average of the spectra acquired between -5 fs and 5 fs. (b) and (c): respectively, time-resolved differential absorption (ΔA) and absorption (A) traces.

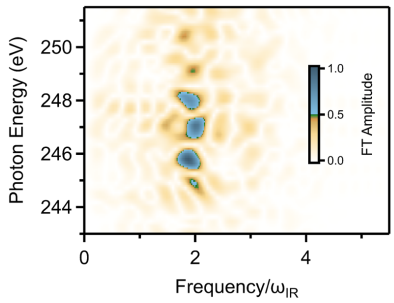

Figure 3.7: Fourier analysis of the ΔA trace in Fig. 3.6 showing half IR optical cycle periodic components. The frequency is shown in ω_{IR} unit, where ω_{IR} is the frequency of the dressing IR pulse.

as a shift and/or a disappearance of a transition.

In Fig3.6(b) and (c) I show, respectively, the time-resolved differential absorption and absorption traces. In order to have a better visualization of the features, the absorption trace has been obtained as $A-A_{bkg}$, where A is given by $-ln(T_{Ar}/T_0)$, with T_{Ar} and T_0 being, respectively, the transmitted spectra with and without sample. A_{bkg} is a smoothed version of its sharp edge. These traces compare really well with the results from [45]. The $2p_{1/2}4s$ (244.2 eV), $2p_{1/2}5s/3d$ (247 eV) and $2p_{3/2}5s/3d$ (249.2 eV) absorption lines exhibit a Stark-shift. Both $5s/3d$ states shift towards higher energies approaching the ionization limit (≈2 eV) and, at the same time, the absorption lines broaden. These two are nearly one IR photon (0.7 eV) resonant with the $4p$ dark state, hence, their behavior could be in part explained as an Autler-Townes splitting, with the lower state of the doublet less pronounced (as expected being the dark state lower in energy), and masked by other features. $4s$, instead, is not resonant with any dark state and has a much less pronounced shift towards lower photon energies.

The broad positive signal between 245 eV and 246 eV corresponds to the appearance of LISs. The spin-orbit splitting and, hence, the high density of resonances does not allow for an exact assignment of their origin. Possibly, they are two photons resonant coupling from the $2p_{1/2}4s$ and $2p_{1/2}5s/3d$ states. Clearly evident over all the photon energies are periodic modulations of the absorption. The Fourier analysis as function of the photon energy in Fig3.7 clearly shows that the frequency of the oscillations is twice the IR pulse one, as expected.

Besides elucidating the interesting physics of the auotoionizing states of Ar, this measurement and in its comparison with the previously published work, demonstrate the capability of our pump-probe setup to extract sub-cycle strong-field induced dynamics in gas-phase systems. The observation of this periodicity on acquisition time as long as 20 hours is a further confirmation of the CEP and long-term stability of the source.

3.4. CONCLUSIONS

The site-specificity of x-rays spectroscopy is a well-known property that made x-rays a fundamental tool for material science. The capability to access such information in a laboratory-based infrastructure unlocked the possibility to perform such investigation with reduced costs and much more experimental flexibility. At the same time, the recent improvements in the generation of attosecond pulses in big facilities enable to reveal ultrafast dynamics with photon energy and flux not reachable with HHG-based sources. As a consequence of these technological advancements, x-rays science is expected to play a major role in the following years in the investigation of ultrafast non-equilibrium dynamics. In particular, the exemplary measurements shown in section 3.3 provide a picture of the detailed information that XAFS spectroscopy with HHG-based sources can capture thanks to the combination of its broadband bandwidth, high stability and attosecond temporal resolution.

4

ULTRAFAST DYNAMICS IN FURAN RESOLVED WITH ATTOXAFS

In this chapter, I will present the core of this work, which is the experimental observations of the non-adiabatic dynamics of a prototypical five-membered heterocyclic molecule, furan, with attosecond XAFS at carbon K-edge. The knowledge acquired in the previous chapters here will be used to provide a detailed picture of the ultrafast relaxation pathways of the system. The first section, 4.1.3, introduces the reader to the fundamental and practical relevance of the photochemistry of cyclic molecules, as well as to the main nuclear and electronic properties of furan. The second section, 4.2, displays the experimental data and a first qualitative interpretation of the dynamics. The third section, 4.3, is dedicated to a detailed analysis of the experimental and simulated data that will finally lead to a complete interpretation of the experimental results. Finally, section 4.4 will summarize the main results of this work.

4.1. INTRODUCTION

The aim of this section is to provide the experimental and theoretical framework for the experimental results that will be presented in the following. I will start by illustrating the main properties of heterocyclic compounds and the importance of investigating of their ultrafast relaxation dynamics. Next, I will focus on the molecule subject of the present study, furan. Here, first I will show its main electronic and nuclear properties and then I will discuss the main theoretical and experimental results in the literature about its photoinduced ultrafast relaxation dynamics.

4.1.1. HETEROCYCLIC COMPOUNDS

Cyclic compounds have always had historically an important role in organic chemistry because of their peculiar properties. The aromatic systems, for example, are closed-loop molecules with very interesting stability properties due to their π electrons delocalized over the whole ring. A molecule is defined as aromatic if it has planar cyclic geometry, it is fully conjugate (p orbitals at every atoms) and, according to Hückel's Rule, it has $4n+2$ π electrons. Benzene (C_6H_6) is the prototypical aromatic ring molecule in which all carbon atoms are sp^2 hybridized, meaning that each has 1 π electron, and therefore it follows Hückel's Rule with $n=1$. When a ring molecule does not have aromatic properties it is said aliphatic. For example, adding two hydrogen atoms to benzene we have the cyclohexadiene molecule (C_6H_8), which is a non-planar ring compound with just four π electrons and whose bond-breaking reactions upon photon excitation have been intensively investigated [72, 236, 237]. In this case, the presence of dissociative pathways can be interpreted as a consequence of the loss of the high stability properties peculiar to the benzene ring.

Non-adiabatic relaxation dynamics of cyclic molecules have been extensively investigated over the last thirty years. Fundamental and extensive theoretical works have been performed by A.L. Sobolewski, W. Domcke and coworkers, highlighting the electronic and nuclear details of these processes on the ultrashort timescales [238–240]. Pioneering experimental results on the femtochemistry of these systems were obtained by the nobel laureate Ahmed H. Zewail and coworkers. In 1999, they were able to follow the nonradiative deactivation of the excited states of pyridine through time-resolved femtosecond transient absorption [241]. Few years later, they applied ultrafast electron diffraction to determine the transient structures on the ground and excited states of several aromatic molecules [242]. In more recent years, the study of these systems kept being of major interest for the scientific community, as the number of high-level publications on the topic

demonstrates [72, 74, 77, 115, 219, 237, 243]

Among the many kinds of cyclic molecules, five-membered heterocyclic compounds, i.e. closed-loop systems with five atoms on the ring of which at least one is different from carbon (see Fig. 4.1), are of particular interest because of the broad range of fields in which they find applications. For example, they constitute the building blocks in polymers investigated for organic solar cells [244], their derivates have an important role in biochemical processes [245] and applications as pharmacological agents [246] and fuels [247]. Further reasons of interest in this class of molecules are their photoinduced relaxation pathways that typically involve dissociative dynamics [239]. When the bond-breaking happens on the ring, it is identified as Ring-Opening (RO). This relaxation process is characterized by a strong geometrical deformation that leads to the dissociation of the carbon-heteroatom bond and is known to be a dominant pathway in thiophene, furan, selenophene and their derivates [91]. These dynamics are of great fundamental interest and are investigated for technological application, e.g. photo-switching devices [248]. Different, instead, is the case of pyrrole where the excited state deactivation happens through the dissociation of the N-H bond out of the ring.

A competitive non-dissociative channel is the Ring-Puckering (RP) one, which is defined by an out-of-plane rotation of the carbon-heteroatom bonds. Crucial for the existence of trajectories that follow the RP relaxation pathways is the presence of a double bond in the ring (typically between two carbons) where an "ethylenic" dynamic can be initiated [249]. Photo-isomerization of ethylene (C_2H_4) is one of the most investigated photo-induced processes because prototypical for unsaturated hydrocarbons [89]. The molecule is characterized by a double bond between the two carbon atoms and a planar geometry at the ground state; when an electron is promoted from the bonding π molecular orbital to the anti-bonding π^* one, the stable configuration is reached through a twist of the C-C bond. At the same time,

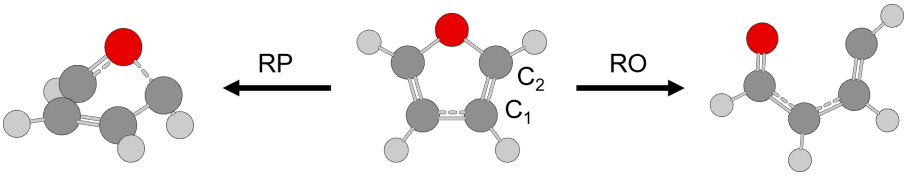

Figure 4.1: Nuclear structure of a prototypical heterocyclic molecule, furan (C_4H_4O). In the center the equilibrium geometry. On the left (right) its distorted ring-puckering (ring-opening) geometry.

the nuclear distortion makes accessible a lower energy electronic state which favors a tetrahedral geometry over the trigonal planar one, i.e. induce a pyramidalization of the molecule. The result is that twisting and pyramidalization happen almost simultaneously leading to a twisted-pyramidalized (tw-py) geometry. In an unsaturated heterocyclic molecule, the structural constraints translate this process into an out-of-plane ring-puckering distortion. O. Schalk and coworkers investigated theoretically and experimentally the dynamics of saturated and unsaturated ring molecules upon $\pi\pi^*$ excitation [249]. They found that, even though the RO is always the main photoproduct in the compounds investigated, in presence of a double bond, the dynamics is delayed. This originates from the accessibility of the RP pathways that leads the molecule to explore other regions of the potential energy surfaces before undergoing ring-opening.

As very often happens in polyatomic molecules, these changes along the nuclear coordinates can strongly modify the energy gap between the potential energy surfaces of the different states till reaching a crossing point, i.e. a conical intersection, that allows an ultrafast internal conversion from an electronically excited state to another or to the ground state. The interplay between electronic and nuclear degrees of freedom plays a fundamental role in the photoinduced reactions of these heterocyclic compounds. Being able to catch the details of the dynamics of such complex systems on such short timescales (typically 10-100 fs) is very challenging, both experimentally and theoretically. The investigation of the ultrafast photochemistry of five-membered heterocyclic molecules is still an environment where the limits of research need to be pushed in order to disentangle electronic and nuclear details of their non-adiabatic deactivation pathways.

4.1.2. DISSOCIATIVE $\pi\sigma^*$ STATE

As mentioned above, many five-membered heterocyclic molecules undergo bond-breaking non-adiabatic relaxation pathways once a $\pi\pi^*$ excitation is induced. The dissociative character of these dynamics comes from the participation in the process of the repulsive $\pi\sigma^*$ state, whose spatially localized character defines which bond breaks. This state is commonly optically dark, i.e. optically inaccessible, in the Frank-Condon region, but, as a consequence of the changes in the nuclear coordinates, its PES intercepts the one of the photoexcited $\pi\pi^*$ state, causing a very effective and ultrafast funneling of energy. This class of relaxation dynamics characterized by the activation of a repulsive state is not typical of only five-membered heterocyclic molecules, but it is a common phenomenon also in biomolecules such as nucleic bases and aromatic amino-acids [90, 250, 251]. The ubiquitousness of the $\pi\sigma^*$ and its crucial role in the dissociative processes drew the interest

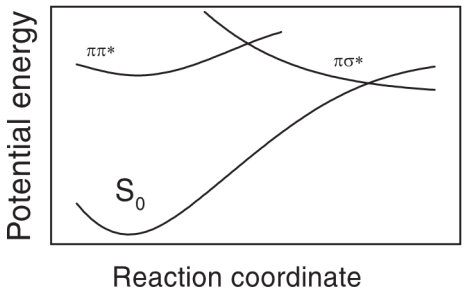

Figure 4.2: Schematic representation of the characteristic case of a repulsive $\pi\sigma^*$ state crossing the $\pi\pi^*$ state and the ground state (S_0). Adapted from [239].

of the scientific community in elucidating its importance.

A.L. Sobolewski, W. Domcke and colleagues investigated theoretically for the first time the repulsive character of this state [83, 239], setting the basis for the comprehension of its role in the ultrafast deactivation dynamics. Its repulsive character translates into a strong force for the elongation, and then the breaking, of the chemical bond on which it is localized. A crucial point in the discussion is that the $\pi\sigma^*$ transition is typically forbidden in the Frank-Condon region for symmetry reasons, while the $\pi\pi^*$ one is highly probable. Quoting the above-mentioned authors, "*The fact that the $\pi\sigma^*$ state is both forbidden and dissociative, renders the spectroscopic detection of the state extremely difficult, if not impossible.* [...] *its existence can only be inferred indirectly via the interpretation of the relaxation or fragmentation dynamics of the photoexcited systems.*". Figure 4.2, adapted from reference [239], shows a schematic view of the intersecting PESs of the $\pi\sigma^*$, $\pi\pi^*$ and GS. Important for the determination of the dynamics is the energetic position of the $\pi\pi^*/\pi\sigma^*$ CI with respect to the minimum of the $\pi\pi^*$ PES. When the former is lower in energy, there is a fast IC from the optically excited state to the dark one. When, instead, the minimum of the $\pi\pi^*$ is below the $\pi\pi^*/\pi\sigma^*$ CI, the dynamics depend on the available energy of the electron wavepacket in the optically excited state. If it is excited close to the bottom of the $\pi\pi^*$ state, then the vibrationally excited state will be long-lived. Instead, if the excess energy is enough to overcome the energy barrier, the system undergoes fast IC to the repulsive state.

For the further relaxation of the system, one possibility is that the $\pi\sigma^*$ PES becomes degenerate also with the GS along the bond fission coordinate, allowing for complete electronic deactivation of the system, as shown in Fig. 4.2. Once the CI

is reached, it can either repopulate the GS of the parent molecule or dissociates in the GS of the products of the bond cleavage. Another possibility, instead, is that the dissociation happens on the $\pi\sigma^*$ PES, resulting in the formation of electronically excited products.

Even with the incredible improvements in the experimental techniques for the study of ultrafast dynamics over the last 20 years, direct detection of this dissociative and dark state is still missing. Being able to directly observe its dynamics could shed light on the photochemistry of a broad range of biologically relevant compounds.

4.1.3. FURAN

In the following, I will focus the attention on a prototypical heterocyclic molecule, furan, which is the subject of the present experimental investigation. Here, I will provide information gathered from the literature regarding, first, its nuclear and electronic structures, and, then, its non-adiabatic relaxation dynamics. Finally, I will present the main experimental results on this molecule.

NUCLEAR AND ELECTRONIC CONFIGURATION

Furan is a heterocyclic compound with one oxygen and four carbon atoms, each bonded with hydrogen (C_4H_4O) (see Fig. 4.1). At ambient conditions, it is in the liquid phase, but its boiling point is very close to room temperature (304.4 K) and, as a consequence, is very volatile (vapor pressure of roughly 800 mbar). Looking at its structural configuration, I will refer to the two carbon atoms bonded to the oxygen as C_1 and C_1', while C_2 and C_2' are the ones further away from the heteroatom. The stable GS configuration is planar with C_{2v} symmetry since it has 2 vertical mirror planes. It is unsaturated with two double bonds, C_1=C_2 and C_1'=C_2', and each atom in the ring is sp^2 hybridized, with the oxygen having two lone pairs of electrons, one of which contributes to the π system. The C_1-C_2 (C_1'-C_2') bond length is significantly smaller than C_2-C_2', as a manifestation of the double bond nature. The compound is aromatic since it is planar, conjugated and has six π electrons, as benzene.

The highest occupied π-orbitals of furan are π_1, π_2 and π_3, while the lowest unoccupied ones are π_4^* and π_5^*, corresponding to a $(\pi_1)^2(\pi_2)^2(\pi_3)^2$ closed shell ground state π electron configuration. The relevant frontier orbitals are shown in Fig. 4.3, adapted from [252]. Referring to the results from reference [253], the lowest valence transitions are in the range of 6-6.5 eV. The first available excited state, S_1, is the Rydberg $\pi_3 3s$ one and is optically dark (oscillator strength equal

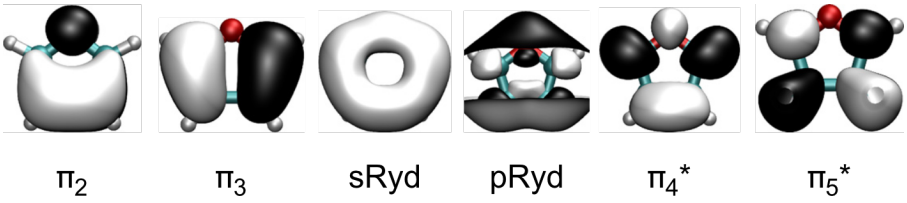

Figure 4.3: Relevant frontier orbitals of furan adapted from [252].

to zero). The one with the largest probability to be excited is the HOMO-LUMO valence transition, S_2, which has $\pi_3\pi_4^*$ nature. This state is very close in energy to the other Rydberg excited state, $\pi_3 3p$, which is the only other transition with a non-zero probability to be excited. The higher $\pi\pi^*$ excited state, S_4, comes from the combination of $\pi_3\pi_5^*$ and $\pi_2\pi_4^*$, it is energetically higher and has a negligible oscillator strength. Another relevant state for the photoinduced dynamics of Furan is the lowest $\pi_3\sigma_{CO}^*$ one. As described in section 4.1.2, this state is dark because the π-σ^* transition is optically forbidden. It is localized on the OC_1 (OC_1') bond and is a repulsive state very high in energy in the FC region (LUMO+80) with transition energy estimated to be close to 20 eV [254].

The VUV absorption spectrum of furan (see Fig. 4.4 adapted from reference [255]) is complex and does not have resolved structures, not allowing for clear assignments. Even if the lower excited states are well identified and their excitation energies have been retrieved with good accuracy, a full description of the shape of the furan absorption spectrum in the low energy region (5.5 eV - 6.5 eV) is not straightforward. As investigated in great detail by E. V. Gromov and coworkers [256, 257], its diffuse nature is a consequence of the strong coupling between the different states, whose presence is also suggested by their energetic proxim-

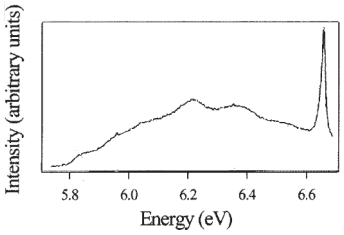

Figure 4.4: Absorption spectrum of furan in the 5.5-7 eV range from [255].

ity. In the following, I will present their interpretation of the spectrum based on the calculation performed under linear vibronic coupling approximation in order to treat multiple electronic states and vibrational degrees of freedom at the same time. Starting from the low energy region (5.6-5.8 eV), historically this has been assigned to S_4 [255]. This is in contradiction with its negligible oscillator strength and its vertical transition energy that, according to calculations, is larger than the S_2 and S_3 ones. According to E.V. Gromov and coworkers, this region could be assigned to the π_3-3s transition, even if not dipole-allowed. The reason is that its vibronic coupling with other excited states can make its contribution visible in the absorption spectrum. The S_2 state, instead, mainly contributes in the region between 5.8 eV and 6.4 eV. Also at these energies the system is subject to very strong non-adiabatic effects that couple multiple states in different regions of the potential energy surfaces, therefore the π-π^* transition is not the only responsible for the shape of the spectrum. Finally, the strong peak at 6.5 eV is assigned to the $\pi_3 3p$ Rydberg state.

PHOTOINDUCED RELAXATION DYNAMICS

One of the reasons why furan is a prototypical compound in the class of the five-membered heterocyclic molecules is that its dynamics upon $\pi \rightarrow \pi^*$ photoexcitation involve the archetypal ring-opening and ring-puckering relaxation pathways. Given its importance, a substantial number of works, both experimentally and theoretically, investigated the problem. In the following I will present their most relevant results, with the aim of pointing out the parts of the dynamics that have been clearly resolved and the ones that still represent open questions. In Fig. 4.5, I show the PESs along the RO and RP pathways along the CO bond length nuclear coordinate calculated by the theory collaborators. These were obtained by linear interpolation between the optimised nuclear GS of furan and the optimized ring-opening conical intersection (ROCI) and ring-puckering conical interaction (RPCI), respectively. The structures were obtained from reference [253] and the linear interpolation was done in internal redundant coordinates using [258]. The electronic ground and excited states calculations were performed with the Gaussian 16 program using (time-dependent) density functional theory (TD-DFT), the hybrid functional PBE0 [259, 260] and the valence triple-zeta basis set with diffuse and polarisation functions, 6-311++G(d,p) [261, 262]. The obtained PES is in very good agreement with the PES in [253] using CCSD/6-311+G*+sp and MS-CASPT2(8,7)/6-311G* level of theory.

Starting from the ring-puckering, the out-of-plane distortion of the ring and the increase of the CO bond length lower the energy of the $\pi_3\pi_4^*$ state, S_2 at the equilibrium, while the $\pi_3 3s$ (S_1) loses its stability. The consequence is an avoided crossing in the early times of the dynamics between the two surfaces that interchange the

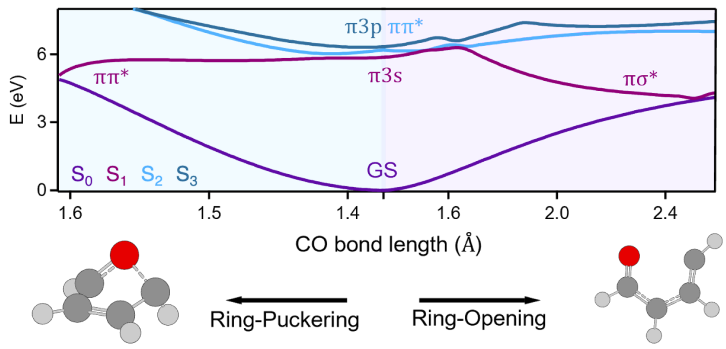

Figure 4.5: Furan PESs as function the CO bond length nuclear coordinated for the RP and RO relaxation pathways involving the relevant electronic states. First three excited states (S_1, S_2, S_3) are represented in magenta, light blue and dark blue, respectively. Shown their electronic configuration at the equilibrium position (center), at the ROCI (right) and RPCI (left) nuclear structures. These were obtained by linear interpolation between the optimised nuclear GS of furan and the optimized ring-opening conical intersection (ROCI) and ring-puckering conical interaction (RPCI), respectively. The structures were obtained from reference [253] and the linear interpolation was done in internal redundant coordinates using [258]. More details in the text.

electronic configurations of PESs, i.e. S_1 becomes $\pi_3\pi_4^*$ and S_2 assumes Rydberg character. Further along the CO elongation coordinate, the $\pi_3\pi_4^*$ keeps relaxing, proceeding without any barriers till reaching the S_0/S_1 seam. In order to be the crossing symmetry allowed, the geometrical structure of the ring is strongly distorted: one CO bond is lengthened by 0.227 Å, while the other is slightly shortened with respect to the equilibrium geometry; at the same time, the same bonds undergo an out-of-plane rotation of 36.4 degrees, while the hydrogen atoms move out of the plane in the opposite direction. The electronic configuration is kept the same, $\pi_3\pi_4^*$, till the conical intersection with the ground state, but its energy is lowered by 1.19 eV with respect to the FC region.

The ring-opening pathway is more complex. The first part of the dynamics is similar to the RP case, with the S_2 surface that initially preserves almost constant energy along the CO elongation coordinate, while S_1 increases in energy reaching the S_1/S_2 crossing where the two states interchange their electronic character. In the meanwhile, $\pi_3\sigma_{CO}^*$ undergoes strong stabilization that allows first an avoided crossing with the $\pi_3 3s$ and then an actual symmetry allowed crossing with $\pi_3\pi_4^*$, $CI_{\pi\pi^*/\pi\sigma^*}$, where it is populated. Further increase in the CO bong length takes the

system to the S_0/S_1 ROCI. At the RO seam point, the geometrical structure of the molecule is mostly planar, with one of the CO bonds stretched (bond length increased by 1.224 Å), while the other is slightly shortened. It is worth noting that most of the CO bond stretching happens after $CI_{\pi\pi^*/\pi\sigma^*}$. The S_0/S_1 crossing happens at an energy of 4 eV, i.e. roughly 2 eV lower than the $\pi_3 \rightarrow \pi_4^*$ transition at the FC region, and occurs long before the $\pi_3\sigma_{CO}^*$ minimum is reached.
The stabilization of the $\pi_3\sigma_{CO}^*$ along the dynamics is a crucial point and has been computationally investigated in detail [252, 254, 263]. Along the RO pathways, the σ_{CO}^* orbital loses its symmetric shape around the oxygen atom and then, when the bond breaking occurs, the σ and σ^* orbitals decompose into two $2p$ ones [249]. The point of change of electronic configuration, from $\pi_3\pi_4^*$ to $\pi_3\sigma_{CO}^*$, is found to be very close in energy to the $\pi_3 \rightarrow \pi_4^*$ transition, allowing for a barrierless deactivation pathway.

The most relevant time-resolved experimental studies on Furan have been performed using photoelectron spectroscopy. The very first investigation of its ultrafast relaxation dynamics was published in 2010 [264]. In this work, thanks to a very high temporal resolution (22 fs), Fuji T. et al. shed light on the early time dynamics after the photoinduced $\pi_3 \rightarrow \pi_4^*$ excitation that involves the participation of the $\pi_3 3s$ state and the S_2/S_1 passage in the first 10-20 fs. However, the low probe energy did not allow to explore the dynamics till the relaxation in the GS. The following investigations tried to solve this issue by probing the dynamics either with multi-photon transitions [265, 266] or higher photon energy [219, 267], usually at the expense of the temporal resolution. Still, the details of the dynamics are yet not well defined, starting from which relaxation pathways is the most probable one. In 2017 Oesterling et al. [266] followed furan's relaxation dynamics with 2 photons probe at the wavelength of 267 nm and with a temporal resolution of 150 fs. Their results confirmed the very short lifetime of the Rydberg state and suggested, with the support of simulations, that most of the trajectories undergo a RO structural deformation in 110 fs. Adalchi et al.[219], instead, used a single-photon 14 eV probe pulse and experimentally found that the relaxation of the system takes place through RPCI at 90 fs (55 fs from the simulations), with the ground state bleach recovery happening at around 200 fs.

One of the reasons for these ambiguous interpretations of the experimental results could be related to the observable. One of the drawbacks of applying photoelectron spectroscopy is that the indetermination principle implies that high temporal sensitivity requires sacrificing the energy resolution or vice versa. Moreover, it is known that the signal obtained through photoelectron spectroscopy could hide details of the dynamics, especially when involving multiple excited states and

several relaxation pathways, as in the present case [268, 269]. In a recent theory work, Filatov M. et al. [116] investigated in detail the furan dynamics and concluded that it is not possible to retrieve the timescales of the passage to the ground state from the photoelectron spectrum and suggested core-level spectroscopy as a complementary measurement to disentangle its details.

4.2. EXPERIMENTAL DATA

In this section I will present the data that consist of the core of this thesis, i.e. static and time-resolved data on furan. Here, I will provide also a first qualitative description of the data before actually moving to the theory comparison in the following section. Finally, I will show the application of a global fit used to highlight time-resolved features hidden in the data.

4.2.1. STATIC AND TIME-RESOLVED MEASUREMENT

I will present in this section the data acquired in our lab using as sample vapors of furan. The experimental setup, for both the static and the time-resolved measurements, is described in chapter 2. The pressure of furan in the interaction region is estimated at around 5 mbar, corresponding to 14 mbar of backing pressure. In the next, I will first show the GS absorption of furan at the carbon K-edge, highlighting its main features, and then the time-resolved data acquired in our experimental campaign.

In Fig. 4.6(a) I show the SXR transmission spectra with and without the furan vapors. The measurement was performed by acquiring 10 consecutive transmission spectra with 90 s exposure time each, alternating acquisition with and without the furan vapors in order to compensate for the potential shift of the spectrum. The spectra clearly display a strong decrease in the transmission in correspondence to the C K-edge (284.5 eV). Around the edge, the furan transmission spectrum presents features that characterize the excitation of the carbon core-electron to the unoccupied orbitals (see inset). In order to enhance these, in Fig. 4.6(b) I show the absorption spectrum, obtained as $-ln(T/T_0)$, where T and T_0 are the averaged transmission spectra, respectively, with and without the sample. The measurement compares really well with previous results from literature [270, 271]. The absorption is characterized by two main peaks at 285.6 eV and 286.5 eV of similar amplitude, followed by the other two at 288.5 eV and 289.3 eV. Given the similar energy distance between these two couple of features, these were historically assigned to excitation of $1s_{C_1}$ and $1s_{C_2}$ electrons to, first, the LUMO and, then, the LUMO+1[270]. At higher energies, the transitions are more difficult to distinguish

since coupled with the rising contribution of the core electrons ionization, which is estimated at 290.4 for C_1 and 291.6 eV for C_2 [270].

The time-resolved data were acquired using the pump-probe setup described in section 2.2.3. For the furan campaign, the beamsplitter used to split the 1.85 μm beam in the pump and probe pulses had a 70/30 ratio, with the most intense portion being exploited for the generation of the SXR attosecond pulse. This allowed obtaining in the pump arm 63 μJ after the beam splitter and 43 μJ in the interaction region. Given a measured focus size of 41 μm and a retrieved pulse duration of 17 fs, the estimated intensity at the focal plane is 9.6 $\times 10^{13}$ W/cm^2.

The data acquisition and analysis protocol has been described in 2.2.3. In this measurement the exposure time per frame was fixed at 15 seconds and, for each delay step, 55 frames were acquired for the pump+probe (I_{pp}) and probe only (I_0) cases and 10 for the pump only (I_p) case. The region exploited for the normalization of the spectra consists of two areas, one before the carbon K-edge (260-280 eV) and one after (300-320 eV), both being far enough from the edge such that no pump-induced effects are present. The data acquired cover the temporal region from -45 fs to 380 fs. The pump-probe delay step size changes over the whole mea-

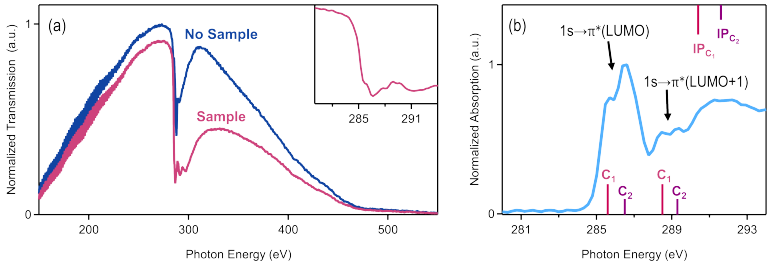

Figure 4.6: (a): Normalized SXR transmission spectra with (magenta) and without (blue) the Furan vapors at 14 mbar of backing pressure. Each spectrum is an average of 10 frames acquired with 90 s exposure time. In the inset the zoom over the C K-edge region. (b): absorption spectrum obtained from the transmission shown in (a); marked the energy positions of the resonance with the $1s_{C_1}$ (magenta) and $1s_{C_2}$ (violet) (see Fig. 4.1) with the bound states (bottom) and the continuum (top).

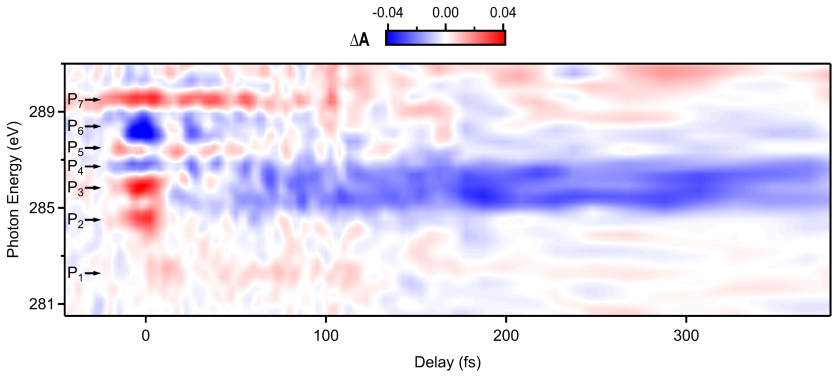

Figure 4.7: Differential Absorption signal as function of pump-probe delay and photon energy of furan pumped with 9.6×10^{13} W/cm^2 and probed at the C K-edge. Notable features are labeled as P_1 through P_7 and discussed in the text.

surement in order to have a better resolution in the first part and larger temporal coverage at the end. The step size used is 2.5 fs between -45 fs and 115 fs, 5 fs between 115 fs and 180 fs and then 20 fs up to the end of the measurement.

Figure 4.7 shows the differential absorption signal as function of the photon Energy (E) and the pump-probe delay (τ), ($\Delta A(E,\tau)$), over the complete dataset. Before moving to the comparison with the simulations, here I will provide a first qualitative description of the data with the aim of pointing out the most relevant features. For negative delays the differential absorption is mostly null, i.e. the absorption spectrum is the same as the ground state one of furan; the only non-zero signal appears at 289 eV. This could be explained as a pump-induced perturbation of the polarization generated by the x-ray pulse [42]. Multiple excited state features appear at the pump and probe time overlap region. Notable features are labeled as P_1 through P_7 and discussed subsequently.

P_1 shows an increased absorption at lower energy than the ground state features and could be identified as the transition of the 1s-core electron to a Singly Occupied Molecular Orbital (SOMO), resulting from the pump-induced excitation of a valence electron. P_4 and P_6, being an absorption decrease in the spectral region characterized by the ground state features, could be interpreted as depletion of GS transitions, i.e. the pump pulse excited an electron in the Lowest Unoccupied

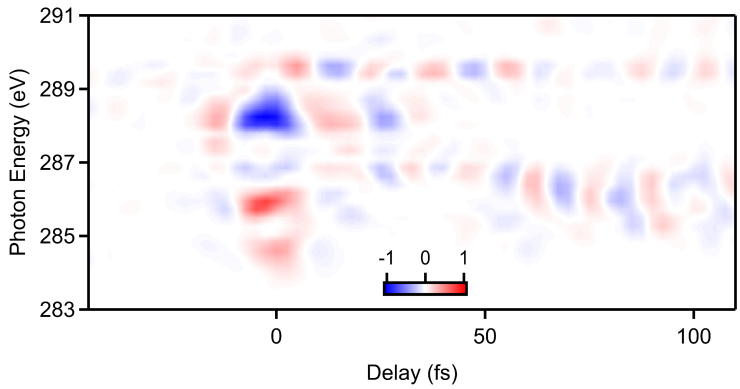

Figure 4.8: Oscillations map obtained as $(\Delta A - Bkg)|Bkg|$ in order to isolate the oscillatory components in the data. Bkg is the polynomial fit of order 7 of the temporal evolution of each energy pixel. More details in the text.

Molecular Orbitals (LUMOs). Finally, P_2, P_3, P_5 and P_7 can be read as an absorption feature's change, in either energy position or amplitude, induced by the pump.

Focusing on the delay-dependent changes, we note distinct temporal evolution. P_2, P_3 and P_6 are very strong in amplitude at the time zero and vanish almost completely around 15 fs (except P_6 which has also a residual component lasting longer). P_4, P_5 and P_7 are periodically modulated in time and last till roughly 100 fs, suggesting that they have a different nature with respect to the much shorter lived P_2, P_3 and P_6. Their modulations in time can be emphasized by removing, from the temporal behavior of each energy pixel, its slow varying component obtained from a polynomial fit (Bkg) and, then, multiplying the resulting trace by the absolute value of the polynomial fit previously subtracted ($(\Delta A - Bkg)|Bkg|$). This last step is used to reduce the contribution of the area dominated by noise. The result is shown in Fig. 4.8. One of the features enhanced is a shift of P_4 towards lower energy between 50 fs and 100 fs, right before the peak completely disappears (it can be appreciated also in the ΔA trace in Fig. 4.7). A sudden energy shift is a typical XAFS feature of a nuclear wavepacket moving along a steep PES gradient in the proximity of a conical intersection [53, 117]. At the same time, a weak positive signal appears at 284.5 eV that lasts till roughly 130 fs (see Fig. 4.7). At delays larger than 150 fs there is a broad and negative long-lasting signal that covers the spec-

tral region of the two main absorption features of the GS. Broad negative signals as this one are usually referred to as ground state bleach, i.e. depletion of the GS. The most relevant part of the dynamics takes place in the first 150 fs, in agreement with previous studies on furan relaxation pathways [219, 266].

Even in such a complex system, a first inspection of the tr-XAFS data gives already a lot of information regarding the underlying dynamics that occur after the excitation from the pump pulse. The depletion of the GS signals at the time overlap suggests that an electron wavepacket has been promoted in an excited state at the pump-probe overlap. The oscillations imply the presence of coherence, electronic and/or vibrational, while the chemical shift and subsequent appearance of the long-lasting bleaching signal indicate that the system has relaxed, most likely through CIs, in the first 150 fs. The long-lasting bleaching signal suggests that the molecule did not go back to the initial conditions, because either it is vibrationally excited or the product of the photoinduced reaction has a different nuclear and/or electronic structure.

4.2.2. GLOBAL FIT

The presence of two distinct carbon atoms, or more once the symmetry is lost due to the photoinduced evolution of the nuclear wavepacket, and multiple transitions from each of them can generate overlapping features that can hide details of the dynamics. The evolution with the pump-probe delay of XAFS peaks can help us disentangle these contributions, as qualitatively shown in the previous section.

In order to do this systematically, we apply a least square fitting model to the time-dependent differential absorption trace, $\Delta A(E,\tau)$, where E is the photon energy and τ is the pump-probe delay. This is constructed with the aim of recognizing the spectral contributions that have similar dynamic trends. We fit the data with the following:

$$\Delta A(E,\tau) = \sum_{i=1}^{3} A_i(E) f_i(\tau)$$

$$f_i(\tau) = \frac{1}{\gamma_i\sqrt{2\pi}} e^{-\frac{1}{2}\left(\frac{\tau-\tau_{0_i}}{\gamma_i}\right)^2} * e^{\frac{\tau-\tau_{0_i}}{\tau_i}}$$

where $A_i(E)$ are the spectral amplitudes and $f_i(\tau)$ are functions comprised of a convolution, in time, of a Gaussian and an exponential decay functions. $f_i(\tau)$ are constructed such to model the rise and the subsequent decay of the respective transient signals. In this way, $A_i(E)$ should show the spectral features with the same temporal evolution $f_i(\tau)$. The number of independent spectral amplitudes

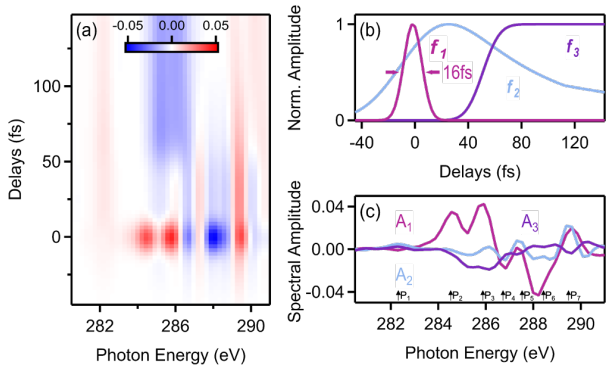

	τ_{0i} (fs)	γ_i (fs)	τ_i (fs)
$i=1$	-1.7	6.7	0.1
$i=2$	-3.2	25.1	69.9
$i=3$	52.2	10	6165697

Figure 4.9: Results of the global fit described in the text. (a): the 2D fit result; (b): time dependence of the f_i; (c): spectral amplitude A_i. For reference shown the relevant peaks position (see Fig. 4.7); in the table the parameters obtained from the fit.

is arbitrary and has been fixed to three because the qualitative analysis of the transient signal suggested the presence of three distinct temporal behavior. The free parameters used are $A_i(E)$, along with the width, γ_i, and the center of the Gaussian function, τ_{0_i}, and the characteristic exponential decay time, τ_i. The fit has been performed on the first 140 fs because of convergence issues on larger datasets. The results are shown in Fig. 4.9.

A_1 is short-lived around the time overlap and its main features are the peaks P_2, P_3 and P_6 described above. The Gaussian width describing the evolution of A_1 is consistent with the temporal duration of the pump pulse and it dominates also its decay, i.e. τ_1 is much smaller than γ_1. In strong-field attosecond transient absorption spectroscopy features like these are usually attributed to reshaping of the absorption lines or light-induced states [43]. A_2 presents an increase in absorption in correspondence of P_1, P_4 and P_7 and negative contributions on the first two features of the GS, i.e. 285.6 eV and 286.5 eV. It peaks around 20 fs and then decays with τ_1=70 fs. Finally, A_3 is characterized by a broad negative signal, again in correspondence of 285.6 eV and 286.5 eV and a small positive signal in correspondence of P_1. Its contribution rises at later times (τ_{0_3}=52 fs) and it does not decay in the time frame of the measurement.

The fit captures the main proprieties of the time-resolved trace and allows to recognize hidden signals, such as the A_2 negative at 285.5 eV that is masked by A_1

at short delays and A_3 at long ones. At the same time, it cannot recognize features like spectral shifts or oscillations, which are indeed present in the data. The fit results can be exploited in order to "clean" the ΔA trace from spectrally overlapping features, like the changes at the time overlap captured by $A_1 f_1$. In Fig. 4.10 I show a subtracted version of the differential absorption, where $A_1 f_1$ and $A_3 f_3$ have been removed. Doing so, we are left with a signal that at time zero is similar to A_2, but at later times has an evolution that cannot be captured by the model. In the following, I will refer to this trace as subtracted ΔA, $sub\Delta A$. Both the $sub\Delta A$ and the ΔA traces will be exploited for the following discussion.

4.3. DATA ANALYSIS AND THEORY COMPARISON

In this section I will show the main results of the data analysis performed on the simulated and experimental data with the aim of building an interpretation of the dynamics observed in the measurement. First, in the section 4.3.1, I will show the calculated XAFS spectra pointing out the key points that will be used further in the analysis of the data. Afterward, I will use these results to assign the principal features of the time-resolved differential absorption spectra. Finally, in section 4.3.3 I will investigate electronic and vibrational coherence in order to provide an interpretation of the modulation present in the data.

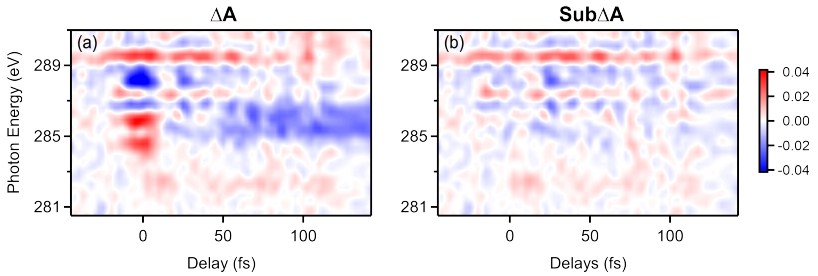

Figure 4.10: Comparison between the ΔA (a) and the $sub\Delta A$ (b) traces. The $sub\Delta A$ has been obtained removing $A_1 f_1$ and $A_3 f_3$ from the ΔA. More details in the text.

4.3.1. XAFS SIMULATION

In order to go further than a qualitative interpretation of the static and time- resolved absorption spectra, a theoretical investigation of the core-level excitation of furan is needed. The x-rays spectra simulated by the theory collaborators were calculated for specific nuclear and electronic configurations using the core-valence-separation scheme [272] in the frozen-core equation of motion model for electronically excited states on the coupled cluster singles and doubles level of theory (fc-CVS-EOM-EE-CCSD) [273]. The spectra were calculated at the relevant nuclear geometry points along the relaxation pathways (FC, $CI^{RO}_{S_1/S_0}$,$CI^{RP}_{S_1/S_0}$) with the respective relevant electronic excited states of the dynamics (GS, $\pi_3 3s$, $\pi_3\pi_4^*$, $\pi_3 3p$, $\pi_3\sigma^*$). In the following, I will first describe in detail the GS simulated spectra, comparing the assignments with previous works, and then I will investigate the changes induced by electronic excitation and/or nuclear deformation.

4

CORE-LEVEL GS ABSORPTION

The absorption spectrum at Carbon and Oxygen K-edges of furan was observed for the first time in 1986 by mean of electron energy loss spectroscopy [270], while the first and only simulations of the core-hole transitions were performed in 2003 [274]. Still, until the present work, the assignments of the XAFS peaks remained elusive; in particular, the controversy was centered around the labeling of a feature at 287.2 eV that was resolved for the first time just in 2002 [271], but no clear assignment was provided. The calculation performed by Duflot D. et al. [274] suggested that this feature was related to the transition to the LUMO+1 π^* orbital, but, at the same time, proposed new assignments of the other resonances that were in strong contrast with the previous literature. In the present work, we unambiguously identify the transitions responsible for the main features of the carbon K-edge spectrum of furan providing also a clear assignment for the 287.2 eV resonance.

In Fig. 4.11, I show the good match between the furan absorption spectrum at the C K-edge measured in our lab and the results of the simulations performed by the theory collaborators. Given its symmetry at the equilibrium geometry, XAFS calculations show that the two distinguishable carbon atoms, C_1 and C_2 (see inset in Fig. 4.11), generate distinct contributions to the spectrum. The first two absorption features primarily correspond to the transitions to the LUMO with π_4^* electronic configuration from, respectively, the $1s$ core orbital of C_1 and C_2, i.e. $1s_{C_1}\rightarrow\pi_4^*$ and $1s_{C_2}\rightarrow\pi_4^*$. A smaller contribution to these peaks is also given by the transition into the higher π^* orbital, i.e. π_5^*. The higher energy peaks of the spectrum have multiple contributions and it is not possible to identify a unique nature.

Still, the ones at 288.5 eV and 289.3 eV are mainly characterized by transitions to the LUMO+1 π orbital, i.e. $1s \rightarrow \pi_5^*$, respectively from C_1 and C_2, mixed with excitation to Rydberg states. The feature at 291.5 eV is largely $1s_{C_1}$ excitation into different σ^* orbitals. Finally, even if not experimentally resolved, the character of the shoulder peak at 287.2 eV is assigned to Rydberg states transitions C_1.

These results are in good agreement with previous interpretations of the spectrum [270, 271] and also allow to identify the presence of resonances to Rydberg states at 287.2 eV, from C_1, and at 288.5 eV, from C_2, solving the controversial assignment of these peaks.

EXCITED STATES AND DISTORTED GEOMETRIES

Changes in the electronic and/or nuclear configuration of a molecule can alter significantly the core-level absorption spectrum [117]. While a modification in the electronic occupation of states can generate an abrupt change in the spectrum, a geometrical rearrangement usually manifests itself as a continuous shift of the features [53]. Thanks to the simulations it is possible to evaluate this on the C K-edge absorption of furan. Firstly, I will discuss electronic transitions in the first excited states and, then, the effects of the nuclear deformations at the ROCI and RPCI.

The spectra comparison between the different electronic configurations at the equilibrium structure is shown in Fig. 4.12. Clear common features of the excited states are the depletion of the two strong resonances at 285.6 eV and 286.5 eV, which in the GS spectrum mainly correspond to the $1s \rightarrow \pi_4^*$ transitions, and the appearance of a new excitation around 282 eV. The latter is assigned to the transi-

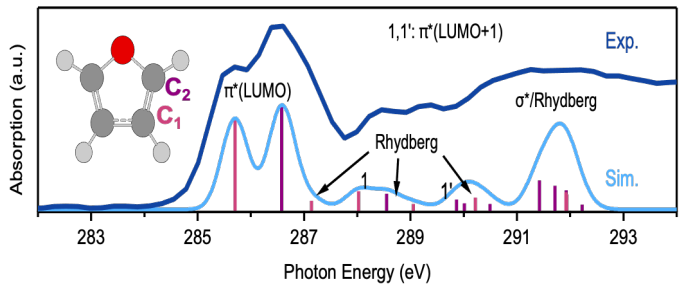

Figure 4.11: Comparison between measured (dark blue) and simulated (light blue) absorption spectrum of furan at the C K-edge at the equilibrium geometry. Most relevant transitions in pink (C_1) and violet (C_2).

tions from C_1 and C_2 into the SOMO, which is the same for the three excited states, i.e. π_3. Interestingly, for this orbital the carbons are not distinguishable. A significant difference between the excited states spectra is the peak at 285 eV present only in the case of Rydberg ones.

Regarding the $\pi_3\pi_4^*$, the depletion of the GS feature is due to the electronic occupation of the π_4^* orbital. The core electron from C_1 is responsible for the transitions in the spectral region between 285 eV and 288 eV. The residual peak at 285.6 eV is $1s_{C_1} \rightarrow \pi_5^*$ (this excitation was present also in the GS spectrum), while the excitation at 287.5 eV has mixed contributions from Rydberg states and, again, the π_5^* orbital. The $1s_{C_2}$ electron, instead, has its main contributions between 288 eV and 290 eV, where the transitions can be primarily assigned to π_5^* and Rydberg orbitals. Moving to the $\pi 3s$ and $\pi 3p$ states, their absorption spectra are very similar and they will be discussed together. In this case, there is not an actual depletion of the $1s \rightarrow \pi_4^*$ transitions, but just a shift and a splitting of these features. The transitions into the Rydberg states are almost completely missing, besides a shoulder peak at 289.5 eV. A mix of π_4^* and π_5^* excitation determines the absorption spectrum above 284 eV. In particular, C_1 transitions entirely define the peak at 285 eV, while C_2 resonances the one at 288.5 eV. The feature at 287.5 eV, instead, is a mix of contributions from both carbons.
Interestingly, in the GS as well as in the excited states, the transitions of the $1s_{C_1}$ electron are always lower in energy than the ones from $1s_{C_2}$

When the molecule loses its C_{2v} symmetry, the complexity of the absorption

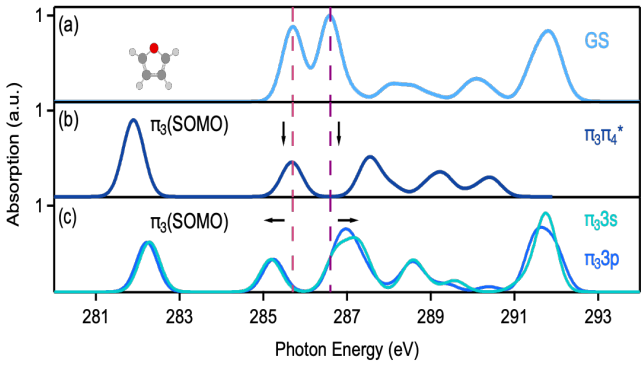

Figure 4.12: Simulated furan XAFS spectra of GS(a), $\pi_3\pi_4^*$(b) and Rydberg states(c) at the equilibrium geometry.

spectra increases since each of the four carbons will have a distinct contribution. This can be appreciated in the simulated spectra at the ROCI and RPCI geometrical structures (see Fig. 4.13). Starting from the RO case, the absorption features can be explained following the flow of population, i.e. $\pi_3\pi^*_{4_{FC}} \rightarrow \pi_3\sigma^*_{ROCI} \rightarrow GS_{ROCI}$. At the $CI_{\pi_3\sigma^*/\pi_3\pi^*_4}$ crossing, the vacancy in the π_3 orbital is preserved and such is also the absorption feature at 282 eV. Interestingly, this time the geometrical distortion of the molecule is such to generate clearly distinct SOMO contributions to the absorption spectrum. Two are at 281.5 eV and 282.5 eV, respectively from C_2 and C_4, while the other two are at 284.5 eV and 285.5 eV, respectively from C_1 and C_3 (see sketch in Fig. 4.13(a) for the carbons labeling). These last two are not purely SOMO transitions but are mixed with transitions into the π^*_4 and π^*_5. In the following passage, CI_{S_1/S_0}, the vacancy in the π_3 orbital is filled. Nevertheless, the GS_{ROCI} spectrum shows a low energy transition, which is assigned to $1s\rightarrow\sigma^*$. It is worth noting that at the ROCI geometry the σ^* orbital is the LUMO. In a qualitative way, this can be understood as the σ^* orbital that stabilized along the ring-opening coordinates, till reaching π_3 energy at the crossing point. The disappearance of the peak at 284.5 eV suggests that is a transient feature along the RO trajectories peculiar to the system being excited in the $\pi_3\sigma^*$ state.

Along the RP trajectories, the peak at 282 eV shifts to 284.5 eV in the passage $\pi_3\pi^*_{4_{FC}} \rightarrow \pi_3\pi^*_{4_{RPCI}}$. After the passage to the GS, a transition at this energy is preserved, similarly to what is seen in the RO dynamics for the peak at 282 eV. This significant difference between the RO and RP trajectories can be qualitatively interpreted by looking at the PESs along the two relaxation pathways (Fig.4.5). In fact, along the RP trajectories the increase in energy of the GS PES is much more

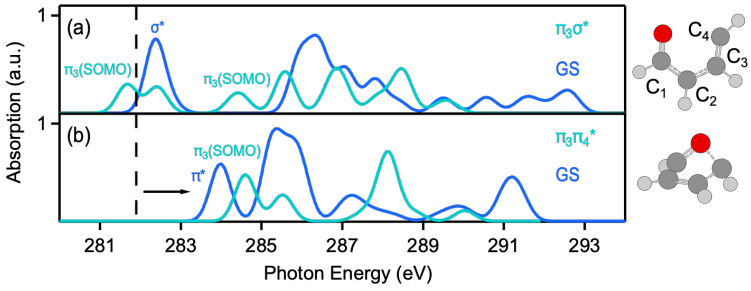

Figure 4.13: Simulated furan XAFS spectra of $\pi_3\sigma^*$ and GS at the ROCI geometry (a) and $\pi_3\pi^*_4$ and GS at the RPCI geometry (b). On the right the sketches representing the corresponding nuclear structures.

pronounced and this could explain the shift of the XAFS SOMO feature to higher energies.

4.3.2. TR-XAFS ASSIGNMENTS

A detailed understanding of the dynamics presented in the data can be obtained by means of comparisons with simulated spectra. In order to do so, another crucial ingredient is to simulate the population dynamics that provide temporal information regarding the flow of electronic energies from one state to another. The theory collaborators provided ab initio on-the-fly surface hopping including non-adiabatic and laser coupling calculations [275, 276]. This method was chosen to sample all possible excited state relaxation pathways without pre-assuming any reaction modes, while incorporating all relevant quantum and strong-field effects. In the next sections, I will first discuss the data at the time overlap, comparing them with simulations at the equilibrium geometry in order to define the excitation induced by the pump; then, the evolution of the ΔA trace will be investigated following the results of the population dynamics. For sake of simplicity, from now on I will refer to the π_3 as π and to the π_4^* as π^*, if not otherwise stated.

OVERLAP REGION

A key point for the interpretation of the data is to identify the optical transition induced by the pump at the overlap between pump and probe. In the present experiment this is not trivial because the pump photon energy is much lower than the first available valence transitions in furan. The high intensity of the pump enables to induce strong-field effects and the timescales of tr-XAFS features suggest that an excited state population was initiated via multi-photon excitation. As previous works show, such a strong-field effect can produce an excitation in the cation[54, 68] and/or in the neutral[66, 71].

In the case of ionization, the ATAS signals are typically characterized by a long-lasting signature of the lowest cationic state that appears at the time overlap, often also showing modulation due to vibrational excitation [54, 65, 68, 277]. The lowest cationic state of furan is known to have an equilibrium geometry similar to the one of the neutral and is not expected to dissociate [278]. In Fig.s 4.14(a) and (b) I compare the simulated ΔA XAFS spectrum of the first electronic state of furan cation at the FC region with the experimental data at the time overlap (-15:15 fs). The positive peaks at 285 eV and 288.5 eV of the cationic spectrum are not present in the experimental data. Moreover, the feature at 289.5 eV, characteristic of both ΔA and $sub\Delta A$ time-averaged spectra (referred to as P_7 in section 4.2.1), is not reproduced in the simulated cationic one.

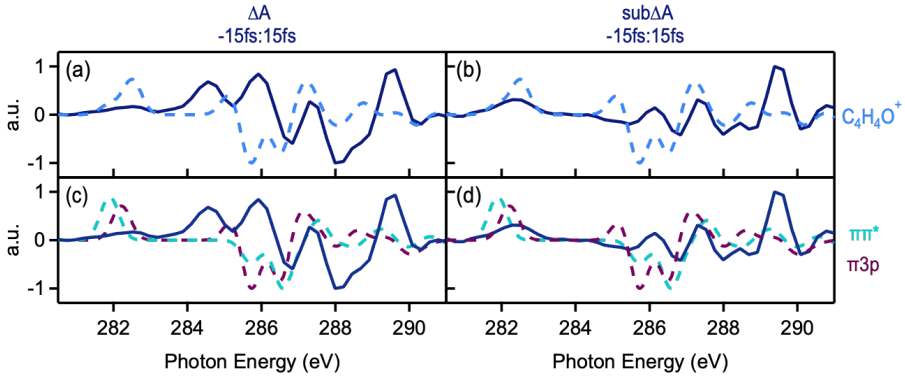

Figure 4.14: Comparison between the simulated differential x-rays absorption spectra and the measured ΔA ((a) and (c)) and $sub\Delta A$ ((b) and (d)) time averaged between -15 fs and 15 fs. In (a) and (b) these are compared with the cation ($C_4H_4O^+$) (light blue), in (c) and (d) with $\pi\pi^*$ (aqua green) and $\pi 3p$ (magenta).

	Transition	ΔE(eV)	f
S_1	$\pi \rightarrow 3s$	5.87	0.00
S_2	$\pi \rightarrow \pi^*$	6.2	0.17
S_3	$\pi \rightarrow 3p$	6.37	0.03

Table 4.1: Calculated electronic transitions, vertical excitation energies (ΔE) and oscillator strengths (f) of the first three excited states of furan at the FC region.

In the case of excitation in the neutral, the calculated energy levels and corresponding oscillator strengths of the first excited states, shown in table 4.1, help identifying the $\pi\rightarrow\pi^*$ and the $\pi\rightarrow 3p$, respectively corresponding to the S_2 and S_3 state, as the two most relevant transitions at the FC region, with a clear preference for S_2. Figure 4.14(c) and (d) show the comparison of the XAFS spectrum of these two states with the time-averaged experimental data. The ΔA at the pump-probe overlap is dominated by the strong peaks at 284.5 eV, 286 eV and 288.5 eV, (previously referred to as P_2, P_3 and P_6). These are not present in the spectra of the excited states, therefore supporting the assignment to reshapes of the absorption lines or light-induced states due to the strong-field character of the pump (see section 4.2.2). The comparison with the $sub\Delta A$, instead, shows a good match with the simulated spectrum of S_2 excited state, allowing to determine that the pump induced a $\pi\rightarrow\pi^*$ transition. This demonstrates the validity of the subtraction pro-

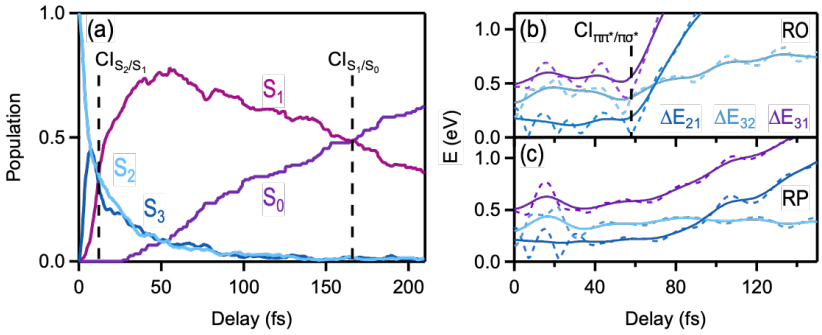

Figure 4.15: Results of the simulated dynamics in furan starting from an excitation into the second excited state (S_2, $\pi\pi^*$ at the FC region). (a): population dynamics of the first three excited states (S_1, S_2, S_3) and GS (S_0); (b),(c): energy gap (ΔE) between the first three excited states as function of pump-probe delay for RO (b) and RP (c) trajectories (dotted lines) and their Gaussian smoothed versions (continuous lines). The Gaussian smoothing used has a width corresponding to the pump pulse one (FWHM = 16 fs). Labeled in (a) and (b) the passage through CI_{S_2/S_1} (12 fs), $CI_{\pi\pi^*/\pi\sigma^*}$ (58 fs) and CI_{S_1/S_0} (158 fs).

cedure applied to the data, which enables highlighting details of the dynamics otherwise masked in the experimental data. The most characteristic features of the $\pi\pi^*$ are the positive peaks at 282 eV (SOMO), 287.5 eV and 289.5 eV and a negative one at 286.5 eV.

The Rydberg ΔA spectrum has as most distinctive features the positive peaks at 285 eV and 288.5 eV (see section 4.3.1). These spectral regions are strongly dominated by the strong-field effects and this could explain why it is not possible to detect electronic excitation in this state.

NON-ADIABATIC RELAXATION TO THE GS

In the previous section I showed how the overlap features can be interpreted as a pump-induced $\pi \rightarrow \pi^*$ transition. Assuming an electronic wavepacket in this excited state, the investigation of the subsequent dynamics provides the necessary tools to interpret the experimental data. The characteristics of the relaxation to the GS were already partially discussed in section 4.1.3. The simulated population dynamics starting from the $\pi\pi^*$ shows a strong interplay between the first three excited states in the early times of the dynamics (see Fig. 4.15(a)). Right after the excitation, there is a very quick exchange between S_2 ($\pi\pi^*$) and S_3 ($\pi 3p$), such that a portion of the population (≈20%) is immediately transferred to S_3. At slightly

later times (12 fs), the S_2 and S_1 PESs cross in a first conical intersection, CI_{S_2/S_1}, with the $\pi\pi^*$ now becoming the lowest excited state S_1. This generates a flow of population from the second to the first excited state with the wavepacket preserving its electronic configuration. This kind of conical intersections is not expected to generate abrupt changes in the XAFS spectrum [53].

In Fig. 4.15(b) and (c) I show the energy gaps (ΔE) between S_1, S_2 and S_3 as function of delay, following, respectively, the RO and RP relaxation pathways. The energy gaps are not strictly constant, but oscillate preserving a more or less stable average value until 60 fs (continuous lines). The fact that ΔE_{21} reaches multiple times the value of zero is a manifestation of the overmentioned strong interplay between the states in this first part of the dynamics. After 60 fs the evolution of the nuclear wavepacket moves the S_1 surface apart from the other two, therefore increasing ΔE_{21} and ΔE_{31}. While on the RP trajectories this happens smoothly, on the RO the change is abrupt. In the latter case, 60 fs turns out to be a very crucial moment of the dynamics, corresponding to the cross between the $\pi\sigma^*$ and the $\pi\pi^*$ PESs. The resulting intersection, $CI_{\pi\pi^*/\pi\sigma^*}$, induces a highly efficient funnel of population, with the $\pi\sigma^*$ becoming the lowest and the most populated state.

In the final part of the relaxation, the nuclear wavepacket proceeds along the S_1 state, $\pi\pi^*$ for RP and $\pi\sigma^*$ for RO, till the ultimate relaxation to the GS at the RPCI and ROCI geometrical structures, CI_{S_1/S_0}, around 160 fs. The present calculations show that the majority of the trajectories (76%) follow the RO relaxation pathways, with the remaining undergoing RP.
Knowing the timestamp of the CIs and the evolution of the PESs as function of time, we can cross reference this to the behavior as function of nuclear coordinates (Fig. 4.5). It is worth noting that the CO bond stretching is much stronger in the last 100 fs after the $CI_{\pi\pi^*/\pi\sigma^*}$ ($\approx 9\times10^{-3}$ Å/fs) than in the first 60 fs ($\approx 5\times10^{-3}$ Å/fs).
Interestingly, simulations suggest that the population dynamics do not change starting from a $\pi 3p$ instead of a $\pi\pi^*$ excitation.

Given the inputs of the theoretical investigations, we can compare these results to the experimental data, exploiting the XAFS simulations presented in section 4.3.1. According to the simulations, in the first 60 fs of the relaxation dynamics, the $\pi\pi^*$ electronic state is expected to be the most populated one. Fitting the temporal evolution of the characteristic XAFS features of this state experimentally confirms this. In Fig. 4.16, I show the peak at 289.5 eV as function of pump-probe delay, superimposed to the fit result obtained using the convolution of a Gaussian and a decay exponential functions. The free parameters used are the width and

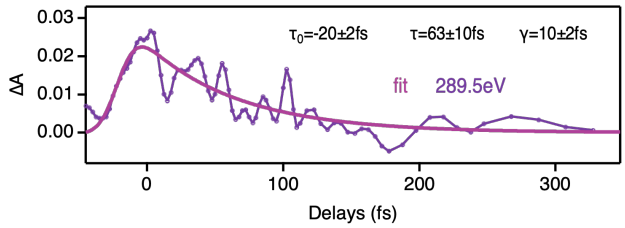

Figure 4.16: Temporal behavior of the energy pixel 289.5 eV and its fitting result. γ and τ_0 are, respectively, the width and the center of the Gaussian function, while τ is the characteristic exponential decay time. Details of the fitting procedure in the text.

the center of the Gaussian function, respectively γ and τ_0, and the characteristic exponential decay time, τ. It reaches its maximum value at zero delay and decays in 63 ±10 fs, in good accordance with the theoretical predictions. Applying the fitting procedure to the other peaks assigned to the $\pi\pi^*$ excited state, such as the one at 287.5, shows similar results.
In this first part of the dynamics, a small portion of the electronic population is expected in the Rydberg states, especially in the first 20 fs after the photoexcitation, because of the strong coupling between the first three excited states. Unfortunately, no feature of the tr-AttoXAFS data can be uniquely assigned to these states. A possible explanation is the presence of strong-field field effects in this temporal region that are spectrally overlapping with the characteristics peaks of the $\pi 3p$ and $\pi 3s$ states, as discussed in section 4.2.2.

After the $CI_{\pi\pi^*/\pi\sigma^*}$ passage, the nuclear wavepacket moves on a steep PES gradient because of the stabilization of the dissociative state along the strong CO bond stretching; its signature in the experimental data is identified with the chemical shift of the oscillating negative feature at 286.5 eV discussed in section 4.2.1 (see Fig. 4.7 and Fig.4.8). At similar delays, a new positive peak appears at 284.4 eV, as it can be appreciated from the time-averaged $sub\Delta A$ spectrum between 70 fs and 110 fs (Fig.4.17(a)). The simulated x-rays spectra of the S_1 state at the ROCI and RPCI nuclear geometries, respectively of $\pi\pi^*$ and $\pi\sigma^*$ electronic configurations, present a positive feature in this spectral region. In both cases, this is constituted by $1s\rightarrow\pi$ and $1s\rightarrow\pi^*$ resonances. As discussed in section 4.3.1, a distinctive feature between these two nuclear geometries is the positive peak at 282.5 eV, only present in the RO one, which corresponds to a SOMO transition. The presence of this peak also in the experimental data allows to provide direct proof of the passage through the $CI_{\pi\pi^*/\pi\sigma^*}$ and of the electronic population in the $\pi\sigma^*$ state, showing

the tr-AttoXAFS' capabilities to directly detect the signature of transiently populated dark states. This experimental observation allows to experimentally identify the RO as the main relaxation pathway, in agreement with the theory.

The low amplitude of the differential absorption signal at 284.4 eV does not allow to experimentally retrieve a decay time for the $\pi\sigma^*$ state. Still, its disappearance around 140 fs (see Fig. 4.9) provides proof of the passage through the CI_{S_1/S_0} and the relaxation in the electronic ground state, since the GS_{ROCI} does not have any resonances in this spectral region (see Fig.4.13). At longer time delays (150 fs:350 fs), ΔA is characterized by a strong depletion of the two main XAFS feature of the ground state, $1s_{C_1}\rightarrow\pi^*$ and $1s_{C_2}\rightarrow\pi^*$, and a positive peak at 282.5 eV (Fig.4.17(b)). The former is a ground state bleaching and its recovery cannot be appreciated in the time frame of the measurement. The 282.5 eV feature is identified in the calculated electronic ground state XAFS spectrum at the RO structure and is assigned to a $1s\rightarrow\sigma^*$ transition (see 4.3.1). The disappearance of the 284.5 eV transition and the presence of a resonance at 282.5 eV at long delays support the identification of the RO as the main relaxation pathway.
The presence of a weak positive signal at 282.5 eV also at delays larger than 200 fs can be interpreted as signature of the complete bond dissociation and can be assigned to a $1s\rightarrow 2p$ transition in radical and/or biradical intermediates. In fact, once the ROCI is reached and the relaxation to the electronic GS occurred, the molecule can either evolve back to the FC geometry or completely break the bond. In the latter case, σ and σ^* orbitals decompose into two $2p$ ones [249] and the system evolves into either radical (carbene) or biradical intermediates [279, 280], de-

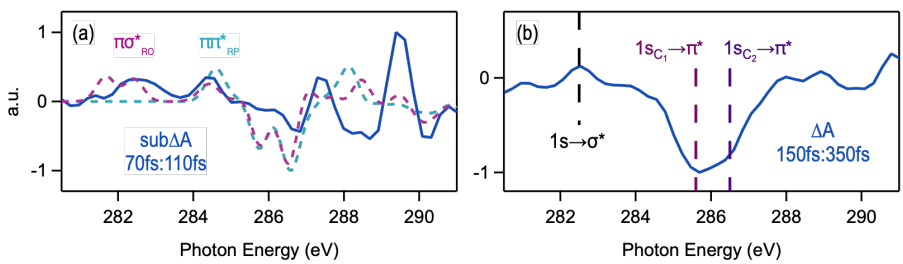

Figure 4.17: (a): $sub\Delta A$ time averaged between 70 fs and 110 fs superimposed to the simulated ΔA spectra of the first excited state at ROCI ($\pi\sigma^*_{RO}$, in magenta) and at RPCI ($\pi\sigma^*_{RP}$, cyan) nuclear structures; (b): ΔA time averaged between 150 fs and 350 fs. labeled the energy position of relevant transitions of the electronic ground state XAFS spectrum at the RO structure (in black) and at the FC region (violet and magenta).

pending on the nature of the bond breaking (homolytic or heterolytic). In a recent tr-XAFS investigation of furfural ring-opening, a low energy peak was identified as the $1s \rightarrow 2p$ transition of radical and/or biradical intermediate products of the photoinduced reaction and was found to last longer than 10ps [74], much more than experimental time window of the present investigation. In general, a peak at an energy close to 282.5 eV is a characteristic feature of carbon K-edge GS absorption spectra of organic radicals [281, 282].

The comparison between the experimental data and the simulated population dynamics and XAFS spectra demonstrates the great capabilities of tr-AttoXAFS at K-edges in disentangling the details of the ultrafast non-adiabatic dynamics of such a complex system. The time-resolved XAFS simulations in the excited states show that the spectra are not subject to large changes between the CIs, allowing an unambiguous assignment based on the relevant nuclear geometry points along the relaxation pathways (GS, $CI^{RO}_{S_1/S_0}$,$CI^{RP}_{S_1/S_0}$) with the respective relevant electronic excited states of the dynamics (S_0, S_1, S_2, S_3).

4.3.3. FOURIER ANALYSIS

While the assignments of the XAFS features give direct information regarding the electronic population of the excited states involved in the relaxation and is crucial for the interpretation of the experimental data, the analysis of the periodic modulations present in the data can provide further details of the coupled electronic and nuclear dynamics. The ΔA trace presents multiple oscillating features, which are further enhanced in the $sub\Delta A$ one (Fig. 4.9). These can be appreciated also in Fig. 4.8. In Fig. 4.18(a) I show the Fourier Transform (FT) of the ΔA as function of energy pixels, done on the temporal region 20 fs:180 fs, to avoid artifacts given by the rise of signals at time zero. Prior to performing the FT, the data are first background subtracted, using a polynomial function, and then smoothed at the border, applying a Hanning function. The results show oscillations in different regions of the spectrum, the strongest being located on the characteristic peaks of the $\pi\pi^*$ spectrum, i.e. 289 eV:290 eV and 286.2 eV:287.5 eV. Focusing on the second one, there are two principal frequency modes (see Fig. 4.18(b) and (c)): a fast one at 63±9 THz (16±2 fs), temporally located in the first part of the dynamics, and a slow one of 36±9 THz (28±7 fs), dominant at later times. The passage from the first to the second one occurs around 75 fs, which is consistent with the decay time of the $\pi\pi^*$ and the passage through $CI_{\pi\pi^*/\pi\sigma^*}$.

According to the interpretation presented in the two following sections, these modes have a different nature, electronic and vibrational, and the passage from

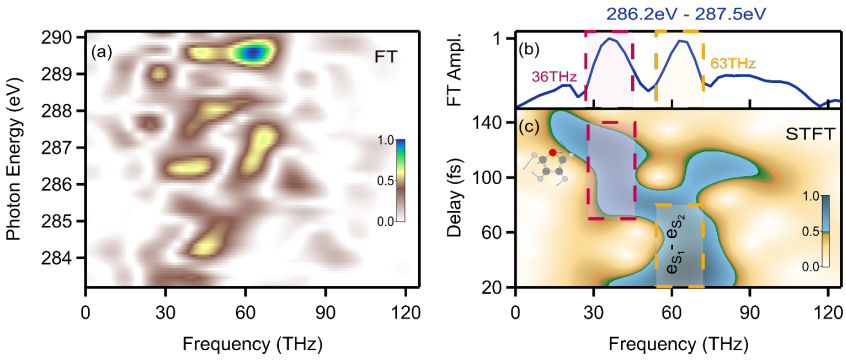

Figure 4.18: Fourier Analysis of the experimental data between 20 fs and 180 fs. Prior to performing the Fourier Transform (FT), data are background subtracted using a polynomial function of order 8 and then a Hanning function is applied to mitigate the border effects. (a): FT as function of the photon energy; (b): FT of the energy averaged signal between 286.2 eV and 287.5 eV; (c) Short Time Fourier Transform (STFT) with 70 fs window of the signal between 286.2 eV and 287.5 eV.

one to the other provides powerful information regarding the role of non-adiabatic coupling in the dynamics. I will discuss separately their origins, starting from the high frequency one.

ELECTRONIC COHERENCE

The high frequency mode is strong on the two spectral regions relevant for the $\pi\pi^*$ XAFS spectrum, 286.2 eV - 287.5 eV and 289 eV - 290 eV (see Fig. 4.18(a)). The former is constituted of a derivative signal that goes from negative to positive values of ΔA, from low to high photon energies, the whole oscillating in phase till roughly 70/80 fs (see Fig. 4.19). The latter is a positive feature of the XAFS and presents intense modulations till 60/70 fs, where the oscillations suffer a drop in amplitude, and then a sort of "revival" around 100 fs. Interestingly, the modulations on these two spectral regions turn out to be out-of-phase with respect to each other (see inset Fig. 4.19(a)). Quantitative estimation of the phase shift is obtained by fitting the temporal evolution of each energy pixel of the $sub\Delta A$ trace as $Acos(\omega\tau + \pi k)$. The free parameters are the amplitude, A, and the phase factor, k, while ω is the dominant frequency retrieved from the Fourier analysis (Fig. 4.19(b)) and τ is the pump-probe delay. In Fig. 4.19(c), I show the phase factor k as function of photon energy for the relevant energy pixels, i.e. the ones for which the fit has a small χ square value and A significantly different from zero. The plot clearly shows a phase

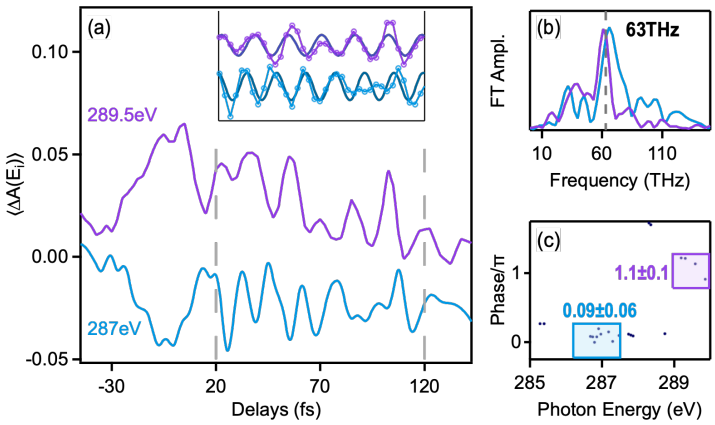

Figure 4.19: Fourier analysis of the fast mode present in the data. (a): Average ΔA signal in the spectral regions 286.2 eV - 287.5 eV (light blue) and 289 eV - 290 eV (violet). In the inset its background subtracted version; (b): FT of the signals in the inset of (a); (c) Retrieved phase factor as function of the photon energy from the fitting procedure (details in the text).

jump between 286.2 eV:287.5 eV ($(0.09 \pm 0.06)\pi$) and 289 eV:290 eV ($(1.1 \pm 0.1)\pi$) consistent with π.

The temporal window in which these 63±9 THz modulations show up is characterized by superposition of electronic states S_2 and S_1, i.e. $\pi 3s$ and $\pi\pi^*$, created by the passage through CI_{S_2/S_1} (see section 4.3.2). Assuming these states are coherently populated after the CI, the resulting electron wavepacket will have two terms, each oscillating with the characteristic energy level of the corresponding state:

$$|\psi(\tau)\rangle = c_1 e^{-iE_1\tau/\hbar}|\psi_1\rangle + c_2 e^{-iE_2\tau/\hbar}|\psi_2\rangle,$$

where τ is the pump-probe delay and $|\psi_1\rangle$ and $|\psi_2\rangle$ are, respectively, the S_1 and S_2 wavefunctions. If these states are coupled back together by a second dynamical event, this will produce coherent-dependent dynamics. The projection of this superposition to a common final state, for example, will beat with a frequency given by the energy difference between the two, $E_2 - E_1 = \Delta E_{21}$. In the current experimental case, this can be obtained by means of the X-rays probe pulse. The intensity of the XAFS signal is given by the modulus square of the transition dipole moment $I_f(\tau)$:

$$I_f(\tau) = |\langle f|\mu|\psi(\tau)\rangle|^2$$

$$= |c_1\mu_{1-f}e^{-iE_1\tau/\hbar} + c_2\mu_{2-f}e^{-iE_2\tau/\hbar}|^2$$
$$= |c_1\mu_{1-f}|^2 + |c_2\mu_{2-f}|^2 + 2|c_1c_2\mu_{1-f}\mu_{2-f}|cos(\Delta E_{21}\tau/\hbar)$$

where $\langle f|$ is the final state and μ_{i-f} is the dipole moment between $|\psi_i\rangle$ and the final state. The coherent-dependent dynamics are contained in the last term, resulting in intensity modulations of the XAFS signal. This is different from zero only if $\mu_{1-f}\mu_{2-f}$ is not null, i.e. the final state is accessible from both S_1 and S_2 by means of the probe pulse. A simplified sketch of this projection scheme is shown in Fig. 4.20(a). The final common state is a doubly excited one, one core and one valence π electron, with the π^* and $3s$ orbitals partially occupied. This can be obtained by projecting either the $\pi\pi^*$ or the $\pi 3s$ to the doubly excited final state. The analysis of the excitation of the XAFS spectrum of these two states shows that transitions to this final state can be identified in both spectral regions of interest, i.e. 289 eV:290 eV and 286.2 eV:287.5 eV (see section 4.3.1).

The calculated ΔE_{21} as function of τ is plotted in Fig. 4.15(b) and (c). Even if it does not have a constant value over time, its average, obtained applying a Gaussian smoothing over the temporal width of the pump, is stable until 60 fs for the RO trajectories and 75 fs for the RP ones. Plotting the beating term $cos(\Delta E_{21}\tau/\hbar)$ shows

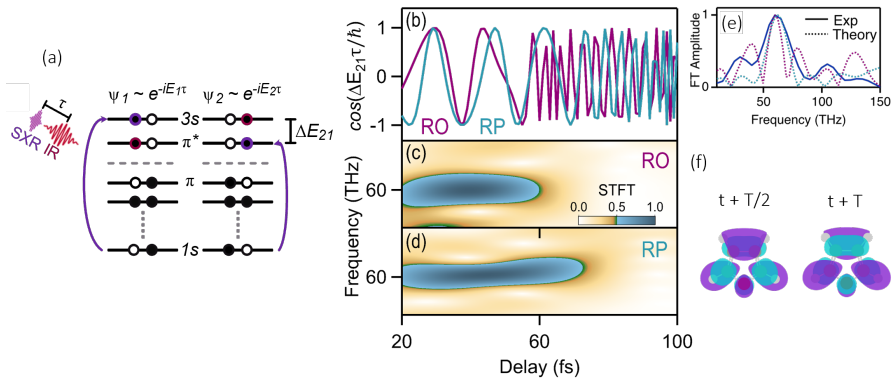

Figure 4.20: Electronic coherence analysis from simulations. (a): Simplified projection scheme of electronic wavefunction to a common doubly excited final state, (b): beating term $cos(\Delta E_{21}\tau/\hbar)$ for RO (light blue) and RP (pink) trajectories, where E_{21} is the averaged one shown in Fig. 4.15(b),(c); (c),(d): STFT of the signals in (b) with 70 fs window; (e): FT of the signals in (b) compared to the experimental one; (f): positive and negative superposition of the $\pi\pi^*$ and $\pi 3s$ wavefunctions showing a π phase difference between the two carbon sites C_1 and C_2.

how this generates regular oscillations in the first part of the dynamics and how then the rapidly increasing energy gap acts as a dephasing effect (see Fig. 4.20(b)). This is reflected also in their Fourier Analysis in Fig. 4.20(c), (d) and (e). They present a main component at the same frequency detected in the experimental data that decays, as expected, around 60 fs for the RO case and a little bit later for the RP one. After this time frame, the rapid frequency change, due to the increase of ΔE_{21}, does not allow to probe the coherence of the superposition of the states. The frequency and the temporal behavior of the 63 THz oscillations in the experimental data match with the theory, providing proof of the presence of a coherent electronic superposition.

By studying the molecular orbitals involved (see Fig. 4.3) is possible to retrieve the symmetry of the coherent superposition of electronic states. Since the vacancy in the π orbital is in common in both S_1 and S_2, the relevant orbitals for the superposition are the π^* and the $3s$. Given the totally symmetric shape of the Rydberg orbital, the resulting electron wavepacket will preserve the π^* symmetry. In particular, it will have a node between C_1 and C_2 that results in a π phase shift between the oscillating electron wavepacket in the two sites (see Fig. 4.20(f)). In a recent theory investigation, Kobayashi et al. showed that the site-specific information of the migrating electron wavepacket initiated by a coherent superposition of electronic states is encoded in the tr-AttoXAFS signal by the complex transition dipole moment[70]. Given the capability of the experimental setup to distinguish the contribution of the different carbon atoms in the furan XAFS spectrum (see section 4.3.1) and the electron wavepacket symmetry, the π phase shift between the periodic modulations of the 289.5 eV and the 287 eV signals is interpreted as a site-specific information of the migrating electron density between C_1 and C_2. This interpretation finds its confirmation in the XAFS spectrum of the $\pi\pi^*$ state (the most populated state in this part of the dynamics), which shows that the low energy region of the spectrum, (285 eV:288 eV), is mainly dominated by transitions starting from the $1s_{C_1}$ electron, while the higher energy region (288 eV:290 eV) from the $1s_{C_2}$ one, as discussed in section 4.3.1

Being able to probe the electronic coherence-induced phenomena gives the opportunity to have the electron perspective on the coupled electron and nuclear dynamics. This provides indirect experimental proof of the passage through CI_{S_2/S_1} and of the presence of electronic population in the $\pi 3s$ dark state. To the best of my knowledge, this is the first time that a migrating electronic density originating from a CI passage has been experimentally probed with site-specific information. This demonstrates the capability of the tr-AttoXAFS to, not only probe electronic coherence, but also to spatially track the oscillating behavior of the electron wavepacket.

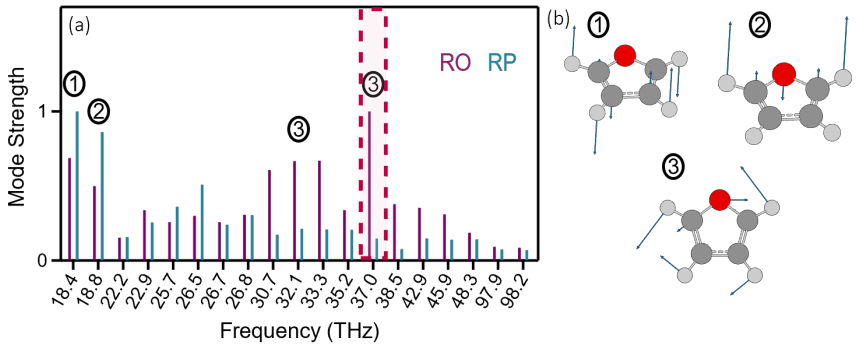

Figure 4.21: (a): Vibrational mode analysis for RO (light violet) and RP (light blue). Highlighted in magenta the mode matching the frequency observed in the data (see Fig. 4.18); (b): sketches of the principal modes resulting from the vibrational analysis.

4

VIBRATIONAL COHERENCE

The low frequency mode is detected in the spectral region 286.5 eV:287.5 eV and it is located in the second part of the dynamics, i.e. from 80 fs to 140 fs (see Fig. (see Fig. 4.18(c))). Similar behavior is observed at 284.5 eV and 288.5 eV. The larger period of these oscillations (27 fs) points towards vibrational coherence as a possible explanation. The vibrational mode analysis is shown in Fig. 4.21, for both RO and RP trajectories. Two modes appear on the low-frequency side with high strengths, especially in the RP case. As shown in the sketches in Fig. 4.21(b), the first one is characterized by out-of-plane motions of the carbon and hydrogen atoms, while the second one is the characteristic ring-puckering mode, defined by out-of-plane and opposite motions of the carbon and oxygen atom. The periods of these modes are large (53 fs and 54 fs period, respectively) with respect to the time scales of the observable and, as such, not easy to detect. In the frequency region from 30 THz to 38 THz, there are several modes dominant in the RO dynamics. The 32.1 THz and the 37 THz ones are ring-opening modes, which are mainly characterized by a stretching of the CO bond length, while the 30.7 THz and the 33.3 THz ones are known as ring-breathing. Among those, the 37 THz mode stands out because it is the one with the largest amplitude and its frequency perfectly matches the experimental observation. The interpretation of the low-frequency oscillation in the data as a ring-opening mode is in line with the theory prediction, confirmed by the data, that most of the trajectories undergo RO. The time localization of this vibrational mode in the final part of the dynamics is interpreted as an indication of the passage through $CI_{\pi\sigma^*/\pi\pi^*}$. As discussed in section 4.1.3 and 4.3.2, after the

CI the evolution of the nuclear wavepacket is characterized by a more pronounced elongation of the CO bond length obtained through the activation of the RO mode. This, in fact, is found to be not dominant in the early time dynamics (0:40 fs) but just in the final part. Moreover, at the same time, the most populated electronic state is the dark $\pi\sigma^*$ that is spatially localized on the CO bond and thus expected to be more sensitive to the vibrational RO mode.

The passage from the 63 THz to the 37 THz modulation is thus interpreted as the nuclear wavepacket evolution along the RO trajectories that at the $CI_{\pi\sigma^*/\pi\pi^*}$, on the one end, acts as a dephasing effect on the electronic wavepacket and, on the other, initiates a stronger deformation of nuclear structure that leads to the dissociation and the relaxation to the GS. This shows the interplay of electronic and nuclear wavepacket in the complex relaxation dynamics and helps assign the RO as the main relaxation pathway.

4.4. CONCLUSIONS

The discussions in the previous chapters highlighted the importance of disentangling the electron and nuclear degrees of freedom with atomic spatial resolution and sub-fs temporal sensitivity in order to resolve the non-adiabatic dynamics of complex systems. Investigating the ultrafast non-adiabatic dynamics of furan (C_4H_4O), a prototypical five-membered molecule, the work presented in the present chapter demonstrated how XAFS spectroscopy with attosecond SXR pulses is capable of meeting these requirements.

In summary, we excited furan via multi-photon absorption of a 17 fs pump beam at a photon energy of 0.7 eV and follow the subsequent relaxation dynamics by measuring the time-dependent carbon K-edge absorption spectra with an isolated attosecond probe pulse. The intricate signal shown by the ΔA trace (Fig. 4.22(a)) contains several characteristic features, which we analyzed by a combination of state-of-the-art simulations and experiments. We extract from this measurement a detailed picture of the coupled electronic and nuclear dynamics that involves multiple CIs, electronic and vibrational coherence and transiently populated dark states. Upon the excitation at time zero, we identify the initial transition to the $\pi\pi^*$ excited state. After the first 15 fs, we observe a fast beating of the XAFS signal at 63±9 THz (16±2 fs) (see Fig. 4.22(b), orange shaded area). Here, the passage through CI_{S_2/S_1} populates a coherent superposition of electronic states and the subsequent quantum beating originates from the electronic wavepacket dynamics as the nuclear wavepacket proceeds on several almost energetically parallel excited electronic states. The migration of the electron wavepacket corre-

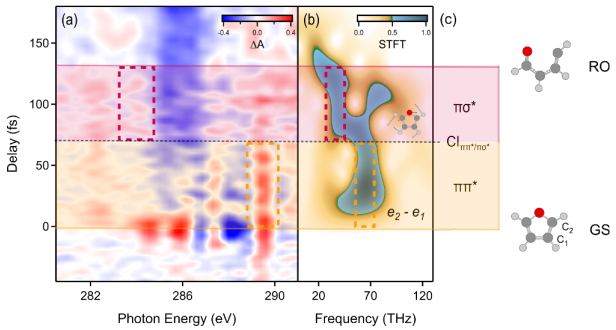

Figure 4.22: Summary of the results of the experimental investigation of furan. (a): Differential absorption (ΔA) as function of the pump-probe delay and the probe photon energy. Marked in orange (magenta) is the relevant XAFS feature of the $\pi\pi^*$ ($\pi\sigma^*$) state; (b): Short Time Fourier Transform (STFT) of the background-subtracted signal at 287 eV; (c): the relevant electronic and nuclear configurations of furan during the relaxation dynamics

4

sponding to two distinct carbon atoms of furan is resolved in the experimental data as out-of-phase quantum beatings in two spectral regions (286.2 eV - 287.5 eV and 288 eV – 289 eV) thanks to the site-specificity of XAFS. The method distinguishes the decay of the $\pi\pi^*$ excited state in 65±10 fs as passage through a second CI, $CI_{\pi\pi^*/\pi\sigma^*}$, that transiently populates a dissociative dark state, the $\pi\sigma^*$ state, which ultimately leads to bond breaking. The signal between 70 fs and 140 fs, besides providing direct access to the electronic population in the $\pi\sigma^*$ state, results in a second Fourier component at 36±9 THz (28±7 fs) that is assigned to activation of the RO vibrational mode (see Fig. 4.22(b), light-red shaded area). The RO dynamics along the $\pi\sigma^*$ state simultaneously results in the dephasing of the electronic coherence. After 140 fs, the $\pi\sigma^*$ XAFS signature disappears and the emergence of a long-lasting component indicate the transition of the excited electronic state back into the electronic GS. Finally, the excitation in the dissociative state, the activation of the vibrational mode and the distinctive signature of the long-lasting signal allow us to identify the RO pathway as the dominant relaxation pathway, in very good agreement with the theory.

The present work tracked for the first time with attosecond temporal resolution a coherently excited polyatomic system with such complexity. This complexity posed great challenges, but, at the same time, offered an ideal opportunity to resolve the interplay between the electronic and nuclear degrees of freedom through multiple CI passages, transiently populated excited states and charge migration.

The fascinating resulting picture of the ultrafast relaxation of the system clearly shows the deep interplay between electrons and nuclei that governs such dynamics, from the sub-fs to the ps time scales.
Despite of a large number of experimental and theoretical works on the subject, the application of AttoXAFS to this system allowed to reveal details never observed before, like the CI-mediated electronic coherence, the spectroscopic signature of the $CI_{\pi\pi^*/\pi\sigma^*}$ passage and the subsequent electronic population in the $\pi\sigma^*$ state. Previous investigations have been mainly performed with PS with either low temporal or energy resolution that limited the experimental observations. The results shown in this chapter demonstrate how the high energy and temporal resolution of AttoXAFS, combined with the site-specific probing of core-level electronic resonances, can overcome these limitations.

The non-equilibrium dynamics of cyclic molecules is complex and can vary from system to system. A broader understanding of the dynamics of such systems requires systematic measurements of their non-adiabatic relaxation under different conditions. Many variables can influence the outcome of the photoinduced reactions, one of which for sure is the character of the chemical bonds on the ring. As highlighted in section 4.1.1, crucial for the existence of an RP pathway and for the efficiency of the RO one is the presence of a double bond on the ring [249]. Systematic AttoXAFS measurements on ring molecules with different saturation levels could provide interesting insights into the details of such dynamics, for example tracing how the time frame of the CI passages, the electronic population and the photoproducts change system to system.

Despite the large number of details retrieved from the data of the present investigation, an improvement of the experimental setup could allow to collect further information. First of all, a pump pulse with 6 eV photon energies would allow for selective excitation and would get rid of the strong-field induced features around time zero that affect the data here presented. This could enable the detection of the electronic population in Rydberg states in the first part of the dynamics. Spectral coverage above 530 eV of the attosecond pulse would allow to simultaneously trace the dynamics from both the carbon and oxygen perspectives, probably providing cleaner signatures and complementary new information. A better spectral resolution and higher SXR photon flux could allow following in a more systematic way the behavior of the XAFS peaks along the dynamics and, hence, the evolution of the wavepacket along the PESs.
We cannot know exactly the amount of details that could be revealed by an ideal AttoXAFS measurement on furan, but these considerations provide motivations for further technological developments in the field of attosecond x-rays science.

5

SUMMARY AND OUTLOOK

5.1. SUMMARY

The work presented in this thesis aims at showing the great capabilities of AttoXAFS in resolving processes taking place on the ultrashort time scales of light-matter interaction. Among the broad range of applications of this spectroscopic technique, the work focuses on the coupled electronic and nuclear dynamics that lead to non-adiabatic relaxation in complex molecules, whose description requires overcoming the Born-Oppenheimer approximation. These dynamics are ubiquitous in polyatomic systems and their experimental investigation is crucial for the comprehension of many biologically and chemically relevant functions.

Tracing the details of these dynamics requires a spectroscopic method capable of observing the evolution of the nuclear and electronic wavepackets on their natural time scales. This became possible with the generation of the first attosecond pulses. Together with the extreme temporal resolution, the birth of attosecond science provided the scientific community with the possibility to exploit table-top x-ray sources for the investigation of matter. The scientific outcome of x-rays attosecond spectroscopy, which is described in section 1.1 of the introduction of this thesis, demonstrated the capabilities of attosecond science to reveal the details of the electrons' motion in matter. Among the many spectroscopic applications of attosecond pulses, attosecond transient absorption, especially when applied to the soft x-rays spectral region, showed to be able to disentangle the interplay between the electronic and nuclear degrees of freedom. Recent theoretical and experimental works show the potentialities of this technique in the investigation

of non-adiabatic processes, such as internal conversion through conical intersections (section 1.2), and purely electronic dynamics, such as charge migration (section 1.3), in complex polyatomic systems. This sets the framework of this thesis that aims at the application of this method to reveal the ultrafast chemical reactions of complex polyatomic systems.

The experimental fundaments of this work are described in chapter 2. The generation of high photon energy ultrashort pulses through the process of HHG is described by the semi-classical three steps model of the interaction of intense laser pulses with gas. Even if this process was understood in 1993, more than twenty years of effort from the scientific community was needed for the first demonstration of isolated attosecond pulses in the soft x-rays spectral region (section 2.1). This result was obtained in Professor's Jens Biegert laboratory at ICFO where the work of this thesis has been performed. In section 2.2 I described the experimental setup for the generation of such pulses and its implementation in the pump-probe scheme for transient absorption spectroscopy, providing the experimental details of the investigations discussed in the following chapters.

Transient absorption in the soft x-rays spectral region allows to perform XAFS K-edge spectroscopy. The well-established capabilities of x-rays science in the study of matter are introduced in chapter 3. In the first section, the main general spectroscopic advantages of high-energy radiation are presented, introducing the reader to the concept of site-specificity. In this section, the different available sources of ultrashort x-ray pulses and their main spectroscopic applications are described. In particular, the capabilities of XAFS spectroscopy are discussed in further detail in section 3.2, being this the method used for the present investigations. Exemplary applications of such technique, performed during my PhD and described in section 3.3, show how its orbital and structural sensitivity, combined with site-specific information, can provide a clear picture of the electronic and structural properties, both in solid state and gas phase samples. Among these, the experimental investigation of the strong-field induced effects in Argon at the $L_{2,3}$-edge demonstrated the capability of the experimental setup to investigate dynamics with sub-fs resolution in gas phase.

In chapter 4, this technique is applied to the investigation of the non-equilibrium dynamics of furan. This is a five-membered heterocyclic molecule (C_4H_4O) whose non-equilibrium dynamic leads to the ultrafast relaxation through either ring- opening (RO) or ring-puckering (RP) structural deformation, typical of cyclic compounds (see section 4.1). The combined experimental and theoretical work shows how the molecule preferentially proceeds through the RO relaxation pathway, pass-

ing through several CIs that mediate the flow of population in multiple electronic states (see section 4.3). The measurement provides signatures of the passage through three CIs: CI_{S_2/S_1} generates a coherent superposition of parallel lying electronic states whose quantum beating is resolved with site-specificity; the decay of the $\pi\pi^*$ state and the appearance of the $\pi\sigma^*$ one, the dephasing of the electronic coherence and the activation of RO vibrational mode, as well as the chemical shift of a spectroscopic feature are clear direct and indirect proofs of the passage through $CI_{\pi\pi^*/\pi\sigma^*}$; the disappearance of excited states features at time longer than 150 fs demonstrates the passage through CI_{S_1/S_0} and the final relaxation of the system in the GS.

The experimental observation of the passage through $CI_{\pi\pi^*/\pi\sigma^*}$ is particularly relevant since it shows the capability of AttoXAFS to provide multiple points of view on the dynamics and to disentangle the nuclear and electronic degrees of freedom. In the time domain, the experimental data show very clearly the electronic passage from the $\pi\pi^*$ to the $\pi\sigma^*$, while the sensitivity to the structural deformation provides a signature of the nuclear rearrangement of the molecule through a chemical shift (see section 4.3.2). At the same time, in the frequency domain electronic and vibrational coherence gives the opportunity to follow the passage from a different perspective (see section 4.3.3). The electronic quantum beating traces the energy spacing between the coherently populated electronic states and its disappearance is a consequence of the effects of the structural deformations that leads to the CI on the PES; the subsequent activation of the RO vibrational mode demonstrates how the populated $\pi\sigma^*$ quickly drives the system towards the structural deformation that leads to the bond-dissociation.

The present work represents a further step in the investigation of the intricate pathways of coupled electronic and nuclear dynamics of a complex polyatomic system with attosecond temporal resolution. The demonstrated great capabilities of AttoXAFS to identify the exact evolution of a complex molecular system across several of its non-adiabatic pathways can play a crucial role in investigating the molecular building blocks of life.

5.2. OUTLOOK

As the reduced number of its experimental applications testify, attosecond x-rays science based on HHG sources, especially when performed in the water window region, is still in its early stages. Further steps are needed in order to finally establish the role of this technique in the spectroscopic community.

One crucial aspect of the development of this spectroscopic technique is the low flux of the sources. State-of-the-art table-top sources in the soft x-rays region have nowadays a flux of 10^5 photons/s over 1% bandwidth. Even if this was a great achievement for the community that allowed to perform the first time-resolved measurements, the corresponding noise level, typically, is at least three orders of magnitude higher compared to experiments performed in the visible and mid-infrared spectral ranges. In addition to generating a comparatively high photon flux from HHG-based sources, a known challenge for working with x-ray beams is the low efficiency of optical elements. A number of exciting technological advancements in source development, as well as x-ray optics, have been recently demonstrated. On one side, the active development of next-generation, ultrafast laser sources for driving the HHG process is underway. 100W-scale OPCPAs have become commercially available in the last few years with expected scaling to the 1kW level [283–285]. On the other side, the developments of reflection zone plate-based x-ray spectrometers offer a dramatic increase in efficiency over current reflection gratings [286]. Thanks to these and further future developments, it is possible to expect an increase of the photon flux up to two or three orders of magnitude in the next decade.

The development of high-power IR sources can play a crucial role also in the extension of time-resolved measurements to higher photon energies. So far the unfavorable scaling law of HHG efficiency with the wavelength precluded the possibility to generate sufficient flux at the Oxygen $K-$edge (see section 2.1.1), but this might be soon unlocked with next-generation IR sources. The recent upgrade of the laser source in our lab allowed us to increase the pulse energy of the CEP-stable IR pulse and, at the same time, shift the central wavelength to 2 μm. Combining this with higher photon flux and spectral resolution deriving from a new spectrograph design will make AttoXAFS an even greater tool for the investigation of ultrafast reactions in organic chemistry.
Exciting prospectives comes also from the recent developments of tunable ultrashort UV sources through soliton compression in hollow-core photonic crystal fiber [287] or hollow-core fiber [288]. Especially in the second case, this unlocked the generation of few-fs μJ-level pulses easily tunable between 160 nm and 350 nm. These characteristics are ideal for a pump pulse capable of selectively photo-excite an organic system and will open the possibility of a broad range of time-resolved experiments.
Another aspect of crucial importance in the investigation of organic chemistry, especially when dealing with transient absorption spectroscopic techniques, is the difficulty in investigating solution phase samples. The high absorption deriving from the high density of the samples prevents the collection of a signal in trans-

mission. This issue has been recently overcome with the development of ultra-thin liquid flat-jets with tunable thickness from few μm to tens of nm [289] and has been recently applied to HHG soft x-rays sources [191]. This enables the application of AttoXAFS to a broad range of biological and chemical-relevant compounds.

BIBLIOGRAPHY

[1] Zewail AH (2000) Femtochemistry: Atomic-Scale Dynamics of the Chemical Bond Using Ultrafast Lasers (Nobel Lecture). *Angew. Chem. Int. Ed* 39:2586–2631.

[2] Scherer NF, Knee JL, Smith DD, Zewail AH (1985) Femtosecond Photofragment Spectroscopy: The Reaction ICN → CN + I. *The Journal of Physical Chemistry* 89:5141–5143.

[3] Dantus M, Rosker MJ, Zewail AH (1987) Real-time femtosecond probing of "transition states" in chemical reactions. *The Journal of Chemical Physics* 87:2395–2397.

[4] Rosker MJ, Dantus M, Zewail AH (1988) Femtosecond real-time probing of reactions. I. The technique. *The Journal of Chemical Physics* 89:6113–6127.

[5] Rose TS, Rosker MJ, Zewail AH (1989) Femtosecond real-time probing of reactions. IV. The reactions of alkali halides. *The Journal of Chemical Physics* 91:7415–7436.

[6] Dantus M, Bowman RM, Zewail AH (1990) Femtosecond laser observations of molecular vibration and rotation. *Nature* 343:737–739.

[7] Corkum PB (1993) Plasma perspective on strong field multiphoton ionization. *Physical Review Letters* 71:1994–1997.

[8] Lewenstein M, Balcou P, Ivanov MY, L'Huillier A, Corkum PB (1994) Theory of high-harmonic generation by low-frequency laser fields. *Physical Review A* 49:2117–2132.

[9] Zuo T, Bandrauk A, Corkum P (1996) Laser-induced electron diffraction: a new tool for probing ultrafast molecular dynamics. *Chemical Physics Letters* 259:313–320.

[10] Wolter B, et al. (2014) Formation of very-low-energy states crossing the ionization threshold of argon atoms in strong mid-infrared fields. 063424:1–8.

[11] Itatani J, et al. (2004) Tomographic imaging of molecular orbitals. *Nature* 432:867–871.

[12] Baker S, et al. (2006) Probing Proton Dynamics in Molecules on an Attosecond Time Scale. *Science* 312:424–427.

[13] Zeidler D, et al. (2005) Controlling attosecond double ionization dynamics via molecular alignment. *Physical Review Letters* 95.

[14] Kraus PM, et al. (2015) Measurement and laser control of attosecond charge migration in ionized iodoacetylene. *Science* 350:790–795.

[15] Wörner HJ, Bertrand JB, Kartashov DV, Corkum PB, Villeneuve DM (2010) Following a chemical reaction using high-harmonic interferometry. *Nature* 466:604–607.

[16] Wörner HJ, et al. (2011) Conical Intersection Dynamics in NO 2 Probed by Homodyne High-Harmonic Spectroscopy. *Science* 334:208–212.

[17] Kraus PM, Wörner HJ (2013) Time-resolved high-harmonic spectroscopy of valence electron dynamics. *Chemical Physics* 414:32–44.

[18] Conti I, Cerullo G, Nenov A, Garavelli M (2020) Ultrafast Spectroscopy of Photoactive Molecular Systems from First Principles: Where We Stand Today and Where We Are Going. *Journal of the American Chemical Society* 142:16117–16139.

[19] Kraus PM, Zürch M, Cushing SK, Neumark DM, Leone SR (2018) The ultrafast X-ray spectroscopic revolution in chemical dynamics. *Nature Reviews Chemistry* 2:82–94.

[20] Krausz F, Ivanov M (2009) Attosecond physics. *Reviews of Modern Physics* 81:163–234.

[21] Leone SR, Neumark DM (2016) Attosecond science in atomic, molecular, and condensed matter physics. *Faraday Discussions* 194:15–39.

[22] Calegari F, Sansone G, Stagira S, Vozzi C, Nisoli M (2016) Advances in attosecond science. *Journal of Physics B: Atomic, Molecular and Optical Physics* 49:62001.

[23] Ramasesha K, Leone SR, Neumark DM (2016) Real-Time Probing of Electron Dynamics Using Attosecond Time-Resolved Spectroscopy. *Annual Review of Physical Chemistry* 67:41–63.

[24] Nisoli M, Decleva P, Calegari F, Palacios A, Martín F (2017) Attosecond Electron Dynamics in Molecules.

[25] Geneaux R, Marroux HJB, Guggenmos A, Neumark DM, Leone SR (2019) Transient absorption spectroscopy using high harmonic generation: a review of ultrafast X-ray dynamics in molecules and solids. *Philosophical Transactions of the Royal Society A: Mathematical, Physical and Engineering Sciences* 377:20170463.

[26] Hentschel M, et al. (2001) Attosecond metrology. *Nature* 414:509–513.

[27] Paul PM, et al. (2001) Observation of a Train of Attosecond Pulses from High Harmonic Generation. *Science* 292:1689–1692.

[28] Drescher M, et al. (2002) Time-resolved atomic inner-shell spectroscopy. *Nature* 419:803–807.

[29] Itatani J, et al. (2002) Attosecond Streak Camera. *Physical Review Letters* 88:173903.

[30] Schultze M, et al. (2010) Delay in Photoemission. *Science* 328:1658–1662.

[31] Klünder K, et al. (2011) Probing Single-Photon Ionization on the Attosecond Time Scale. *Physical Review Letters* 106:143002.

[32] Cavalieri AL, et al. (2007) Attosecond spectroscopy in condensed matter. *Nature* 449:1029–1032.

[33] Neppl S, et al. (2012) Attosecond Time-Resolved Photoemission from Core and Valence States of Magnesium. *Physical Review Letters* 109:087401.

[34] Locher R, et al. (2015) Energy-dependent photoemission delays from noble metal surfaces by attosecond interferometry. *Optica* 2:405.

[35] Uiberacker M, et al. (2007) Attosecond real-time observation of electron tunnelling in atoms. *Nature* 446:627–632.

[36] Calegari F, et al. (2014) Ultrafast electron dynamics in phenylalanine initiated by attosecond pulses. *Science* 346:336–339.

[37] Milne CJ, Penfold TJ, Chergui M (2014) Recent experimental and theoretical developments in time-resolved X-ray spectroscopies. *Coordination Chemistry Reviews* 277-278:44–68.

[38] Chergui M, Collet E (2017) Photoinduced Structural Dynamics of Molecular Systems Mapped by Time-Resolved X-ray Methods. *Chemical Reviews* 117:11025–11065.

[39] Cousin SL, et al. (2014) High-flux table-top soft x-ray source driven by sub-2-cycle, CEP stable, 185-μm 1-kHz pulses for carbon K-edge spectroscopy. *Optics Letters* 39:5383.

[40] Silva F, Teichmann SM, Cousin SL, Hemmer M, Biegert J (2015) Spatiotemporal isolation of attosecond soft X-ray pulses in the water window. *Nature Communications* 6:1–6.

[41] Goulielmakis E, et al. (2010) Real-time observation of valence electron motion. *Nature* 466:739–743.

[42] Beck AR, Neumark DM, Leone SR (2015) Probing ultrafast dynamics with attosecond transient absorption. *Chemical Physics Letters* 624:119–130.

[43] Wu M, Chen S, Camp S, Schafer KJ, Gaarde MB (2016) Theory of strong-field attosecond transient absorption. *Journal of Physics B: Atomic, Molecular and Optical Physics* 49:62003.

[44] Chen S, et al. (2012) Light-induced states in attosecond transient absorption spectra of laser-dressed helium. *Physical Review A* 86:063408.

[45] Chew A, et al. (2018) Attosecond transient absorption spectrum of argon at the L2,3- edge. *Physical Review A* 97:031407.

[46] Wu M, Chen S, Gaarde MB, Schafer KJ (2013) Time-domain perspective on Autler-Townes splitting in attosecond transient absorption of laser-dressed helium atoms. *Physical Review A* 88:043416.

[47] Ott C, et al. (2013) Lorentz Meets Fano in Spectral Line Shapes: A Universal Phase and Its Laser Control. *Science* 340:716–720.

[48] Wang H, et al. (2010) Attosecond Time-Resolved Autoionization of Argon. *Physical Review Letters* 105:143002.

[49] Bernhardt B, et al. (2014) High-spectral-resolution attosecond absorption spectroscopy of autoionization in xenon. *Physical Review A* 89:023408.

[50] Schultze M, et al. (2014) Attosecond band-gap dynamics in silicon. *Science* 346:1348 LP – 1352.

[51] Zürch M, et al. (2017) Direct and simultaneous observation of ultrafast electron and hole dynamics in germanium. *Nature Communications* 8.

[52] Hosler ER, Leone SR (2013) Characterization of vibrational wave packets by core-level high-harmonic transient absorption spectroscopy. *Physical Review A* 88:023420.

[53] Kobayashi Y, Chang KF, Zeng T, Neumark DM, Leone SR (2019) Direct mapping of curve-crossing dynamics in IBr by attosecond transient absorption spectroscopy. *Science* 365:79–83.

[54] Rott F, et al. (2021) Ultrafast strong-field dissociation of vinyl bromide: An attosecond transient absorption spectroscopy and non-adiabatic molecular dynamics study. *Structural Dynamics* 8.

[55] de Groot F (2005) Multiplet effects in X-ray spectroscopy. *Coordination Chemistry Reviews* 249:31–63.

[56] de Groot F, Kotani AA (2008) *Core level spectroscopy of solids* (CRC Press), p 490.

[57] Teichmann SM (2015) Ph.D. thesis (UPC - Universitat Politècnica de Catalunya).

[58] Teichmann SM, Silva F, Cousin SL, Biegert J (2015) Importance of intensity-to-phase coupling for water-window high-order-harmonic generation with few-cycle pulses. *Physical Review A* 91:063817.

[59] Cousin SL, et al. (2017) Attosecond streaking in the water window: A new regime of attosecond pulse characterization. *Physical Review X* 7.

[60] Buades B, et al. (2018) Dispersive soft x-ray absorption fine-structure spectroscopy in graphite with an attosecond pulse. *Optica* 5:502–506.

[61] Buades B, et al. (2018) Attosecond state-resolved carrier motion in quantum materials probed by soft X-ray XANES.

[62] Buades B, et al. (2021) Attosecond state-resolved carrier motion in quantum materials probed by soft x-ray XANES. *Applied Physics Reviews* 8:011408.

[63] Sidiropoulos TPH, et al. (2021) Probing the Energy Conversion Pathways between Light, Carriers, and Lattice in Real Time with Attosecond Core-Level Spectroscopy. *Physical Review X* 11:041060.

[64] Pertot Y, et al. (2017) Time-resolved x-ray absorption spectroscopy with a water window high-harmonic source. *Science* 355:264–267.

[65] Saito N, et al. (2019) Real-time observation of electronic, vibrational, and rotational dynamics in nitric oxide with attosecond soft x-ray pulses at 400eV. *Optica* 6:1542–1546.

[66] Timmers H, et al. (2019) Disentangling conical intersection and coherent molecular dynamics in methyl bromide with attosecond transient absorption spectroscopy. *Nature Communications* 10.

[67] Chang KF, et al. (2020) Revealing electronic state-switching at conical intersections in alkyl iodides by ultrafast XUV transient absorption spectroscopy. *Nature Communications* 11.

[68] Zinchenko KS, et al. (2021) Sub-7-femtosecond conical-intersection dynamics probed at the carbon K-edge. *Science* 371:489–494.

[69] Golubev NV, Kuleff AI (2021) Core-Valence Attosecond Transient Absorption Spectroscopy of Polyatomic Molecules. *Phys. Rev. Lett.* 123001:1–7.

[70] Kobayashi Y, Neumark DM, Leone SR (2022) Theoretical analysis of the role of complex transition dipole phase in XUV transient-absorption probing of charge migration. *Optics Express* 30:5673.

[71] Matselyukh DT, Despré V, Golubev NV, Kuleff AI, Wörner HJ (2022) Decoherence and revival in attosecond charge migration driven by non-adiabatic dynamics. *Nature Physics*.

[72] Attar AR, et al. (2017) Femtosecond x-ray spectroscopy of an electrocyclic ring-opening reaction. *Science* 356:54 LP – 59.

[73] Bhattacherjee A, Pemmaraju CD, Schnorr K, Attar AR, Leone SR (2017) Ultrafast Intersystem Crossing in Acetylacetone via Femtosecond X-ray Transient Absorption at the Carbon K-Edge. *Journal of the American Chemical Society* 139:16576–16583.

[74] Bhattacherjee A, et al. (2018) Photoinduced Heterocyclic Ring Opening of Furfural: Distinct Open-Chain Product Identification by Ultrafast X-ray Transient Absorption Spectroscopy. *Journal of the American Chemical Society* 140:12538–12544.

[75] Yang J, et al. (2018) Imaging CF3I conical intersection and photodissociation dynamics with ultrafast electron diffraction. *Science* 361.

[76] Schnorr K, et al. (2019) Tracing the 267 nm-Induced Radical Formation in Dimethyl Disulfide Using Time-Resolved X-ray Absorption Spectroscopy. *The Journal of Physical Chemistry Letters* 10:1382–1387.

[77] Scutelnic V, et al. (2021) X-ray transient absorption reveals the 1Au ($n\pi^*$) state of pyrazine in electronic relaxation. *Nature Communications* 12.

[78] Kleine C, et al. (2022) Electronic State Population Dynamics upon Ultrafast Strong Field Ionization and Fragmentation of Molecular Nitrogen. *Physical Review Letters* 129:123002.

[79] Domcke W, Yarkony DR, Köppel H (2004) *Conical Intersections: Electronic Structure, Dynamics Spectroscopy* (WORLD SCIENTIFIC) Vol. 15.

[80] Domcke W, Yarkony DR, Köppel H (2011) *Conical Intersections: Theory, Computation and Experiment* (WORLD SCIENTIFIC) Vol. 17.

[81] Callis PR (1983) Electronic States and Luminescence of Nucleic Acid Systems. *Annual Review of Physical Chemistry* 34:329–357.

[82] Creed D (1984) The Photophysics And Photochemistry of the Newar-UV Absorbing Amino Acids Tryptophan and its simple derivatives. *Photochemistry and Photobiology* 39:537–562.

[83] Sobolewski AL, Domcke W, Dedonder-Lardeux C, Jouvet C (2002) Excited-state hydrogen detachment and hydrogen transfer driven by repulsive $1\pi\sigma^*$ states: A new paradigm for nonradiative decay in aromatic biomolecules. *Physical Chemistry Chemical Physics* 4:1093–1100.

[84] Crespo-Hernández CE, Cohen B, Hare PM, Kohler B (2004) Ultrafast excited-state dynamics in nucleic acids. *Chemical Reviews* 104:1977–2019.

[85] Satzger H, et al. (2006) Primary processes underlying the photostability of isolated DNA bases: Adenine. *PNAS* 103:10196–10201.

[86] Schoenlein RW, Peteanu LA, Mathies RA, Shank CV (1991) The First Step in Vision: Femtosecond Isomerization of Rhodopsin. *Science* 254:412–415.

[87] Polli D, et al. (2010) Conical intersection dynamics of the primary photoisomerization event in vision. *Nature* 467:440–443.

[88] Wald G (1968) Molecular Basis of Visual Excitation. *Science* 162:230–239.

[89] Levine BG, Martínez TJ (2007) Isomerization through conical intersections. *Annual Review of Physical Chemistry* 58:613–634.

[90] Ashfold MN, et al. (2010) $\pi\sigma^*$ Excited states in molecular photochemistry. *Physical Chemistry Chemical Physics* 12:1218–1238.

[91] Ashfold MN, et al. (2017) Exploring the Dynamics of the Photoinduced Ring-Opening of Heterocyclic Molecules. *Journal of Physical Chemistry Letters* 8:3440–3451.

[92] Born M, Oppenheimer R (1927) Zur Quantentheorie der Molekeln. *Annalen der Physik* 389:457–484.

[93] Zener C (1932) Non-adiabatic crossing of energy levels. *Proceedings of the Royal Society of London. Series A, Containing Papers of a Mathematical and Physical Character* 137:696–702.

[94] von Neumann J, Wigner EP (1929) Über das Verhalten von Eigenwerten bei adiabatischen Prozessen. *Physik. Z.* 30:467–470.

[95] Teller E (1937) The Crossing of Potential Surfaces. *The Journal of Physical Chemistry* 41:109–116.

[96] Yarkony DR (1996) Diabolical conical intersections. *Reviews of Modern Physics* 68:985–1013.

[97] Domcke W, Yarkony DR (2012) Role of Conical Intersections in Molecular Spectroscopy and Photoinduced Chemical Dynamics. *Annual Review of Physical Chemistry* 63.

[98] Robb MA (2014) pp 189–228.

[99] Michl J (1974) Physical basis of qualitative MO arguments in organic photochemistry. *Topics Curr. Chem.* pp 1–59.

[100] Xantheas S, Elbert ST, Ruedenberg K (1990) An intersection seam between the ground state of ozone and an excited state of like symmetry ^{a)}. *The Journal of Chemical Physics* 93:7519–7521.

[101] Riad Manaa M, Yarkony DR (1990) On the noncrossing rule in polyatomic systems: Determination of a seam of actual surface crossings relevant to the quenching of H2(B 1Σ+u) by helium. *The Journal of Chemical Physics* 93:4473–4474.

[102] Bernardi F, De S, Olivucci M, Robb MA (1990) The mechanism of ground-state-forbidden photochemical pericyclic reactions: evidence for real conical intersections. *Journal of the American Chemical Society* 112:1737–1744.

[103] Kowalewski M, Fingerhut BP, Dorfman KE, Bennett K, Mukamel S (2017) Simulating Coherent Multidimensional Spectroscopy of Nonadiabatic Molecular Processes: From the Infrared to the X-ray Regime. *Chemical Reviews* 117:12165–12226.

[104] Schuurman MS, Stolow A (2018) Dynamics at Conical Intersections. *Annual Review of Physical Chemistry* 69:427–450.

[105] Haiser K, et al. (2012) Mechanism of UV-Induced Formation of Dewar Lesions in DNA. *Angewandte Chemie International Edition* 51:408–411.

[106] Roberts GM, Marroux HJB, Grubb MP, Ashfold MNR, Orr-Ewing AJ (2014) On the Participation of Photoinduced N–H Bond Fission in Aqueous Adenine at 266 and 220 nm: A Combined Ultrafast Transient Electronic and Vibrational Absorption Spectroscopy Study. *The Journal of Physical Chemistry A* 118:11211–11225.

[107] Zhang Y, Improta R, Kohler B (2014) Mode-specific vibrational relaxation of photoexcited guanosine 5-monophosphate and its acid form: a femtosecond broadband mid-IR transient absorption and theoretical study. *Phys. Chem. Chem. Phys.* 16:1487–1499.

[108] Batignani G, et al. (2016) Visualizing Excited-State Dynamics of a Diaryl Thiophene: Femtosecond Stimulated Raman Scattering as a Probe of Conjugated Molecules. *The Journal of Physical Chemistry Letters* 7:2981–2988.

[109] Batignani G, et al. (2021) Excited-State Energy Surfaces in Molecules Revealed by Impulsive Stimulated Raman Excitation Profiles. *The Journal of Physical Chemistry Letters* 12:9239–9247.

[110] Zewail AH (1988) Laser Femtochemistry. *Science* 242:1645–1653.

[111] Borrego-Varillas R, et al. (2018) Observation of the Sub-100 Femtosecond Population of a Dark State in a Thiobase Mediating Intersystem Crossing. *Journal of the American Chemical Society* 140:16087–16093.

[112] Suzuki YI, Fuji T, Horio T, Suzuki T (2010) Time-resolved photoelectron imaging of ultrafast S2→S1 internal conversion through conical intersection in pyrazine. *The Journal of Chemical Physics* 132:174302.

[113] Ullrich S, Schultz T, Zgierski MZ, Stolow A (2004) Electronic relaxation dynamics in DNA and RNA bases studied by time-resolved photoelectron spectroscopy. *Physical Chemistry Chemical Physics* 6:2796.

[114] von Conta A, et al. (2018) Conical-intersection dynamics and ground-state chemistry probed by extreme-ultraviolet time-resolved photoelectron spectroscopy. *Nature Communications* 9:3162.

[115] Pathak S, et al. (2020) Tracking the ultraviolet-induced photochemistry of thiophenone during and after ultrafast ring opening. *Nature Chemistry* 12:795–800.

[116] Filatov M, Lee S, Nakata H, Choi CH (2021) Signatures of conical intersection dynamics in the time-resolved photoelectron spectrum of furan: Theoretical modeling with an ensemble density functional theory method. *International Journal of Molecular Sciences* 22.

[117] Neville SP, Chergui M, Stolow A, Schuurman MS (2018) Ultrafast X-ray spectroscopy of conical intersections. *Phys. Rev Lett.* 120.

[118] Weinkauf R, et al. (1996) Highly Efficient Charge Transfer in Peptide Cations in the Gas Phase: Threshold Effects and Mechanism. *The Journal of Physical Chemistry* 100:18567–18585.

[119] Remacle F, Levine RD (2006) An electronic time scale in chemistry. *Proceedings of the National Academy of Sciences* 103:6793–6798.

[120] Mendive-Tapia D, Vacher M, Bearpark MJ, Robb MA (2013) Coupled electron-nuclear dynamics: Charge migration and charge transfer initiated near a conical intersection. *The Journal of Chemical Physics* 139:044110.

[121] Cederbaum L, Zobeley J (1999) Ultrafast charge migration by electron correlation. *Chemical Physics Letters* 307:205–210.

[122] Lépine F, Ivanov MY, Vrakking MJJ (2014) Attosecond molecular dynamics: fact or fiction? *Nature Photonics* 8:195–204.

[123] Breidbach J, Cederbaum LS (2003) Migration of holes: Formalism, mechanisms, and illustrative applications. *The Journal of Chemical Physics* 118:3983–3996.

[124] Kuleff AI, Cederbaum LS (2014) Ultrafast correlation-driven electron dynamics. *Journal of Physics B: Atomic, Molecular and Optical Physics* 47:124002.

[125] Merritt ICD, Jacquemin D, Vacher M (2021) Attochemistry: Is Controlling Electrons the Future of Photochemistry? *The Journal of Physical Chemistry Letters* 12:8404–8415.

[126] Lindner F, et al. (2005) Attosecond Double-Slit Experiment. *Physical Review Letters* 95:040401.

[127] Kling MF, et al. (2006) Control of Electron Localization in Molecular Dissociation. *Science* 312:246–248.

[128] Kling MF, von den Hoff P, Znakovskaya I, de Vivie-Riedle R (2013) (Sub-)femtosecond control of molecular reactions via tailoring the electric field of light. *Physical Chemistry Chemical Physics* 15:9448.

[129] Arnold C, Vendrell O, Welsch R, Santra R (2018) Control of Nuclear Dynamics through Conical Intersections and Electronic Coherences. *Physical Review Letters* 120:123001.

[130] Schüppel F, Schnappinger T, Bäuml L, de Vivie-Riedle R (2020) Waveform control of molecular dynamics close to a conical intersection. *The Journal of Chemical Physics* 153:224307.

[131] Schnappinger T, de Vivie-Riedle R (2021) Coupled nuclear and electron dynamics in the vicinity of a conical intersection. *The Journal of Chemical Physics* 154:134306.

[132] Hartree DR (1928) The Wave Mechanics of an Atom with a Non-Coulomb Central Field. Part I. Theory and Methods. *Mathematical Proceedings of the Cambridge Philosophical Society* 24:89–110.

[133] Arnold C, Vendrell O, Santra R (2017) Electronic decoherence following photoionization: Full quantum-dynamical treatment of the influence of nuclear motion. *Physical Review A* 95:033425.

[134] Vacher M, Meisner J, Mendive-Tapia D, Bearpark MJ, Robb MA (2015) Electronic Control of Initial Nuclear Dynamics Adjacent to a Conical Intersection. *The Journal of Physical Chemistry A* 119:5165–5172.

[135] Vacher M, Bearpark MJ, Robb MA, Malhado JP (2017) Electron Dynamics upon Ionization of Polyatomic Molecules: Coupling to Quantum Nuclear Motion and Decoherence. *Physical Review Letters* 118:083001.

[136] Scheidegger A, Vaníček J, Golubev NV (2022) Search for long-lasting electronic coherence using on-the-fly ab initio semiclassical dynamics. *The Journal of Chemical Physics* 156:034104.

[137] Keefer D, Schnappinger T, de Vivie-Riedle R, Mukamel S (2020) Visualizing conical intersection passages via vibronic coherence maps generated by stimulated ultrafast X-ray Raman signals. *Proceedings of the National Academy of Sciences* 117:24069–24075.

[138] Bäuml L, Schnappinger T, Kling MF, de Vivie-Riedle R (2021) Photo-Induced Coupled Nuclear and Electron Dynamics in the Nucleobase Uracil. *Frontiers in Physics* 9.

[139] Neville SP, Stolow A, Schuurman MS (2022) Formation of electronic coherences in conical intersection-mediated dynamics. *Journal of Physics B: Atomic, Molecular and Optical Physics* 55:044004.

[140] Kobayashi Y, et al. (2018) Selectivity of Electronic Coherence and Attosecond Ionization Delays in Strong-Field Double Ionization. *Physical Review Letters* 120:233201.

[141] Kobayashi Y, et al. (2020) Coherent electronic-vibrational dynamics in deuterium bromide probed via attosecond transient-absorption spectroscopy. *Physical Review A* 101:063414.

[142] Kobayashi Y, Neumark DM, Leone SR (2020) Attosecond XUV probing of vibronic quantum superpositions in Br2+. *Physical Review A* 102:051102.

[143] Puell H, Spanner K, Falkenstein W, Kaiser W, Vidal CR (1976) Third-harmonic generation of mode-locked Nd:glass laser pulses in phase-matched Rb-Xe mixtures. *Physical Review A* 14:2240–2257.

[144] Reintjes J, Chiao-Yao She, Eckardt R (1978) Generation of coherent radiation in XUV by fifth- and seventh-order frequency conversion in rare gases. *IEEE Journal of Quantum Electronics* 14:581–596.

[145] Li XF, L'Huillier A, Ferray M, Lompré LA, Mainfray G (1989) Multiple-harmonic generation in rare gases at high laser intensity. *Physical Review A* 39:5751–5761.

[146] L'Huillier A, Schafer KJ, Kulander KC (1991) Higher-order harmonic generation in xenon at 1064 nm: The role of phase matching. *Physical Review Letters* 66:2200–2203.

[147] Krause JL, Schafer KJ, Kulander KC (1992) Calculation of photoemission from atoms subject to intense laser fields. *Physical Review A* 45:4998–5010.

[148] Krause JL, Schafer KJ, Kulander KC (1992) High-order harmonic generation from atoms and ions in the high intensity regime. *Physical Review Letters* 68:3535–3538.

[149] Kulander KC, Schafer KJ, Krause JL (1993) *Super Intense Laser Atom Physics (SILAP) III.*

[150] Balcou P, L'Huillier A (1993) Phase-matching effects in strong-field harmonic generation. *Physical Review A* 47:1447–1459.

[151] Miyazaki K, Takada H (1995) High-order harmonic generation in the tunneling regime. *Physical Review A* 52:3007–3021.

[152] Balcou P, Sali'eres P, L'Huillier A, Lewenstein M (1997) Generalized phase-matching conditions for high harmonics: The role of field-gradient forces. *Physical Review A* 55:3204–3210.

[153] Austin DR, Biegert J (2012) Strong-field approximation for the wavelength scaling of high-harmonic generation. *Physical Review A - Atomic, Molecular, and Optical Physics* 86:1–7.

[154] Spielmann C, et al. (1997) Generation of coherent x-rays in the water window using 5-femtosecond laser pulses. *Science* 278:661–664.

[155] Paul A, et al. (2003) Quasi-phase-matched generation of coherent extreme-ultraviolet light. *Nature* 421:51–54.

[156] Seres E, Seres J, Krausz F, Spielmann C (2004) Generation of coherent soft-X-ray radiation extending far beyond the titanium L edge. *Physical Review Letters* 92:2–4.

[157] Seres J, et al. (2010) Laser-driven amplification of soft X-rays by parametric stimulated emission in neutral gases. *Nature Physics* 6:455–461.

[158] Shiner AD, et al. (2009) Wavelength scaling of high harmonic generation efficiency. *Physical Review Letters* 103.

[159] Shan B, Chang Z (2002) Dramatic extension of the high-order harmonic cutoff by using a long-wavelength driving field. *Physical Review A - Atomic, Molecular, and Optical Physics* 65:4.

[160] Teichmann SM, Silva F, Cousin SL, Hemmer M, Biegert J (2016) 0.5-keV Soft X-ray attosecond continua. *Nature Communications* 7.

[161] Li J, et al. (2017) 53-attosecond X-ray pulses reach the carbon K-edge. *Nature Communications* 8:186.

[162] Ishii N, Kaneshima K, Kanai T, Watanabe S, Itatani J (2018) Generation of sub-two-cycle millijoule infrared pulses in an optical parametric chirped-pulse amplifier and their application to soft x-ray absorption spectroscopy with high-flux high harmonics. *Journal of Optics (United Kingdom)* 20.

[163] Johnson AS, et al. (2018) High-flux soft x-ray harmonic generation from ionization-shaped few-cycle laser pulses. *Science Advances* 4.

[164] Schmidt C, et al. (2018) High-order harmonic source spanning up to the oxygen K-edge based on filamentation pulse compression. *Opt. Express* 26:11834–11842.

[165] Pupeikis J, et al. (2020) Water window soft x-ray source enabled by a 25 W few-cycle 22 μm OPCPA at 100 kHz. *Optica* 7:168.

[166] Farkas G, Tóth C (1992) Proposal for attosecond light pulse generation using laser induced multiple-harmonic conversion processes in rare gases. *Physics Letters A* 168:447–450.

[167] Baltuška A, et al. (2003) Attosecond control of electronic processes by intense light fields. *Nature* 421:611–615.

[168] Holler M, Schapper F, Gallmann L, Keller U (2011) Attosecond electron wave-packet interference observed by transient absorption. *Physical Review Letters* 106.

[169] Ferrari F, et al. (2010) High-energy isolated attosecond pulses generated by above-saturation few-cycle fields. *Nature Photonics* 4:875–879.

[170] Corkum PB, Burnett NH, Ivanov MY (1994) Subfemtosecond pulses. *Optics Letters* 19:1870.

[171] Altucci C, et al. (1998) Frequency-resolved time-gated high-order harmonics. *Physical Review A* 58:3934–3941.

[172] Tcherbakoff O, Mével E, Descamps D, Plumridge J, Constant E (2003) Time-gated high-order harmonic generation. *Physical Review A* 68:043804.

[173] Sansone G, et al. (2006) Isolated Single-Cycle Attosecond Pulses. *Science* 314:443–446.

[174] Li Y, et al. (2017) Bacterial endotoxin (lipopolysaccharide) binds to the surface of gold nanoparticles , interferes with biocorona formation and induces human monocyte inflammatory activation. *Nanotoxicology* 0:1157–1175.

[175] Chang Z (2007) Controlling attosecond pulse generation with a double optical gating. *Physical Review A* 76:051403.

[176] Mashiko H, et al. (2009) Extreme ultraviolet supercontinua supporting pulse durations of less than one atomic unit of time. *Optics Letters* 34:3337.

[177] Cao W, Lu P, Lan P, Wang X, Yang G (2006) Single-attosecond pulse generation with an intense multicycle driving pulse. *Physical Review A* 74:063821.

[178] Pfeifer T, et al. (2007) Generating coherent broadband continuum soft-x-ray radiation by attosecond ionization gating. *Optics Express* 15:17120.

[179] Kane D, Trebino R (1993) Characterization of arbitrary femtosecond pulses using frequency-resolved optical gating. *IEEE Journal of Quantum Electronics* 29:571–579.

[180] Muller H (2002) Reconstruction of attosecond harmonic beating by interference of two-photon transitions. *Applied Physics B* 74:s17–s21.

[181] Mairesse Y, et al. (2003) Attosecond Synchronization of High-Harmonic Soft X-rays. *Science* 302:1540–1543.

[182] Mairesse Y, Quéré F (2005) Frequency-resolved optical gating for complete reconstruction of attosecond bursts. *Physical Review A* 71:011401.

[183] Goulielmakis E, et al. (2004) Direct Measurement of Light Waves. *Science* 305:1267–1269.

[184] Feng X, et al. (2009) Generation of Isolated Attosecond Pulses with 20 to 28 Femtosecond Lasers. *Physical Review Letters* 103:183901.

[185] Gaumnitz T, et al. (2017) Streaking of 43-attosecond soft-X-ray pulses generated by a passively CEP-stable mid-infrared driver. *Optics Express* 25:27506.

[186] Zhao X, et al. (2020) Metrology of Time-Domain Soft X-Ray Attosecond Pulses and Reevaluation of Pulse Durations of Three Recent Experiments. *Phys. Rev. Applied* 13:34043.

[187] Nisoli M, et al. (1997) Compression of high-energy laser pulses below 5 fs. *Optics Letters* 22:522.

[188] Schmidt BE, et al. (2011) CEP stable 16 cycle laser pulses at 18 μm. *Optics Express* 19:6858.

[189] Buades B (2018) Ph.D. thesis.

[190] Cousin SL (2016) Ph.D. thesis (UPC - Universitat Politècnica de Catalunya).

[191] Kleine C, et al. (2019) Soft X-ray Absorption Spectroscopy of Aqueous Solutions Using a Table-Top Femtosecond Soft X-ray Source. *The Journal of Physical Chemistry Letters* 10:52–58.

[192] Lang B (2018) Photometrics of ultrafast and fast broadband electronic transient absorption spectroscopy: State of the art. *Review of Scientific Instruments* 89.

[193] Oppermann M, et al. (2019) Ultrafast broadband circular dichroism in the deep ultraviolet. *Optica* 6:56.

[194] Géneaux R, Chang HT, Schwartzberg AM, Marroux HJB (2021) Source noise suppression in attosecond transient absorption spectroscopy by edge-pixel referencing. *Optics Express* 29:951.

[195] Robben KC, Cheatum CM (2020) Edge-pixel referencing suppresses correlated baseline noise in heterodyned spectroscopies. *Journal of Chemical Physics* 152.

[196] Eckert M (2012) Max von Laue and the discovery of X-ray diffraction in 1912. *Annalen der Physik* 524:A83–A85.

[197] Bragg WH (1913) X-rays and Crystals. *Nature* 90:572–572.

[198] Bragg WH, Bragg WL (1913) The reflection of X-rays by crystals. *Proceedings of the Royal Society of London. Series A, Containing Papers of a Mathematical and Physical Character* 88:428–438.

[199] de Broglie M (1914) Sur la spectroscopie des rayons secondaires emis hors des tubes a rayons de Rontgen d'absorption. *Comptes rendus de l'Académie des Sciences* 158:1593–1495.

[200] Fricke H (1920) The K-Characteristic Absorption Frequencies for the Chemical Elements Magnesium to Chromium. *Physical Review* 16:202–215.

[201] Sayers DE, Stern EA, Lytle FW (1971) New Technique for Investigating Noncrystalline Structures: Fourier Analysis of the Extended X-Ray—Absorption Fine Structure. *Physical Review Letters* 27:1204–1207.

[202] Cushing SK, et al. (2020) Layer-resolved ultrafast extreme ultraviolet measurement of hole transport in a Ni-TiO ₂ -Si photoanode. *Science Advances* 6.

[203] Als-Nielsen J, McMorrow D (2011) *Elements of Modern X-ray Physics* (Wiley).

[204] Schoenlein RW, et al. (2000) Generation of Femtosecond Pulses of Synchrotron Radiation. *Science* 287:2237 LP – 2240.

[205] Zhao Z, et al. (2017) Status of the SXFEL Facility. *Applied Sciences* 7:607.

[206] Seddon EA, et al. (2017) Short-wavelength free-electron laser sources and science: a review. *Reports on Progress in Physics* 80:115901.

[207] Maroju PK, et al. (2020) Attosecond pulse shaping using a seeded free-electron laser. *Nature* 578:386–391.

[208] Duris J, et al. (2020) Tunable isolated attosecond X-ray pulses with gigawatt peak power from a free-electron laser. *Nature Photonics* 14:30–36.

[209] Li S, et al. (2022) Attosecond coherent electron motion in Auger-Meitner decay. *Science* 375:285–290.

[210] Korn G, et al. (2002) Ultrashort 1-kHz laser plasma hard x-ray source. *Optics Letters* 27:866.

[211] McFarland BK, et al. (2014) Ultrafast X-ray Auger probing of photoexcited molecular dynamics. *Nature Communications* 5:4235.

[212] Wolf TJA, et al. (2017) Probing ultrafast $\pi\pi^*$/nπ^* internal conversion in organic chromophores via K-edge resonant absorption. *Nature Communications* 8:29.

[213] Mayer D, et al. (2022) Following excited-state chemical shifts in molecular ultrafast x-ray photoelectron spectroscopy. *Nature Communications* 13:198.

[214] Neppl S, Gessner O (2015) Time-resolved X-ray photoelectron spectroscopy techniques for the study of interfacial charge dynamics. *Journal of Electron Spectroscopy and Related Phenomena* 200:64–77.

[215] Vaida ME, Leone SR (2016) Femtosecond Extreme Ultraviolet Photoemission Spectroscopy: Observation of Ultrafast Charge Transfer at the n-TiO2/p-Si(100) Interface with Controlled TiO2 Oxygen Vacancies. *The Journal of Physical Chemistry C* 120:2769–2776.

[216] Marsh BM, Vaida ME, Cushing SK, Lamoureux BR, Leone SR (2017) Measuring the Surface Photovoltage of a Schottky Barrier under Intense Light Conditions: Zn/p-Si(100) by Laser Time-Resolved Extreme Ultraviolet Photoelectron Spectroscopy. *The Journal of Physical Chemistry C* 121:21904–21912.

[217] Mathias S, et al. (2007) Angle-resolved photoemission spectroscopy with a femtosecond high harmonic light source using a two-dimensional imaging electron analyzer. *Review of Scientific Instruments* 78:083105.

[218] Gray AX, et al. (2011) Probing bulk electronic structure with hard X-ray angle-resolved photoemission. *Nature Materials* 10:759–764.

[219] Adachi S, Schatteburg T, Humeniuk A, Mitrić R, Suzuki T (2019) Probing ultrafast dynamics during and after passing through conical intersections. *Physical Chemistry Chemical Physics* 21:13902–13905.

[220] Wernet P, et al. (2015) Orbital-specific mapping of the ligand exchange dynamics of Fe(CO)5 in solution. *Nature* 520:78–81.

[221] Newville M (2014) Fundamentals of XAFS. *Reviews in Mineralogy and Geochemistry* 78:33–74.

[222] Hahn JE, et al. (1982) Observation of an electric quadrupole transition in the X-ray absorption spectrum of a Cu(II) complex. *Chemical Physics Letters* 88:595–598.

[223] Bunker G (2010) *Introduction to XAFS* (CAMBRIDGE UNIVERSITY PRESS).

[224] Roemelt M, Maganas D, DeBeer S, Neese F (2013) A combined DFT and restricted open-shell configuration interaction method including spin-orbit coupling: Application to transition metal L-edge X-ray absorption spectroscopy. *The Journal of Chemical Physics* 138:204101.

[225] Stöhr J (1992) *NEXAFS Spectroscopy* (Springer-Verlag) Vol. 25, p 403.

[226] Rehr JJ, Kas JJ, Vila FD, Prange MP, Jorissen K (2010) Parameter-free calculations of X-ray spectra with FEFF9. *Physical Chemistry Chemical Physics* 12:5503.

[227] Pemmaraju CD (2020) Simulation of attosecond transient soft x-ray absorption in solids using generalized Kohn–Sham real-time time-dependent density functional theory. *New Journal of Physics* 22:83063.

[228] Ahmed S, Yi J (2017) Two-Dimensional Transition Metal Dichalcogenides and Their Charge Carrier Mobilities in Field-Effect Transistors. *Nano-Micro Letters* 9:50.

[229] Manzeli S, Ovchinnikov D, Pasquier D, Yazyev OV, Kis A (2017) 2D transition metal dichalcogenides. *Nature Reviews Materials* 2:17033.

[230] Reduzzi M, et al. (2015) Polarization control of absorption of virtual dressed states in helium. *Physical Review A* 92:033408.

[231] Kobayashi Y, Timmers H, Sabbar M, Leone SR, Neumark DM (2017) Attosecond transient-absorption dynamics of xenon core-excited states in a strong driving field. *Physical Review A* 95:031401.

[232] Drescher L, et al. (2019) State-Resolved Probing of Attosecond Timescale Molecular Dipoles. *The Journal of Physical Chemistry Letters* 10:265–269.

[233] Autler SH, Townes CH (1955) Stark Effect in Rapidly Varying Fields. *Physical Review* 100:703–722.

[234] Pabst S, et al. (2012) Theory of attosecond transient-absorption spectroscopy of krypton for overlapping pump and probe pulses. *Physical Review A* 86:063411.

[235] Chen S, Wu M, Gaarde MB, Schafer KJ (2013) Laser-imposed phase in resonant absorption of an isolated attosecond pulse. *Physical Review A* 88:033409.

[236] Pullen SH, Anderson NA, Walker LA, Sension RJ (1998) The ultrafast photochemical ring-opening reaction of 1,3-cyclohexadiene in cyclohexane. *The Journal of Chemical Physics* 108.

[237] Karashima S, et al. (2021) Ultrafast Ring-Opening Reaction of 1,3-Cyclohexadiene: Identification of Nonadiabatic Pathway via Doubly Excited State. *Journal of the American Chemical Society* 143:8034–8045.

[238] Sobolewski AL, Domcke W (1991) Photophysically relevant potential energy functions of low-lying singlet states of benzene, pyridine and pyrazine: an ab initio study. *Chem. Phys. Lett.* 180.

[239] Sobolewski AL, Domcke W (2000) Conical intersections induced by repulsive 1 pr Ã states in planar organic molecules: malonaldehyde, pyrrole and chlorobenzene as photochemical model systems. *Chemical Physics* 259:181–191.

[240] Vieuxmaire OPJ, Lan Z, Sobolewski AL, Domcke W (2008) Ab initio characterization of the conical intersections involved in the photochemistry of phenol. *The Journal of Chemical Physics* 129.

[241] Chachisvilis M, Zewail AH (1999) Femtosecond Dynamics of Pyridine in the Condensed Phase: Valence Isomerization by Conical Intersections. *Journal of Physical Chemistry A* 103:7408–7418.

[242] Srinivasan R, Feenstra JS, Park ST, Xu S, Zewail AH (2005) Dark Structures in Molecular Radiationless Transitions Determined by Ultrafast Diffraction. *Science* 307.

[243] Slanina T, et al. (2020) Impact of Excited-State Antiaromaticity Relief in a Fundamental Benzene Photoreaction Leading to Substituted Bicyclo[3.1.0]hexenes. *Journal of the American Chemical Society* 142.

[244] Clarke TM, Durrant JR (2010) Charge photogeneration in organic solar cells. *Chemical Reviews* 110:6736–6767.

[245] Dalvie DK, Kalgutkar AS, Khojasteh-Bakht SC, Obach RS, O'Donnell JP (2002) Biotransformation reactions of five-membered aromatic heterocyclic rings.

[246] Meotti FC, et al. (2003) Thiophenes and furans derivatives: A new class of potential pharmacological agents. *Environmental Toxicology and Pharmacology* 15:37–44.

[247] Xu N, Gong J, Huang Z (2016) Review on the production methods and fundamental combustion characteristics of furan derivatives.

[248] Irie M (2000) Diarylethenes for Memories and Switches. *Chemical Reviews* 100:1685–1716.

[249] Schalk O, et al. (2020) Competition between ring-puckering and ring-opening excited state reactions exemplified on 5H-furan-2-one and derivatives. *Journal of Chemical Physics* 152.

[250] Improta R, Santoro F, Blancafort L (2016) Quantum Mechanical Studies on the Photophysics and the Photochemistry of Nucleic Acids and Nucleobases. *Chemical Reviews* 116:3540–3593.

[251] Hua W, Mukamel S, Luo Y (2019) Transient X-ray Absorption Spectral Fingerprints of the S1 Dark State in Uracil. *Journal of Physical Chemistry Letters* 10:7172–7178.

[252] Gavrilov N, Salzmann S, Marian CM (2008) Deactivation via ring opening: A quantum chemical study of the excited states of furan and comparison to thiophene. *Chemical Physics* 349:269–277.

[253] Stenrup M, Larson Å (2011) A computational study of radiationless deactivation mechanisms of furan. *Chemical Physics* 379:6–12.

[254] Gromov EV, Trofimov AB, Gatti F, Köppel H (2010) Theoretical study of photoinduced ring-opening in furan. *Journal of Chemical Physics* 133.

[255] Palmer MH, Walker IC, Ballard CC, Guest MF (1995) The electronic states of furan studied by VUV absorption, near-threshold electron energy-loss spectroscopy and ab initio multi-reference configuration interaction calculations. *Chemical Physics* 192:111–125.

[256] Gromov EV, Trofimov AB, Vitkovskaya NM, Schirmer J, Köppel H (2003) Theoretical study of the low-lying excited singlet states of furan. *Journal of Chemical Physics* 119:737–753.

[257] Gromov EV, et al. (2004) Theoretical study of excitations in furan: Spectra and molecular dynamics. *Journal of Chemical Physics* 121:4585–4598.

[258] Steinmetzer J, Kupfer S, Gräfe S (2021) pysisyphus: Exploring potential energy surfaces in ground and excited states. *International Journal of Quantum Chemistry* 121.

[259] Adamo C, Barone V (1999) Toward reliable density functional methods without adjustable parameters: The PBE0 model. *The Journal of Chemical Physics* 110:6158–6170.

[260] Ernzerhof M, Scuseria GE (1999) Assessment of the Perdew–Burke–Ernzerhof exchange-correlation functional. *The Journal of Chemical Physics* 110:5029–5036.

[261] Clark T, Chandrasekhar J, Spitznagel GW, Schleyer PVR (1983) Efficient diffuse function-augmented basis sets for anion calculations. III. The 3-21+G basis set for first-row elements, Li-F. *Journal of Computational Chemistry* 4:294–301.

[262] Krishnan R, Binkley JS, Seeger R, Pople JA (1980) Self-consistent molecular orbital methods. XX. A basis set for correlated wave functions. *The Journal of Chemical Physics* 72:650–654.

[263] Gromov EV, Lévêque C, Gatti F, Burghardt I, Köppel H (2011) Ab initio quantum dynamical study of photoinduced ring opening in furan. *Journal of Chemical Physics* 135.

[264] Fuji T, et al. (2010) Ultrafast photodynamics of furan. *Journal of Chemical Physics* 133.

[265] Liu Y, Knopp G, Qin C, Gerber T (2015) Tracking ultrafast relaxation dynamics of furan by femtosecond photoelectron imaging. *Chemical Physics* 446:142–147.

[266] Oesterling S, et al. (2017) Substituent effects on the relaxation dynamics of furan, furfural and β-furfural: A combined theoretical and experimental approach. *Physical Chemistry Chemical Physics* 19:2025–2035.

[267] Spesyvtsev R, Horio T, Suzuki YI, Suzuki T (2015) Excited-state dynamics of furan studied by sub-20-fs time-resolved photoelectron imaging using 159-nm pulses. *Journal of Chemical Physics* 143.

[268] Ruckenbauer M, Mai S, Marquetand P, González L (2016) Revealing Deactivation Pathways Hidden in Time-Resolved Photoelectron Spectra. *Scientific Reports* 6:1–14.

[269] Piteša T, et al. (2021) Combined Surface-Hopping, Dyson Orbital, and B-Spline Approach for the Computation of Time-Resolved Photoelectron Spectroscopy Signals: The Internal Conversion in Pyrazine. *Journal of Chemical Theory and Computation* 17:5098–5109.

[270] Newbury DC, Ishii I, Hitchcock AP (1986) Inner shell electron-energy loss spectroscopy of some heterocyclic molecules. *Canadian Journal of Chemistry* 64.

[271] Rennie EE, et al. (2002) A core-level photoionization study of furan. *Journal of Chemical Physics* 117:6524–6532.

[272] Cederbaum LS, Domcke W, Schirmer J (1980) Many-body theory of core holes. *Physical Review A* 22:206–222.

[273] Tsuru S, et al. (2019) Time-resolved near-edge X-ray absorption fine structure of pyrazine from electronic structure and nuclear wave packet dynamics simulations. *The Journal of Chemical Physics* 151:124114.

[274] Duflot D, Flament JP, Giuliani A, Heinesch J, Hubin-Franskin MJ (2003) Core shell excitation of furan at the O1s and C1s edges: An experimental and ab initio study. *The Journal of Chemical Physics* 119.

[275] Richter M, Marquetand P, González-Vázquez J, Sola I, González L (2011) SHARC: ab initio Molecular Dynamics with Surface Hopping in the Adiabatic Representation Including Arbitrary Couplings. *Journal of Chemical Theory and Computation* 7:1253–1258.

[276] Mai S, Marquetand P, González L (2018) Nonadiabatic dynamics: The SHARC approach. *WIREs Computational Molecular Science* 8.

[277] Wei Z, et al. (2017) Elucidating the origins of multimode vibrational coherences of polyatomic molecules induced by intense laser fields. *Nature Communications* 8.

[278] Yang J, Li J, Mo Y (2006) The vibrational structures of furan, pyrrole, and thiophene cations studied by zero kinetic energy photoelectron spectroscopy. *Journal of Chemical Physics* 125.

[279] Sendt K, Bacskay GB, Mackie JC (2000) Pyrolysis of furan: Ab initio quantum chemical and kinetic modeling studies. *Journal of Physical Chemistry A* 104:1861–1875.

[280] Urness KN, et al. (2013) Pyrolysis of furan in a microreactor. *The Journal of Chemical Physics* 139:124305.

[281] Okajima T, et al. (2002) Soft X-ray absorption spectra of the Lithium Phthalocyanine radical., Technical Report 1.

[282] Alagia M, et al. (2013) The soft X-ray absorption spectrum of the allyl free radical. *Physical Chemistry Chemical Physics* 15:1310–1318.

[283] Eidam T, et al. (2010) Femtosecond fiber CPA system emitting 830 W average output power. *Optics Letters* 35:94.

[284] Nagy T, et al. (2019) Generation of three-cycle multi-millijoule laser pulses at 318 W average power. *Optica* 6:1423.

[285] Hrisafov S, et al. (2020) High-power few-cycle near-infrared OPCPA for soft X-ray generation at 100 kHz. *Optics Express* 28:40145.

[286] Kleine C, et al. (2021) Highly efficient soft x-ray spectrometer for transient absorption spectroscopy with broadband table-top high harmonic sources. *Structural Dynamics* 8:034302.

[287] Hosseini P, Ermolov A, Tani F, Novoa D, Russell PS (2018) UV Soliton Dynamics and Raman-Enhanced Supercontinuum Generation in Photonic Crystal Fiber. *ACS Photonics* 5:2426–2430.

[288] Travers JC, Grigorova TF, Brahms C, Belli F (2019) High-energy pulse self-compression and ultraviolet generation through soliton dynamics in hollow capillary fibres. *Nature Photonics* 13:547–554.

[289] Koralek JD, et al. (2018) Generation and characterization of ultrathin free-flowing liquid sheets. *Nature Communications* 9:1353.

ABBREVIATIONS

AIP	Attosecond Isolated Pulses
AttoXAFS	Attosecond XAFS
BBO	Beta Barium Borate
BO	Born-Oppenheimer
CB	Cunduction Band
CEP	Carrier-to-Envelope Phase
CI	Conical Intersection
DFG	Difference-Frequency Generation
EXAFS	Extended-edge X-rays Absorption Fine Structure
FC	Franck Condon
FEL	Free Electron Laser
FROG	Frequency-Resolved Optical Gating
FT	Fourier Transform
GS	Ground State
HCF	Hollow Core Fiber
HHG	High Harmonic Generation
HHS	High Harmonic Spectroscopy
HOPG	Highly-Oriented Pyrolithic Graphite
IC	Internal Conversion
IR	Infrared
LIED	Light Induced Electron Diffraction
NIR	Near Infrared
OPA	Optical Parametric Amplification
PES	Potential Energy Surface
PFS	Photofragmentation Spectroscopy
PS	Photoelectron Spectroscopy
RABBITT	Reconstruction of Attosecond Beating By Interference of Two-photon Transitions
RIXS	Resonant Inelastic X-rays Scattering
RO	Ring-Opening
ROCI	Ring-Opening Conical Intersection
RP	Ring-Puckering
RPCI	Ring-Puckering Conical Intersection
S/N	Signal to Noise ratio

SFG	Sum-Frequency Generation
SHG	Second-Harmonic Generation
STFT	Short-Time Fourier Transform
SWIR	Short Wavelength Infrared
SXR	Soft X-rays
TA	Transient Absorption
Ti:Sa	Titanium:Sapphire
ToF	Time-of-Flight
tr	time-resolved
UV	Ultra-Violet
VB	Valence Band
Vis	Visible
XAFS	X-rays Absorption Fine Structure
XANES	X-rays Absorption Near-Edge Structure
XUV	EXtreme Ultra-Violet
YAG	Yttrium - Aluminum - Garnet

LIST OF PUBLICATIONS

Here is the list of publications related to the work carried out during my Ph.D. project.

- T. P. H. Sidiropoulos*, N. Di Palo*, D. E. Rivas*, **S. Severino**, M. Reduzzi, B. Nandy, B. Bauerhenne, S. Krylow, T. Vasileiadis, T. Danz, P. Elliott, S. Sharma, K. Dewhurst, C. Ropers, Y. Joly, M. E. Garcia, M. Wolf, R. Ernstorfer, and J. Biegert, *"Probing the Energy Conversion Pathways between Light, Carriers, and Lattice in Real Time with Attosecond Core-Level Spectroscopy"*, Physical Review X, **11**, 041060 (2021)

- A. M. Summers*, **S. Severino***, M. Reduzzi, T. P. H. Sidiropoulos, D. E. Rivas, N. Di Palo, Hung-Wei Sun, Ying-Hao Chien, I. León, B. Buades, S. L. Cousin1, S. M. Teichmann, T Mey, K. Mann, B. Keitel, E Plönjes-Palm, D. K. Efetov, H. Schwoerer, J. Biegert, *"Realizing attosecond core-level X-ray spectroscopy for the investigation of condensed matter systems "*, accepted in Ultrafast Science.

- **S. Severino***, K.M. Ziems*, M. Reduzzi, A. Summers, H.-W. Sun, Y.-H. Chien, S. Gräfe, J. Biegert, *"Non-Adiabatic Electronic and Vibrational Ring-Opening Dynamics resolved with Attosecond Core-Level Spectroscopy"*, submitted.

AUTHOR'S CONTRIBUTION

The aim of this section is to highlight the author's contributions with respect to the different works presented in this thesis. The laser system providing CEP-stable, few-cycle infrared pulses was built by Dr. Seth L. Cousin (SC) and Dr. Michael Hemmer under the supervision of Prof. Dr. Jens Biegert (JB). The actual setup for the Attosecond Beamline is a slight modification of the original scheme designed by JB and realized by BesTec. The Mirror and the Experimental chambers preserve the original design, while the Spectrograph was rebuilt by SC with the help of Dr. Nicola Di Palo (NDP) and Dr. Bárbara Buades (BB). The Generation and Differential Pumping chamber are instead a new design realized by Dr. Biplob Nandy and JB and then installed by NDP and Dr. Themistoklis P. H. Sidiropoulos (TS).

The source characterization in terms of flux, tunability and stability has been realized by the author with the help of NDP, TS, and Dr. Daniel Rivas (DR). The collinear pump-probe setup was realized by the author, together with Dr. Maurizio Reduzzi (MR), Dr. Adam Summers (AS), Hung-Wei Sun (HWS) and Ying-Hao Chien (YHC). The XAFS measurements taken at ALBA synchrotron source (see Fig.2.9) were collected by Dr. Eric Pellegrin, Dr. Pierluigi Gargiani and Dr. Manuel Valdivares. The static measurements shown in chapter 3 were performed by the author, AS, MR, HWS and YHC. The experimental campaign for the time-resolved investigation of the strong-field induced effects in argon was led by the author and MR, with the help of AS, TS, HWS and YHC. The data were analyzed by the author with the support of MR.

The experimental campaign for the time-resolved data in furan presented in chapter 4 was led by the author and MR and performed with the help of AS, HWS and YHC. The analysis of the collected experimental data was performed by the author with the support of MR. The theory calculations were performed by Karl Michael Ziems (KMZ) from the group of Prof. Dr. Stefanie Gräfe and analyzed by the author and KMZ. The combined simulated and experimental data were interpreted by the author with the help of KMZ and MR.

ACKNOWLEDGMENTS

Acknowledgements.